INVESTIGATION ON THE INCORPORATION OF QUANTUM DOT THIN FILM LAYERS IN THE ORGANIC AND INORGANIC SOLAR CELL STRUCTURES

A THESIS SUBMITTED TO

THE GRADUATE SCHOOL OF NATURAL AND APPLIED SCIENCES

OF

MIDDLE EAST TECHNICAL UNIVERSITY

BY

İDRİS CANDAN

IN PARTIAL FULFILLMENT OF THE REQUIREMENTS

FOR

THE DEGREE OF DOCTOR OF PHILOSOPHY

IN

PHYSICS

FEBRUARY 2016

Approval of the thesis:

INVESTIGATION ON THE INCORPORATION OF QUANTUM DOT THIN FILM LAYERS IN THE ORGANIC AND INORGANIC SOLAR CELL STRUCTURES

submitted by **İDRİS CANDAN** in partial fulfillment of the requirements for the degree of **Doctor of Philosophy in Physics Department, Middle East Technical University** by,

Prof. Dr. Gülbin Dural Ünver _____
Dean, Graduate School of **Natural and Applied Sciences**

Prof. Dr. Mehmet Zeyrek _____
Head of Department, **Physics**

Prof. Dr. A. Çiğdem Erçelebi _____
Supervisor, **Physics Dept., METU**

Prof. Dr. Mehmet Parlak _____
Co-Supervisor, **Physics Dept., METU**

Examining Committee Members

Prof. Dr. Ahmet Macit Özenbaş _____
Metallurgical and Materials Engineering Dept., METU

Prof. Dr. A. Çiğdem Erçelebi _____
Physics Dept., METU

Prof. Dr. Raşit Turan _____
Physics Dept., METU

Assoc. Prof. Dr. Hakan Karaağaç _____
Physics Engineering Dept., İTU

Assoc. Prof. Dr. Kadir Ertürk _____
Physics Dept., NKU

Date: *05.02.2106*

I hereby declare that all information in this document has been obtained and presented in accordance with academic rules and ethical conduct. I also declare that, as required by these rules and conduct, I have fully cited and referenced all material and results that are not original to this work.

Name, Last name : İdris Candan

Signature :

ABSTRACT

INVESTIGATION ON THE INCORPORATION OF QUANTUM DOT THIN FILM LAYERS IN THE ORGANIC AND INORGANIC SOLAR CELL STRUCTURES

Candan, İdris

Ph.D., Department of Physics

Supervisor : Prof. Dr. A. Çiğdem Erçelebi

Co-Supervisor: Prof. Dr. Mehmet Parlak

February 2016, 129 pages

Thin films based photovoltaic solar cell technologies have the Shockley-Queisser limit for maximum efficiencies and these cells can only collect photon in the specific energy range due to their band gap. New approaches are needed to improve the power conversion efficiency (PCE) of photovoltaic devices. Quantum dots (QDs) thin film layer inside any device structure is particularly attractive candidates to increase the PCE of solar cells due to their size adjustable band gap values, multiple exciton generation (MEG) properties. Among the QDs, lead sulfide (PbS) has high photo sensitivity in the infrared (IR) region of electromagnetic spectrum and can be produced with the band gap values in the range of 0.7 to 2.1 eV. Therefore, PbS QD is the material which can be used as a thin film layer in traditional solar cell device architecture to collect photons, having energies in the near IR region which are normally not collected by the devices.

In this study, a new method for increasing the PCE of organic and inorganic solar cells by using QDs thin film layer inside the device structure is discussed. Lead sulfide quantum dots (PbS QDs) thin film layers are separately located inside organic and inorganic devices. The polycrystalline chalcopyrite $CuIn_{1-x}Ga_xSe_2$ (CIGS) thin films as an inorganic semiconductor and a blend of Poly (3-hexylthiophene-2, 5-diyl) and poly (6, 6-phenyl C61-butyric acid methyl ester) (P3HT:PCBM) as an organic semiconductor are chosen to cooperate with QDs thin film layer for the production of light converting devices. To determine the contributions of PbS QDs thin film layer inside the devices, the optical, structural, morphological, electrical measurements were performed by using the transmission, absorbance, XRD, Raman spectroscopy, SEM, TEM, photoluminescence (PL), photoconductivity, Hall effect, external quantum efficiency (EQE), current–voltage (I-V), capacitance-voltage (C-V), and impedance spectroscopy measurements.

Keywords: Lead sulfide quantum dots (PbS QDs), Chalcopyrite, CIGS thin film, inverted polymer solar cell (IPSC), P3HT:PCBM, organic solar cells.

ÖZ

KUANTUM NOKTA İNCE FİLM TABAKASININ ORGANİK VE İNORGANİK GÜNEŞ PİLİ YAPILARINA EKLENMESİ

Candan, İdris

Doktora, Fizik Bölümü

Tez Yöneticisi: Prof. Dr. A. Çiğdem Erçelebi

Ortak Tez Yöneticisi: Prof. Dr. Mehmet Parlak

Şubat 2016, 129 sayfa

İnce film tabanlı fotovoltaik güneş pili teknolojisinde en yüksek verimlilik değeri Shockley-Queisser limiti tarafından sınırlandırmakta olup bu aygıtlar bant aralıklarından dolayı yalnızca belirli bir bölgedeki fotonların enerjisini toplayabilmektedirler. Fotovoltaik aygıtların PCE değerini geliştirmek için yeni yaklaşımlara ihtiyaç vardır. Kuantum nokta ince film katmanı, ayarlanabilir bant aralıkları, çoklu eksiton üretim özellikleri (MEG) ve aynı zamanda güneş spektrumunun özel bir bölgesi için kullanılabiliyor olmalarından dolayi, güneş pili aygıtlarının PCE değerini artırmak için cazip bir aday olmaktadır. Kuantum noktalar içerisinde, kurşun sülfat (PbS) elektromanyetik spektrumun kızılötesi bölgesinde mükemmel ışık hassasiyetine sahiptir ve bant yapısı olarak ta 0.7 ile 2.1eV aralığında üretilebilmektedir. Dolayısıyla, PbS kuantum noktalar malzemelerde güneş spektrumunun geniş bölgesinden ışığı toplayabildiğinden geleneksel güneş pili yapısı içerisinde ince film katmanı olarak normalde toplanamayan yakın kızılötesi bölgesinden de foton toplamak için mükemmel bir adaydır.

Bu çalışmada, organik ve inorganik güneş pillerinin PCE değerlerini artırmak için yeni bir metod olarak aygıt yapısı içerisinde kuantum nokta ince film katmanının kullanılmasi tartışılmaktadır. Kurşun sülfat kuantum noktalar ince film katmanı organik ve inorganik aygıtlar içerisine ayrı ayrı yerleştirilmektedir. Işık dünüştürücü aygıtlarda kuantum nokta ince film katmanı ile beraber inorganik yarıiletken olarak polikristal kalkopirit $CuIn_{1-x}Ga_xSe_2$ (CIGS) ve organik yarıiletken olarak Poly (3-hexylthiophene-2,5-diyl) ve poly (6,6-phenyl C61-butyric acid methyl ester) (P3HT:PCBM) karışımı seçilmiştir. Aygıt içerisindeki PbS QDs tabakasının etkisi optiksel, yapısal, morfolojik, elektriksel ölçümler ve geçirgenlik, soğurma, XRD, Raman spektroskopisi, SEM, TEM, PL, fotoiletkenlik, Hall etkisi, harici kuantum verimliliği (EQE), akım-voltaj (I-V), kapasitans–voltaj (C-V) ve empedans ölçümleri ile incelendi.

Anahtar Sözcükler: Kurşun sülfat kuantum noktalar (PbS QDs), kalkopirite, CIGS ince film, ters çevrilmiş polimer güneş pili (IPSC), P3HT:PCBM, organik güneş pilleri.

To my lovely family, once again.

To my daughter Narin Nisa for being with me during the nights as my light…

ACKNOWLEDGEMENTS

It is a great pleasure to work with my supervisor Prof. Dr. A.Çiğdem Erçelebi. Her valuable patience, encouragement and motivation led to the completion of the thesis as a friend and sometimes as a mother. I always feel an admiration about her positive energy, scientific knowledge and creative criticism throughout thesis. In addition, I express my endless thanks to my co-supervisor Prof. Dr. Mehmet Parlak for his scientific guadience, helpful suggestions, keeping his eyes on me at every steps of experimental stages, continous support and kind friendship.

I would like to express my deepest gratitude to Prof. Dr. Kang L. Wang for accepting and giving oppurtinity to me to study under his supervision in Device Research Laboratory (DRL) at University of California – Los Angeles (UCLA), USA, and for his great guidance and advice.

I will always be grateful to my dear friend Dr. Chandan Biswas for his good friendship, helps and encouragements during my days at UCLA.

I am also very grateful to the examining committee members Prof. Dr. A. Macit Özenbaş, Prof.Dr. Rasit Turan, Dr. Hakan Karaağaç and Dr. Kadir Ertürk for their valuable comments and feedback during my thesis defence.

I also want to express my thanks to my lab-mates, Dr. Tahir Çolakoğlu, Dr. Hakan Karaağaç, Dr. Murat Kaleli, Dr. Emre Coşkun, Hasan Hüseyin Güllü, Özge Bayraklı, Makbule Telemezoğlu, Arezoo Hosseini and Cansu Emir for their good friendship, helps and encouragements.

I also would like to thank to technicians Yücel Eke, Nevzat Görmez, Tayfun Demir, Dursun Erdoğan for their kind friendship and technical assistance during every stage of this study.

I would like to thank all academic and administrative staff of the Department of Physics, especially Mrs. Gülşen Parlak, Mrs. Zeynep Eke, Mrs. Selda Atasever, and Mrs. Özge Topal for everything they have done concerning the time-consuming bureaucratic tasks.

I would like to express my endless thanks to my friends Dr. M. Ali Kaplan and Av. Zekeriya Çetin for their valuable supports during my USA travel as a visiting scholar.

I wish to thank my friends: Dr. Nevfel Boz, Dr. Olcay Mert, Dr. Muhammed Aydın, Dr. Fahri Öztürk, Dr. Fatih Bay, Dr. Mustafa Kulakçı, Dr. Fuat Korkut, Dr. Hakan Bayrak, Dr. Halil Ibrahim Yavuz, Dr. Sholeh Alaei, Dr. Hisham Nasser, Fırat Es, Zeynep Demircioğlu, Nehir Yasan, Mücahid Yılmaz, Ziya Türetken, Mustafa Kaya, Gaffar Büyüktaş, Sedat Çalışkan, Yasin Tunç, Aydoğan Yanılmaz, Alper Karaaslan, İlhan Candan, and Hüseyin Kırmızı.

I would also like to thank Kocaeli University for the financial support during my thesis via Faculty Development Program (ÖYP).

My special thanks go to my parents, Nesibe and Muhiddin Candan, my brothers, İlyas, M. Ali and M. Akif and my sisters, Huri, Gülsüm, Meryem, Selma, and Büşra and my wife Nucude for their endless love and trust in me. They have always been with me and supported endlessly whenever I need them. Without them the life would be meaningless for me.

Finally, I would like to thank to all whose direct and indirect support helped me completing my thesis in time.

TABLE OF CONTENTS

LIST OF TABLES

TABLES

LIST OF FIGURES

FIGURES

CHAPTER 1

INTRODUCTION

Human population growth and industrialization of countries are increasing from the industrial revolution to now. Increasing energy costs and global climate change due to heavily using of fossil fuels have motivated interest in renewable energy resources. Hydropower, wind, and solar energies are the most common renewable energy sources which are investigated nowadays. Among the renewable energy, solar energy is the most promising alternative energy source to supply the world energy demand because of longevity, cost-effective and clean properties. Solar cells are the photovoltaic devices that can directly convert solar radiation into electricity in anywhere on the earth or outside of the earth. The earth receives 174 petawatts of incoming solar radiation in one hour which is enough energy for total annual energy needs of worldwide [1].

This chapter will focus on the historical background for photovoltaic solar cells technology, motivation of dissertation and it gives a brief outline for this thesis.

1.1 Development of Photovoltaic Solar Cells

The photovoltaic solar cell is a device which can convert the sun light energy directly into the electricity. When light is exposed to the photovoltaic materials, the photon energies make electrons excitation to higher energy states in those materials. The first photoelectric effect was observed by Edmund Becquerel in 1839. He reported that silver (Ag) coated platinum (Pt) electrodes produced a photocurrent [2]. In 1883, Charles Fritts invented the first working photovoltaic solar cell by melting selenium (Se) into a thin sheet on a metal substrate and used a gold leaf film on top of the

selenium film as the top contact [3]. In 1932, the photovoltaic effect of cadmium selenide (CdSe) was discovered by Audobert and Stora. This development opened up the way to II–VI solar cell technologies [4]. Nearly 10 years later, Russel Ohl developed the silicon based point contact rectifier which was sensitive to visible light and generating an electromotive force that independent of the applied voltage [5]. The development of the p-n junction manufacturing technique made to start the silicon electronic and solar cell technology in the 1950s. In 1954, researchers from Bell Labs made a silicon p-n junction solar cell and observed 6% power conversion efficiency (PCE) under the solar irradiance [6]. The first thin film based photovoltaic solar cell device was made in single crystal form of the cuprous sulphide /cadmium sulphide (p-Cu_2S/n-CdS) heterojunction by Reynolds et al. in 1954 [7]. Other semiconductor materials such as cadmium telluride (CdTe), gallium arsenide (GaAs), and indium phosphide (InP) were used to make p–n junction photovoltaic devices, but Si has remained the primary photovoltaic material [8]. Afterwards, the Soviets satellite, Sputnik, has powered completely by solar cells in 1957 [9]. In 1976, the first chalcopyrite thin film based solar cell ($CuInSe_2$) was fabricated with a 5.7% efficiency value by Kazmerski et al [10]. Since then, the researhers have been working the polycrystalline thin film $CuInSe_2$ solar cells. Nowadays, the copper indium gallium diselenide (CIGS) thin film based solar cells reached the efficiency value of 21.7% by the scientists of Zentrum für Sonnenenergie - und Wasserstoff (ZSW), setting a new world record for this type of cell in the National Renewable Energy Laboratory (NREL) [11].

Figure 1.1 shows the best efficiencies chart for various photovoltaic technologies in the laboratory prototype [National Renewable Energy Laboratory, 2015].

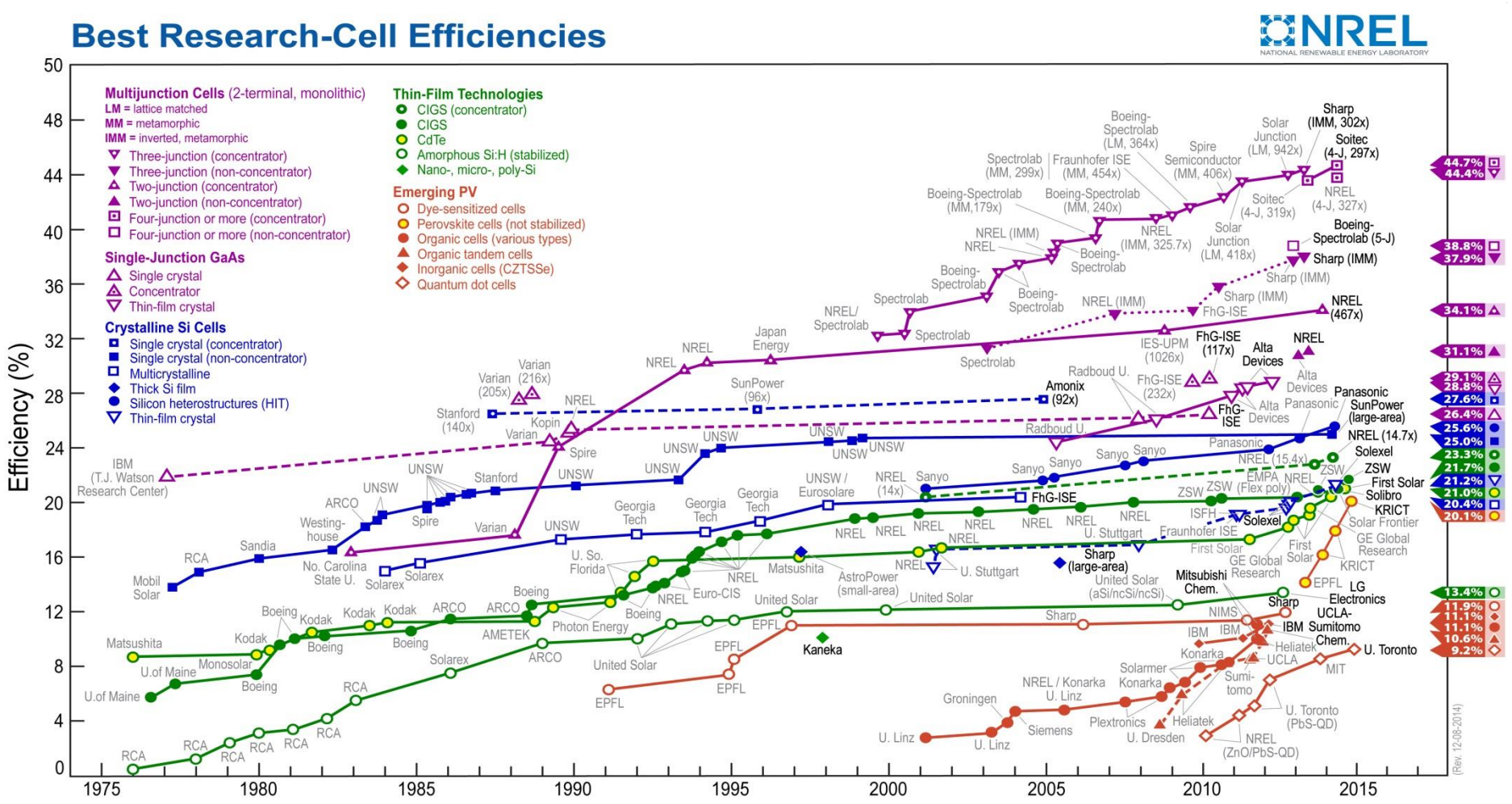

Figure 1.1 The best efficiencies chart for various photovoltaic technologies in the laboratory prototype [National Renewable Energy Laboratory, 2015]

1.2 Motivation

Power conversion efficiency (PCE) is the most critical parameter for production of low-cost solar cell devices. Inorganic thin film based and organic polymer based solar cells offer strong potential for low-cost energy harvesting in replacement of conventional solar cells but their absorption limitation of solar spectra and carrier mobility problems enforce the restriction on achieving commercially practicable [12]. The main problem of inorganic thin film based and organic polymer based photovoltaic solar cells technologies is the harvesting solar radiation efficiently from all spectra. New approaches to harvest photons with wide range are needed to increase the efficiency of photovoltaic devices [13], [14]. The solution of increasing efficiency problem of photovoltaic devices should be easy and applicable. In recent years, several approaches have been suggested to be able to go beyond Shockley-Queisser theoretical limit. Some researchers have focused on tandem (or multi-junction) solar cells and used an arrangement of several materials with different band gaps to improve device efficiency [15]–[20]. This type of solar cells can collect the photons in the wide range of solar spectra (from UV to IR) but these devices are sophisticated and very difficult to build and also expensive to produce commercially. On the other hand, well organized nanoparticles layer inside any device structure is particularly attractive candidates to increase the efficiency of solar cells due to their size settable band gaps and multiple exciton generation (MEG) properties and they can also can be used in solar cell architecture for specific electromagnetic radiation region [21]–[23]. Therefore, hybrid solar cells, consisting of both organic and inorganic nanoparticles especially quantum dots (QDs) in thin film form, propose a new approach to increase in the efficiency value of solar cell devices [23], [24]. In recent years, many researchers have used nanoparticle with different applications such as light trapping, surface plasmon enhancement, dye-sensitized nanowire, blending polymer and nanoparticle, surface-embedded nanowire etc. to increase efficiency of photovoltaic devices [25]–[29]. In all of these applications except thin films, nanoparticles are not homogeneously distributed and there are huge differences from one part of device to other parts. In other words, local improvement in absorption or the increase in the carrier density is not the solution for the efficiency limitation problem. On the other hand, QDs in thin film form can be homogeneously distributed on substrates and improve the efficiency value as well [30].

In the last two decades, colloidal nanocrystal QDs has been densely used to build third generation solar cells devices. Nowadays, QDs solar cells have been much progressed and the PCE of QDs photovoltaic solar cells have reached the value of 9.2% [31]–[33]. Additionally, the developments in QD surface passivation, especially changing organic legands with halide ions, and extending in the spectral sensitivity of cells with arrangement of particle size from visible region to near-infrared (near-IR) region. These spectral regions including nearly half of the energy of the solar spectrum have been brought about progress in QDs solar cells' PCE [34], [35]. The QDs have been produced from different semiconductors and they are optically active from the ultraviolet (UV) to the near-IR regions of the solar spectrum. Cadmium sulfide (CdS), zinc selenide (ZnSe) and zinc sulfide (ZnS) QDs have absorption range in the UV region, cadmium selenide (CdSe), cadmium telluride (CdTe) and indium phosphide (InP) QDs have absorption range in the visible region, and lead selenide (PbSe), lead telluride (PbTe), and lead sulfide (PbS) QDs have absorption values in the IR region [36]–[41]. Among the QDs, PbS QDs having band gaps range 0.7 to 2.1 eV, has a wonderful photosensivity in the near-IR region of solar spectrum and this property makes it the perfect candidate for material to harvest the light from wide range of solar spectrum [41], [42]. Therefore, they can be used as a thin film inside inorganic and organic solar cell device structure to collect photons, having energies in the near-IR region.

It should be mentioned that all experiments for inorganic part of this work were carried out at Physics Department and Center for Solar Energy Research and Application (GÜNAM) of Middle East Technical University. Whereas, most of the experiments for organic part were conducted at Device Research Laboratory (DRL) in the Electrical Engineering Department at University of California, Los Angeles (UCLA).

1.3 Thesis Outline

This thesis was divided into six main chapters. In the following chapter, the theoretical background about p-n junction, heterojunction, photovoltaic effect (PV), the properties of inorganic CIGS thin film and solar cell device mechanism has been introduced.

Chapter 3 deals with the detailed explanation about the properties of quantum dots, quantum confinement effects, up and down conversions, and multi exciton generation (MEG) process.

Chapter 4 gives detailed explanation about organic solar cells, the chemical and physical properties of organic semiconductors, and also conventional and inverted polymer solar cells (IPSC) have been described.

It is followed by chapter 5 in which detailed explanations of the preparation and deposition of $CuIn_{1-x}Ga_xSe_2$ (CIGS) thin film and P3HT;PCBM polymer solar cell, and QDs layer have been presented. It gives short information about the physical nature of the methods and techniques which were used during the deposition, physical improvement and characterization of the inorganic thin film based and polymer based solar cell devices.

In chapter 6, the structural, electrical and optical properties of the deposited inorganic thin film, polymer layers, and the effect of QDs layer inside inorganic and organic light converting devices have been discussed over the results presented.

Finally, general conclusions and the interpretations of the results are given in the last chapter.

CHAPTER 2

INORGANIC SEMICONDUCTOR SOLAR CELLS

2.1 Introduction

This chapter introduces a brief presentation of fundamental information about the semiconductors, chalcopyrite structure, and properties of CIGS thin film solar cells, p-n junction model, heterojunctions, heterojunction under the illumination, the photovoltaic (PV) effect, and the solar cell device mechanism to explain experimental results obtained by electrical measurements.

2.2 Semiconductors

There are several types of semiconductors like elemental, binary, ternary, multinary, oxides, and organic semiconductors. The best known and commonly used elemental semiconductors are the silicon (Si) and Germanium (Ge) for the electronic device applications. GaAs, GaN, and InP are well known binary III-V compound semiconductors, and ZnSe, ZnS, and CdTe are the examples of binary II-VI compound semiconductors with the zinc-blende structure [43]. The bonding between components is partially ionic due to electron transferring from group III atom to group V atom or group II atom to group VI atom. PbS, PbSe, PbTe, and SnS are also examples of binary (IV-VI compound) semiconductors [43]. $CuInSe_2$, $CuGaSe_2$, $AgGaS_2$ are the examples of ternary I-III-VI_2 and $ZnSiP_2$ is the example of ternary II-IV-V_2 compound semiconductors, respectively. $CuIn_{1-x}Ga_xSe_2$ is the example of multinary semiconductor. The oxides are mostly insulators but some of the oxide forms such as ZnO, CuO, CuO_2 and TiO_2 show semiconductor behavior and they are

used as conducting oxide layer in opto-electronic applications. The organic semiconductors such as P3HT, PCBM, NDI, MDMO-PPV and phthalocyanine are widely used in electronics and light converting systems due to the cheap price and flexibility [44], [45].

2.3 p-n junctions

An n-type semiconductor has a high concentration of negative carriers (electrons) while a p-type semiconductor has a high concentration of positive carriers (holes). When p-type and n-type semiconductors are in contact, the p-n junction is formed which allow for exchange of electrons and holes until the equilibrium is reached. If n-type and p-type semiconductor materials are the same materials this junction type called as homojunction, otherwise heterojunction. A homojunction occurs between similar semiconductor material and these materials have equal band gaps but typically have different doping type. William Shockley established the basic theory of current-voltage (I-V) characteristics of p-n junctions in 1948 [46]. The electrons from n-type material diffuse into the p-type material, leaving behind ionized donor levels, and holes from p-type material diffuse into the n-type material, leaving behind ionized acceptor levels. The mobile carriers diffuse in the region near the p-n junction and they leave behind fixed charges. This region is called depletion region or space charge region since it is depleted of charges. Figure 2.1 shows the depletion region (space charge region), electric field distribution, and band gap diagram of a typical p-n junction.

Since the mobile carriers are depleted, the ionized impurities of space charge region are no longer in equilibrium. This leads to a buildup negative (N_A^-) charges (electrons) on p-side of junction and a positive (N_D^+) charges (holes) on the n-side of junction. This creates a potential difference through the junction and results in an internal electric field between n and p sides. This internal electric field is directed from n-side to p-side and resists the further flow of electrons from the n-side and holes from the p-side. The magnitude of internal electric field is given by

$$E = \frac{-dV(x)}{dx} \tag{2.1}$$

where V is the potential through the p-n junction.

In thermal equilibrium condition, the built in potential, a potential difference without applying bias, is given by

$$qV_{bi} = E_g - \left(q\Phi_n + q\Phi_p\right) = qV_n + qV_p \tag{2.2}$$

here V_n and V_p are barrier potentials between the Fermi energy level (E_F) and intrinsic energy level (E_i) in the n-type semiconductor and p-type semiconductor as shown in Figure 2.1 (c) [47].

The built in potential for non-degenerate semiconductors is given by

$$V_{bi} = \frac{kT}{q}\ln\left(\frac{n_{n0}}{n_i}\right) + \frac{kT}{q}\ln\left(\frac{p_{p0}}{n_i}\right) \approx \frac{kT}{q}\ln\left(\frac{N_A N_D}{n_i^2}\right) \tag{2.3}$$

Since at equilibrium;

$$n_{n0}p_{n0} = n_{p0}p_{p0} = n_i^2 \tag{2.4}$$

then, the built in potential can be written as

$$V_{bi} = \frac{kT}{q}\ln\left(\frac{n_{n0}}{n_{p0}}\right) = \frac{kT}{q}\ln\left(\frac{p_{p0}}{p_{n0}}\right) \tag{2.5}$$

The Equation 2.5 gives the relationship between carrier densities on either side of p-n junction [47].

The internal electric field can be found by using Poisson equation for depletion region as

$$-\frac{d^2V_i}{dx^2} = \frac{d\epsilon}{dx} = \frac{\rho(x)}{\varepsilon_s} = \frac{q}{\varepsilon_s}[N_D(x) - n(x) - N_A(x) + p(x)]. \tag{2.6}$$

Inside the depletion region;

$$n(x) \approx p(x) \approx 0 \tag{2.7}$$

Assuming the complete ionization and using Eq. 2.7 in Eq. 2.6, we get

$$\frac{d^2V_i}{dx^2} \approx \frac{qN_A}{\varepsilon_s} \qquad \text{for} \qquad -W_{Dp} \le \mathrm{x} \le 0 \tag{2.8}$$

$$-\frac{d^2V_i}{dx^2} \approx \frac{qN_D}{\varepsilon_s} \qquad \text{for} \qquad 0 \le \mathrm{x} \le -W_{Dn} \tag{2.9}$$

The internal electric field is derived by integrating the Eqs. 2.8 and 2.9, as shown in Figure 2.1 (b);

$$\epsilon(x) = -\frac{qN_A(x+W_{Dp})}{\varepsilon_s} \qquad \text{for} \quad -W_{Dp} \leq x \leq 0 \qquad (2.10)$$

$$\epsilon(x) = -\epsilon_m + \frac{qN_D x}{\varepsilon_s} = -\frac{qN_D}{\varepsilon_s}(W_{Dp} - x) \qquad \text{for} \quad 0 \leq x \leq -W_{Dn} \qquad (2.11)$$

here ε_m is the maximum electric field at x=0 and is given by [47]

$$|\epsilon_m| = \frac{qN_D W_{Dn}}{\varepsilon_s} = \frac{qN_A W_{Dp}}{\varepsilon_s} \ . \qquad (2.12)$$

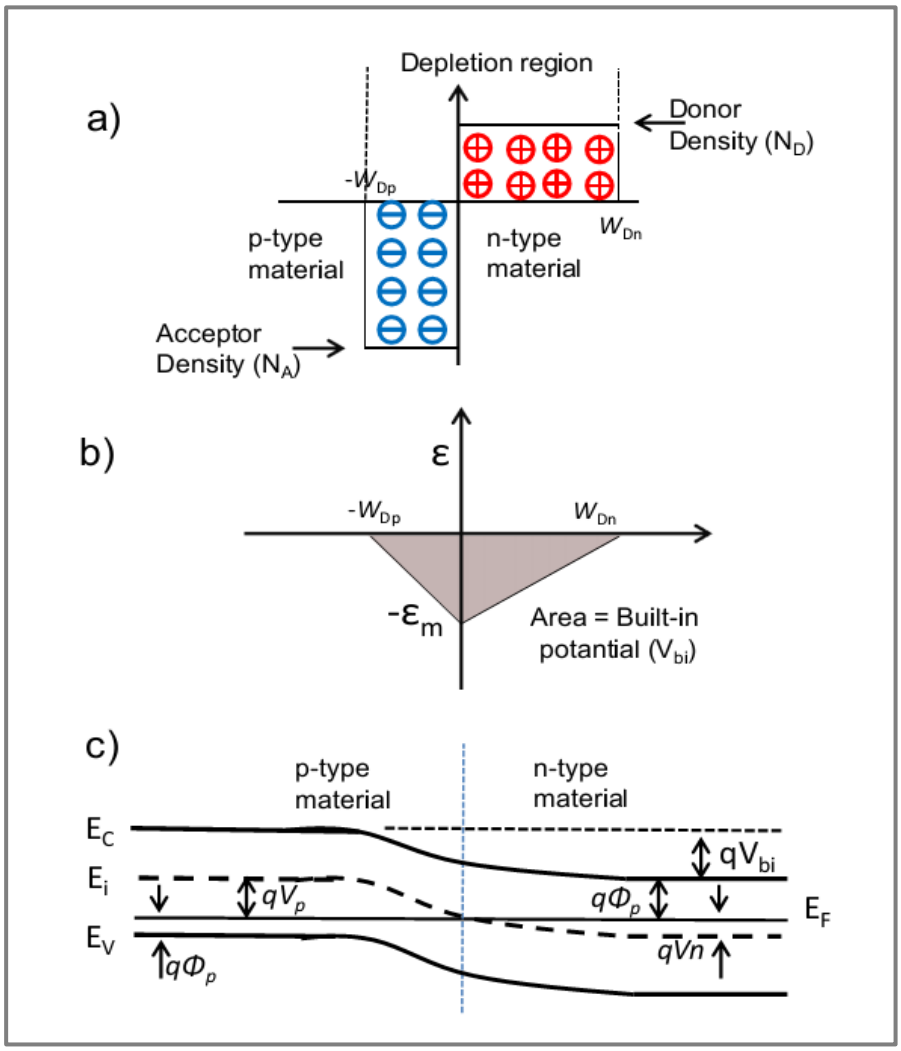

Figure 2.1 Schematic representation of a) depletion (space charge) region, b) electric field distribution, and c) energy band diagram of junction in thermal equilibrium (adopted from Ref. [47]).

2.4 Heterojunctions

A heterojunction is a p-n junction formed between two different semiconductor materials. In the case of heterojunction, devices are more complicated than homojunctions because of the semiconductor materials have different bandgap and electron affinities. The discontinuities occur in between valence band and conduction band due to band bending which is called band offset. If band offsets are very large, they act as a barrier to mobile charge carriers and can oppositely affect the current. A typical energy band diagram of a representative heterojunction is given in Figure 2.2

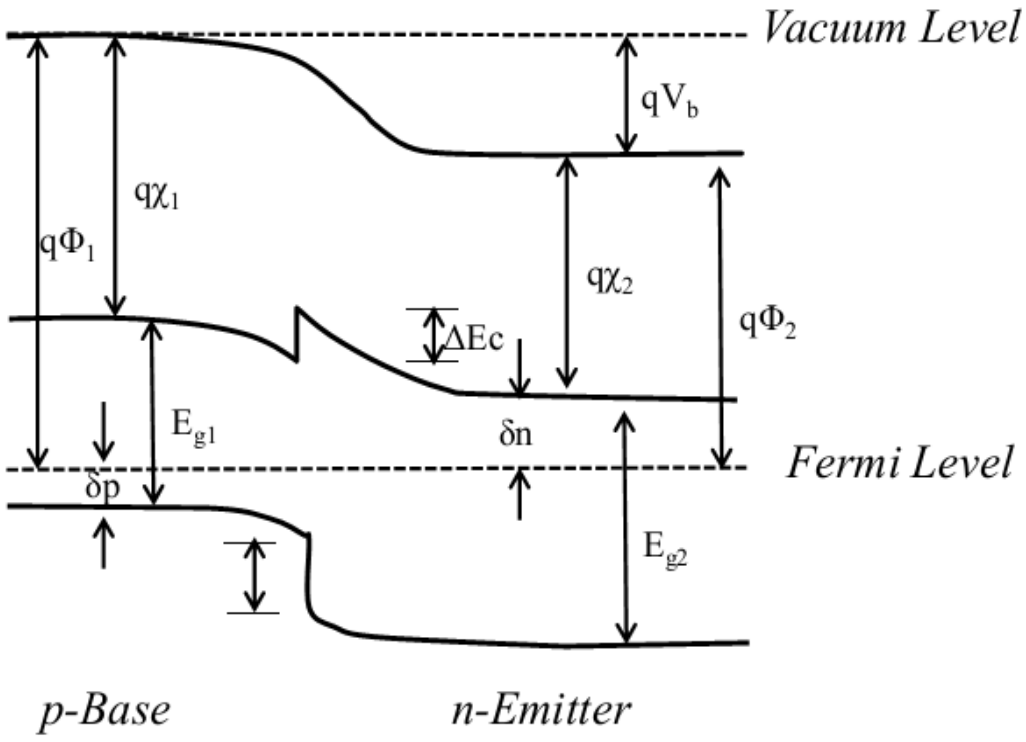

Figure 2.2 Energy band diagram of a heterojunction in thermal equilibrium [47].

In the Figure 2.2, Φ_1, E_{g1}, and χ_1 are the work function, band gap, and electron affinity for p-type semiconductor, respectively. Φ_2, E_{g2}, and χ_2 are work function, band gap, and electron affinity for n-type semiconductor, respectively. ΔEc is band

offset and it is related with discontinuity of valance band and conduction band. The band offset can be calculated by Anderson's Rule [47].

The difference in electron affinities is equal to the difference in the conduction band edges of the two semiconductors. Therefore, the band offset is,

$$\Delta E_c = \chi_2 - \chi_1. \tag{2.13}$$

Similarly, the discontinuity in valance band is given by

$$\Delta E_v = \Delta E_v - \Delta E_c = (E_{g2} - E_{g1} - \Delta E_c). \tag{2.14}$$

The extra barrier is created by band offsets of the heterojunction. This barrier increases the recombination of generated charges in the heterojunction. Therefore, in order to minimize the effect of band offset on current flow, ΔEc must be minimized by choosing closer band gaps and electron affinities.

2.5 Heterojunction under Illumination and the Photovoltaic Effect

The current (I) – voltage (V) characteristics for ideal p-n heterojunction under the dark condition is given by [47]

$$I = I_0\left[e^{qV_a/kT} - 1\right] \tag{2.15}$$

here V_a is the applied voltage and I_0 is the reverse saturation current and it is given by the following relation [47].

$$I_0 = qn_i^2\left[\frac{1}{N_A}\left(\frac{D_e}{\tau_e}\right)^{\frac{1}{2}} + \frac{1}{N_D}\left(\frac{D_h}{\tau_h}\right)^{\frac{1}{2}}\right] \tag{2.16}$$

Here n_i is the intrinsic carrier density, N_A and N_D are acceptor and donor concentrations, respectively. D_e, D_h andτ_e, τ_h are diffusion constants and life times for electrons and holes, respectively. The reverse saturation current term could also be written in terms of L_e and L_h, diffusion lengths of electrons and holes, respectively.

$$I_0 = \left(\frac{e_p L_e}{\tau_e} + \frac{h_n L_n}{\tau_n}\right) \tag{2.17}$$

here e_p and h_n are the electrons and holes concentrations in p and n regions, respectively.

When a heterojunction is exposed to the solar radiation, photons with energy higher than the band gap, E_g, interact with electrons and excite them from valance band to conduction band leaving the holes behind as shown in Figure 2.3. The photo-generated carriers, created in the built in internal electric field area, are swept away by the electrical field and set up a current through the heterojunction. Incident photons on heterojunction generate electron-hole pairs and the generation of carriers is described by the following equation.

$$G(x) = (1 - s)\ \int_{\lambda}\big(1 - r(\lambda)\big)f(\lambda)\alpha(\lambda)e^{-\alpha x}\,d\lambda \qquad (2.18)$$

Where s is the grid shadowing factor and r(λ), α(λ) , f(λ) are the reflectance, absorption co-efficient and the incident photon flux, respectively.

The illumination of heterojunction results in an increase equally in the density of electrons in the conduction band and the density of holes in the valence band. The reverse saturation current equation (Eq. 2.16) for illuminated heterojunction is given by,

$$I_0 + I_{ph} = q\left[\frac{(e_p+\Delta e)L_e}{\tau_e} + \frac{(h_p+\Delta h)L_h}{\tau_h}\right] \qquad (2.19)$$

here I_{ph} is the photocurrent and Δe and Δh are excess electrons and holes density due to the absorption of photons, respectively. The excess carrier density in equilibrium is given by,

$$\Delta e = \frac{\varphi\alpha Q\tau_e}{h\nu} = \Delta h = \frac{\varphi\alpha Q\tau_h}{h\nu} \qquad (2.20)$$

here Q is the quantum efficiency, defined as the number of excitons (electron hole pair) produced per number of absorbed photons. α and φ are the absorption coefficient and the incident photon radiation per unit area, respectively. Thus the equation of photocurrent generated by light (Eq. 2.19) under the zero bias is

$$I_{ph} = \frac{q\varphi\alpha Q}{h\nu}(L_e + L_h). \qquad (2.21)$$

Photovoltaic devices are based on the principle of p-n heterojunction. Photovoltaic conversion happens across the absorption of solar radiation to create exciton within the semiconductors. Thus, the photovoltaic effect is the generation of electricity by excitation of electron-hole pairs when the energy of incident photons greater than the band gap energy of semiconductors. In heterojunction region, the photo excited charge carriers (electrons and holes) diffuse the depletion region and internal electric field sweeps away the carriers before recombination. This process results in collection of the electrons and holes at the back and front contacts and causes photocurrent as shown in Figure 2.3.

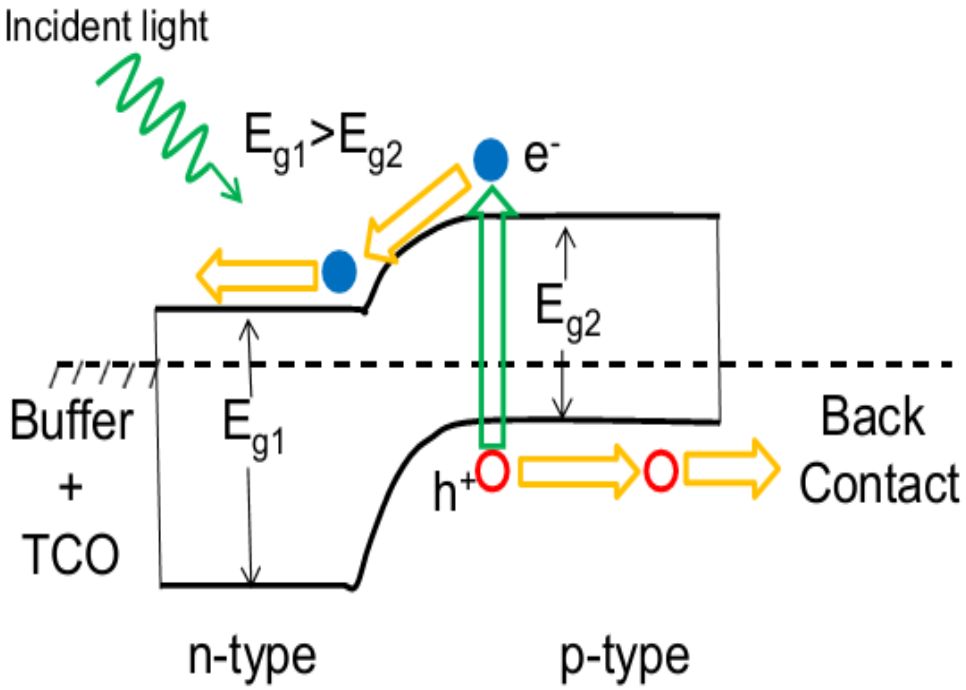

Figure 2.3 Schematic illustration of the p-n heterojunction (or solar cell) under the illumination. The band gap of n-type semiconductor is greater than the band gap of p-type semiconductor.

The well known and most commonly used photovoltaic converter device is the solar cell. The performance and the power of the solar cell depend on the properties of material, incident light, fabrication technique and layer design. The performance of

the solar cell can be analyzed over the current-voltage (I-V) characteristic. A typical current- voltage characteristic of an ideal solar cell is illustrated in Figure 2.4. There are four important photovoltaic parameters of solar cell devices which can be calculated from the current voltage characteristic under the illumination; short circuit current density (J_{sc}), open circuit voltage (V_{oc}), fill factor (FF) and efficiency (η).

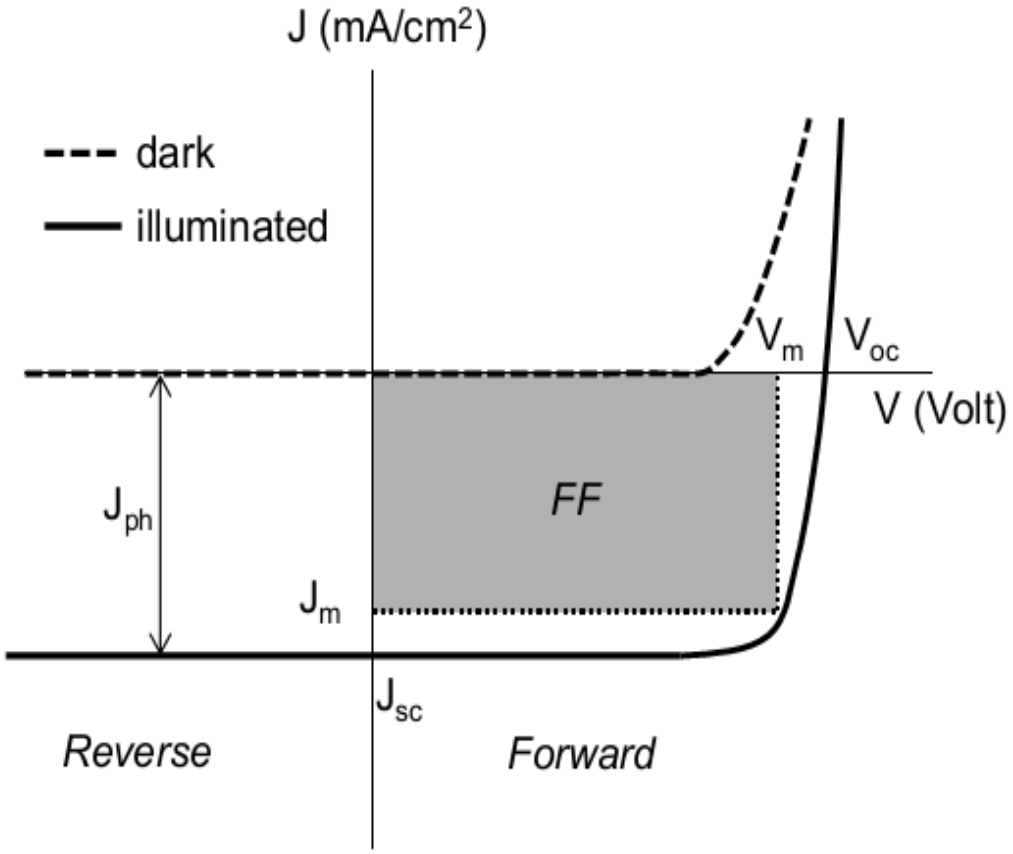

Figure 2.4 Schematic representation of current voltage characteristic of an ideal solar cell under the dark and illumination.

2.6 Solar Cell Parameters

Short -circuit current (I_{sc}) is defined as the magnitude of the photo generated current that flows through the junction under illumination when it is connected to a zero resistance and without an external bias (Eq.2.21). J_{sc} is the density of short circuit current. Ideally, J_{sc} is equal to the light generated current J_{ph} at V=0. The short circuit current increases with increase in diffusion length and lifetimes of minority carriers.

The open circuit voltage (V_{oc}) is defined as the potential difference between front and back contact under illumination and it has maximum value when the contact are isolated. Under the circumstances, there is no external current accross the solar cell and the carriers remain in the device until they recombine. For the ideal case, Voc is given by [48]

$$V_{oc} = \frac{kT}{q} \ln\left(\frac{J_{sc}}{J_0} + 1\right). \tag{2.22}$$

V_{oc} increases logarithmically with the increase in incident light intensity and photo-voltage occurs in forward bias (V>0) region.

Fill factor (*FF*) is defined as the ratio the maximum power of a cell to the produce of its V_{oc} and I_{sc} under illumination and shows the quality of solar cell. The maximum power output of an ideal device can be obtained by condition $\frac{\partial P}{\partial V} = 0$. As seen from Figure 2.4, the maximum power of *J-V* curve is product of the maximum current density (J_m) and maximum voltage (V_m).

$$P_{max} = J_m V_m \tag{2.23}$$

FF describes the squareness of *J-V* curve under the irradiation and it is calculated by the following expression [48].

$$FF = \frac{P_{max}}{J_{sc} V_{oc}} = \frac{J_m V_m}{J_{sc} V_{oc}} \tag{2.24}$$

The efficiency (η) is the energy conversion ability of solar cell and it is a fraction of maximum power output of the device to incident solar irradiation power. The efficiency (η) is given by [48]

$$\eta = \frac{P_{max}}{P_{in}} = \frac{J_m V_m}{P_{in}} = \frac{J_{sc} V_{oc}\, FF}{P_{in}} \ . \tag{2 .25}$$

here P_{in} is the incident solar irradiation power on the device. The efficiency (η) of solar cell depends on the current of photo generated carriers.

All the parameters (J_{sc}, V_{oc}, *FF*, and η) are the key parameters that define performance characteristics a solar cell and they are given above assuming the device is an ideal one. They should be defined for specific illumination conditions. Standard

Test Condition (STC) is the Air Mass 1.5 (1.5AM) spectrum, power density of 1000 W/m^2, and room temperature (25 ^oC).

2.7 Material Properties

2.7.1 The structure of Chalcopyrite Semiconductors

The chalcopyrite semiconductors have a crystal structure in the tetragonal system with a I-III-VI_2 (or A^I-B^{II}-C_2^{IV}) chemical composition and their structures are closely related to the binary zinc blende structure, which are the II-VI and III-V semiconductors. The unit cell of chalcopyrite structure can be derived from two unit cells of the zinc blende structure as shown in Figure 2.5. The column-I elements (Cu, Ag, and Au) can all occupy the same positions in the chalcopyrite crystal structure. Similarly, column-III elements (Al, Ga, and In) can hold down the same positions, and column-VI elements (S, Se, and Te) can occupy the same positions in the chalcopyrite structure. The each set of elements in parentheses can be blended in any ratio and hypothetically form a stable chalcopyrite crystal.

In the crystal structure, each cation atoms is tetrahedrally coordinated to the anion atoms [49]. The crystal structure of chalcopyrite belongs to the space group D_{2d}^{12} (eight atoms per primitive unit cell), which is the super lattice of the space group T_d^2 and the bonding between atoms is covalent (sp^3 hybrid) due to the tetrahedral coordination [49]–[51].

The unit cell of chalcopyrite is tetragonally bended with $\eta \equiv c/2a$ distortion parameter which leads to crystal-field splitting. The crystal-field splitting and tetragonal distortion are dependent on x.

For $CuIn_{1-x}Ga_xSe_2$ thin film with x> 0.1, $\eta < 1$ and $\Delta_{cf} < 0$ whereas x> 0.1, c > 1 and $\Delta_{cf} > 0$ [52].

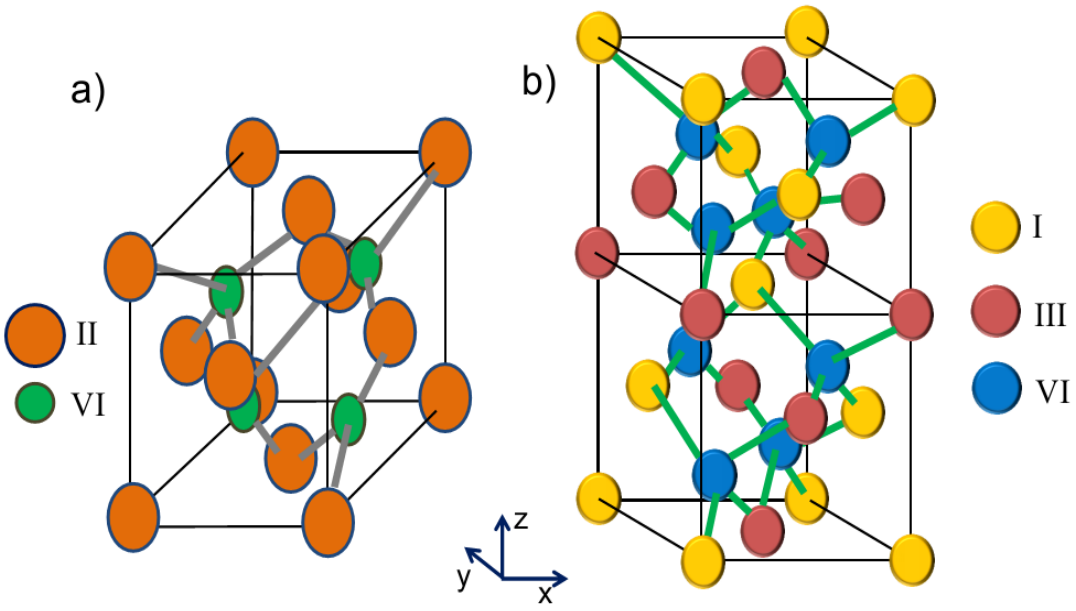

Figure 2.5 Schematic illustration of a single unit cell crystal structure of a) zinc blende and b) chalcopyrite.

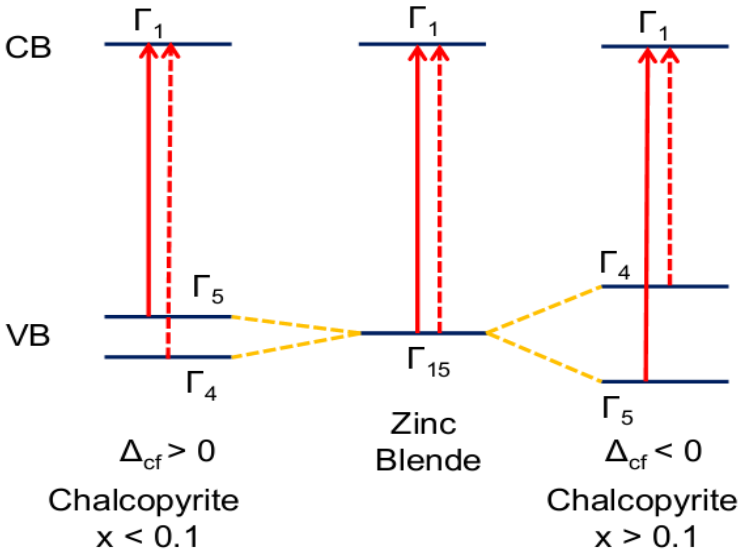

Figure 2.6 Schematic representation of the energy state at the band gap of zinc blende and chalcopyrite structures with crystal-field splitting. Solid and dashed arrows represent transition by symmetry in $E \perp c$ and $E \parallel c$ polarizations, respectively [52].

These parameters determine the structural, optical, and electrical properties of the chalcopyrite materials [50]–[54]. The schematic evaluation of crystal-field splitting is illustrated in Figure 2.6.

The crystal-field splitting parameter (Δ_{cf}) is given by

$$\Delta_{cf} = \frac{3}{2} b \left(2 - \frac{c}{a}\right). \quad (2.26)$$

where b is the negative deformation potential.

2.7.2 Properties of CIGS Thin Film

Chalcopyrite type $CuIn_{1-x}Ga_xSe_2$ (CIGS) semiconductor is a direct band gap semiconductor with a band gap in between 1.04 eV (x=0) and 1.70 eV (x=1) depending on In and Ga ratios [53], [54]. Polycrystalline thin film CIGS is one the convenient material for the high efficient PV devices due to suitable band gap and high absorption coefficient values. The highest efficiency value of polycrystalline thin film CIGS based solar cell has exceeded 21.7% [11].

Thin film materials have many advantages. They can be formed onto various substrates such as soda-lime glass, stainless-steel, polymer, and flexible plastic substrates and can be grown by various methods [55]. Additionally, the CIGS thin film based solar cells have demonstrated efficiencies with no evidence of reduction as an absorber layer with light exposure or time. They showed magnificent radiation hardness under solar irradiation [56]. The CIGS absorber layer has high absorbtion coefficient (~ 10^{-4}- 10^{-5} cm^{-1}) and adjustable direct band which makes it possible to achieve the high efficiency values in CIGS thin film based PV [57]. Moreover, the CIGS thin film based PV devices have structural tolerance to defects, impurities, and the stoichiometry in large scale. They can be manufactured a series of compounds with different Cu:(In+Ga):Se or Ga/In+Ga ratios [53], [54], [58]–[60]. The band gap of $CuInSe_2$ (x=0) (CIS) is about 1.04 eV and $CuGaSe_2$ (x=1) (CGS) is about 1.70 eV. Therefore, the band gap value of CIGS can be adjusted in between 1.04 eV and 1.70 eV depending of Ga amount [61]. The energy band gap of $CuIn_{1-x}Ga_xSe_2$ can be calculated for stoichiometric composition and Cu-poor film by the following equations, respectively [62].

$$E_g(x) = 1.011 + 0.664x - 0.249(1 - x) \quad (2.27)$$

$$E_g(x) = 1.032 + 0.71269x \quad (2.28)$$

Change in the energy band gap value as a function of Ga/(In+Ga) and In/(In+Ga) ratios (Eq.2.27) and Cu content (Eq.2.28) are plotted in Figure 2.7.

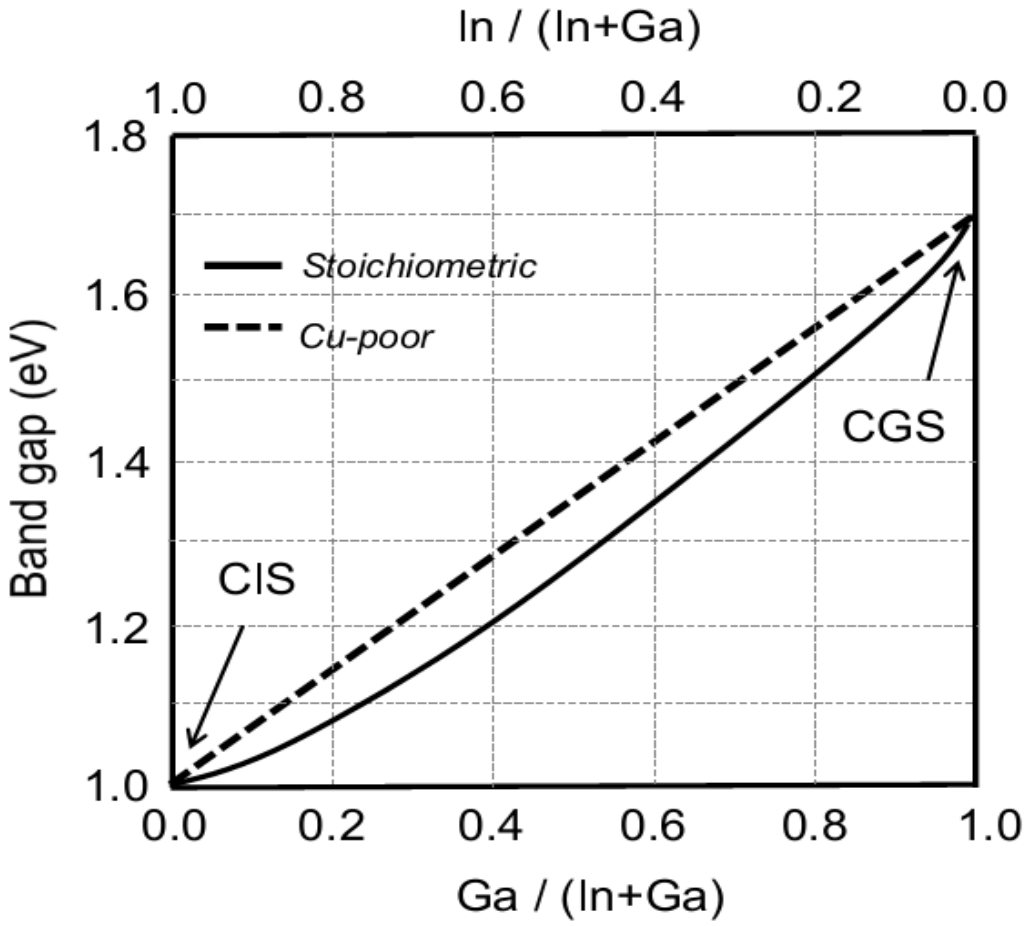

Figure 2.7 Energy band gap graph of CIGS thin film as a function of In and Ga ratios and Cu content [62].

Figure 2.8 shows a basic schematic device structure of CIGS thin film based solar cell. The layers of device are deposited by sequential fabrication. As seen from Figure 2.8, the design of the solar cell device is built up by glass/ Mo/ CIGS/ CdS/ i-ZnO/ TCO/ Al, respectively. The preferred electrical back contact is Mo because it makes a good ohmic contact to the p-type CIGS thin film layer. Additionally, a thin

interface layer of $MoSe_2$ is developed during the growth of CIGS absorber layer in between Mo and CIGS layer [63], [64]. The growth conditions of Mo layer strongly affect the characteristics of Mo/CIGS interface and the microstructure [65]. A dense Mo layer grows up when the layer is deposited at a low pressure. The dense crystalline Mo layer with intensive grain structure has a weak reactivity with Se during the CIGS layer deposition. Therefore, when the Mo layer was coated at a lower pressure, the Mo/CIGS interlayer has a thinner reaction layer of $MoSe_2$ [63].

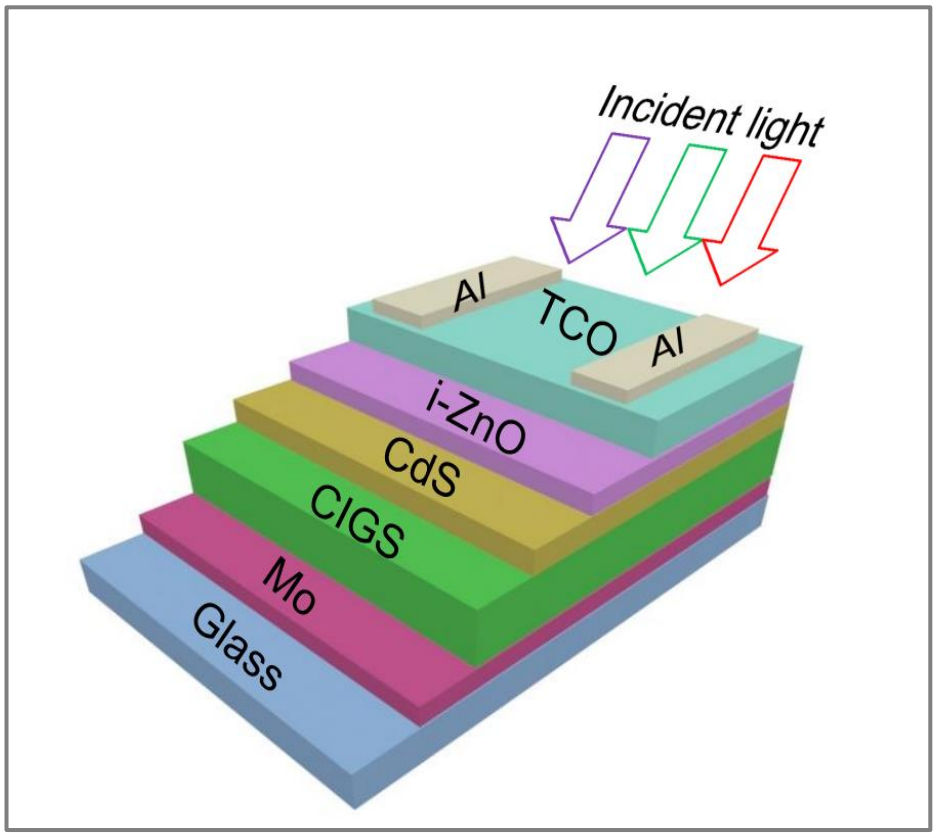

Figure 2.8 Schematic illustration of the complete CIGS thin film based solar cell.

The p-type CIGS thin film layer, where the absorption of the photons takes place, is the main part of the solar cell. N-type CdS thin film buffer layer is deposited on top of the CIGS layer [66]. The p-n heterojunction is formed between the absorber and buffer layers, which leads to bending of conduction and valence bands. The absorber

layer divides into a majority charge carrier depleted space charge region (depletion region) and a quasi-neutral region as shown in Figure 2.9. Incoming photons with higher energy than the band gap of CIGS which changes between 1.04 eV and 1.70 eV are mostly absorbed within the first micrometer of the absorber layer which creates excitons (electron-hole pairs) [67]. The electrons and holes are separated by the internal electric field and optimal collection of minority carriers (electrons) from p-type absorber layer is crucial for achieving high efficiency values.

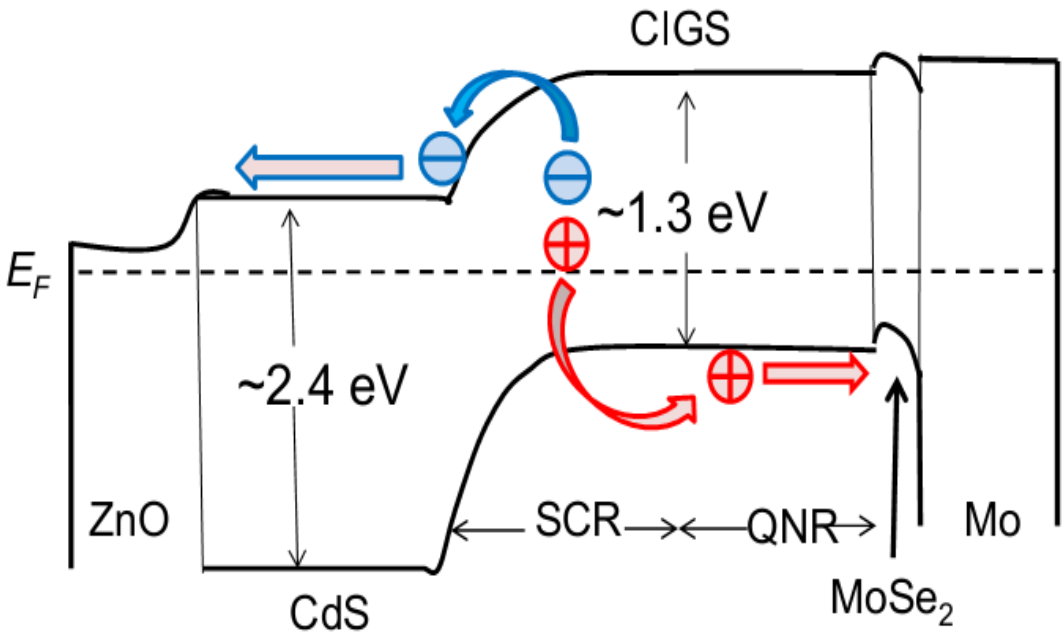

Figure 2.9 Schematic band diagram of a CIGS thin film based solar cell under zero-bias voltage condition. Indicated as well are the $MoSe_2$ interface layer, the Fermi level E_F, space charge region (*SCR*) and quasi-neutral region (*QNR*).

CHAPTER 3

QUANTUM DOTS

3.1 Introduction

In a bulk semiconductor material, the energy levels are closely spaced levels that form bands and the number of available energy levels is described as the density of state (DOS). The highest energy molecular orbital occupied band, known as valance band, is mostly filled and the lowest energy molecular orbital unoccupied band, known as conduction band, is mostly empty and there is a level called Fermi level between them. The valance and conduction bands are separated by a band gap. The valence band electrons are not free and cannot move to conduction band because they are bonded by Coulomb forces. When an electron in the valence band obtains enough energy that is greater than or equal to band gap energy level, the electron can move from the valance band to the conduction band. This process creates an electron and hole pair (exciton) in the conduction and valance bands, respectively. The hole can be filled easily by another electron in the valence band and it seems like a moving positive electron in the valance band. The electron and hole are also attracted to each other by the Coulomb force but the pair can move freely in lattice of the bulk semiconductor. On the other hand, if semiconductor is reduced in size to a few hundred atoms scale, the properties of semiconductor can be changed intensely. Zero dimensional ("0D") particles, known as quantum dots (QDs), were first discovered in 1980 by Ekimov and Onushchenko [68]. The term "quantum dots" (QDs) refers to nanocrystal or particle of semiconductor nano-structure or nano-particle and widely used from 1980s [69]. Typical size of colloidal QD ranges from 2 to 10 nanometers in diameter, so that on average they contain 10 to 50 atoms.

This chapter describes the properties of quantum dots and also quantum confinement effects, up conversion, down conversion, and multi exciton generation (MEG) phenomenon will be explained in detail.

3.2 Properties of Quantum Dots

The value and property of the energy band gap (E_g) of the bulk semiconductor which is fixed and determined by the materials property changes for the nanoscale particles such as quantum dots with sizes less than ~10 nm [70]. The quantum confinement of carriers leads to size-dependent electronic energy levels and density of states reduced to a set of delta functions [71]. The size-dependence of energy levels suggests the flexibility to manage the optical and electric properties of semiconductor QDs. The effective bandgap energy of QDs can be arranged by changing the physical dimensions of the QDs as shown in Figure 3.1. The calculation of effective E_g for spherical QDs, which changes with radius (R), was calculated by Louis Brus in 1986. The equation of Brus is given by [72]

$$E_g^{QD}(R) = E_g + \frac{\hbar^2\pi^2}{2R^2}\left[\frac{1}{m_e^*} + \frac{1}{m_h^*}\right] - \frac{1.8e}{\varepsilon R} \tag{3.1}$$

here, Eg and ε are the band gap and the dielectric constant of the QD material, respectively, R is the QD radius, ħ is Plank's constant, m_e^* is the effective mass of electron, and m_h^* is the effective mass of hole. As clearly seen from equation, the effective band gap of semiconductor QD material is proportional to R^{-2} in second term and R^{-1} in third term. The second term is quantum confinement energy of the electrons and the holes and it increases with decreasing R. The third term in equation is Coulomb attraction of the electrons and the holes [73]. If R is sufficiently small, the Coulomb term dominates the equation and E_g shifts to lower energy. Many improvements have been done to Brus' model, but this model is the basis of much of the theoretical work on the semiconductor QDs [74].

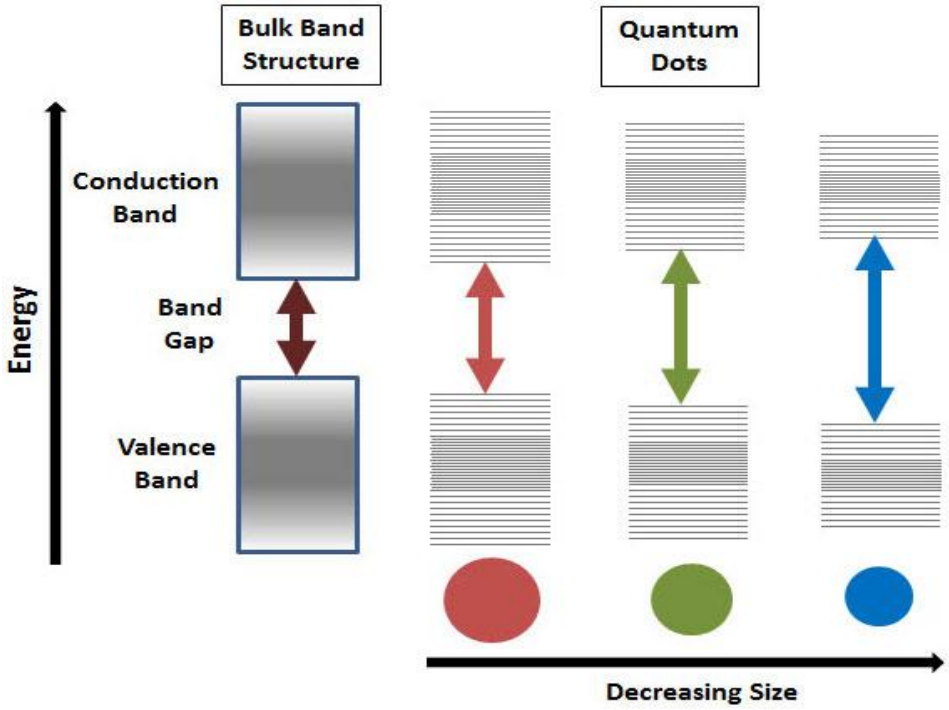

Figure 3.1 Schematic representation of changing in the band gap energy according to the quantum dots size (from ref. [75]).

3.3 Quantum Confinement Effect

In contrast to materials with dimensional structures, such as bulk materials, quantum wells and quantum wires for which the density of state (DOS) has a continuum in energy states, the electron energy spectra in semiconductors QDs with conduction electrons are consist of a series of sub-bands and the profile of the confining potential determines the distances between sub-bands. Therefore, QDs have atomic like discrete energy states and the spectrum is continuous and these continuous spectra overlap inside each sub-band. DOS, physical quantity characterizing the occupation, of an individual QD is convenient to characterize these spectra. The DOS for three dimensions (3D) bulk semiconductor is given by

$$\rho_{3D}(E) = \left(\frac{m^*}{\hbar^2}\right)^{3/2} \frac{V}{\pi^2}\sqrt{2E} \tag{3.2}$$

Here, m* is the effective mass of electron and V is the volume of bulk crystal material [76].

The DOS for two dimensional (2D) materials such as quantum well is given by

$$\rho_{2D}(E) = \frac{Sm^*}{\pi\hbar^2} \sum_{l_3} \Theta(E - \varepsilon l_3) \tag{3.3}$$

here, S is the surface area of 2D material, l_3 is a quantum number, and Θ(x) is the Heaviside step-function, defined by [77]

$$\Theta(x) = \begin{cases} 1, & for\ x > 0, \\ 0, & for\ x < 0. \end{cases} \tag{3.4}$$

The DOS for one dimensional (1D) materials such as nanowire is given by

$$\rho_{1D}(E) = \sum_{l_2,l_3} \rho_{l_2,l_3}(E) \tag{3.5}$$

where

$$\rho_{l_2,l_3}(E) = \frac{L}{\pi}\left(\frac{2m^*}{\hbar^2}\right)^{1/2} \frac{1}{\sqrt{E-\varepsilon_{l_2,l_3}}}\ \Theta\left(E - \varepsilon_{l_2,l_3}\right) \tag{3.6}$$

Therefore, the DOS for 1D material;

$$\rho_{1D}(E) = \frac{L}{\pi}\left(\frac{2m^*}{\hbar^2}\right)^{1/2} \sum_{l_2,l_3} \frac{1}{\sqrt{E-\varepsilon_{l_2,l_3}}} \Theta\left(E - \varepsilon_{l_2,l_3}\right) \tag{3.7}$$

here, L is the length of the nanowire.

In the case of quantum dots which are zero-dimensional (0D), the spectra are discrete and the DOS is just dependent on the number of the limited levels [76]. According to the definition of Pauli principle, two identical electrons cannot occupy the same state simultaneously and only two states exist at each energy level. Therefore, the DOS is simply a set of δ-shaped peaks in the case of 0D, which is given by

$$\rho_{0D}(E) = \sum_m \delta(E - \varepsilon_m) \tag{3.8}$$

here, ε_m is the energy associated with the quantum state *m*, and Dirac's δ-function:

$$\delta(x) = \begin{cases} 0, & for\ x \neq 0, \\ \infty, & for\ x \to 0. \end{cases} \tag{3.9}$$

Figure 3.2 shows schematically the DOS of bulk crystal (3D), quantum well (2D), nanowire (1D), and quantum dot (0D).

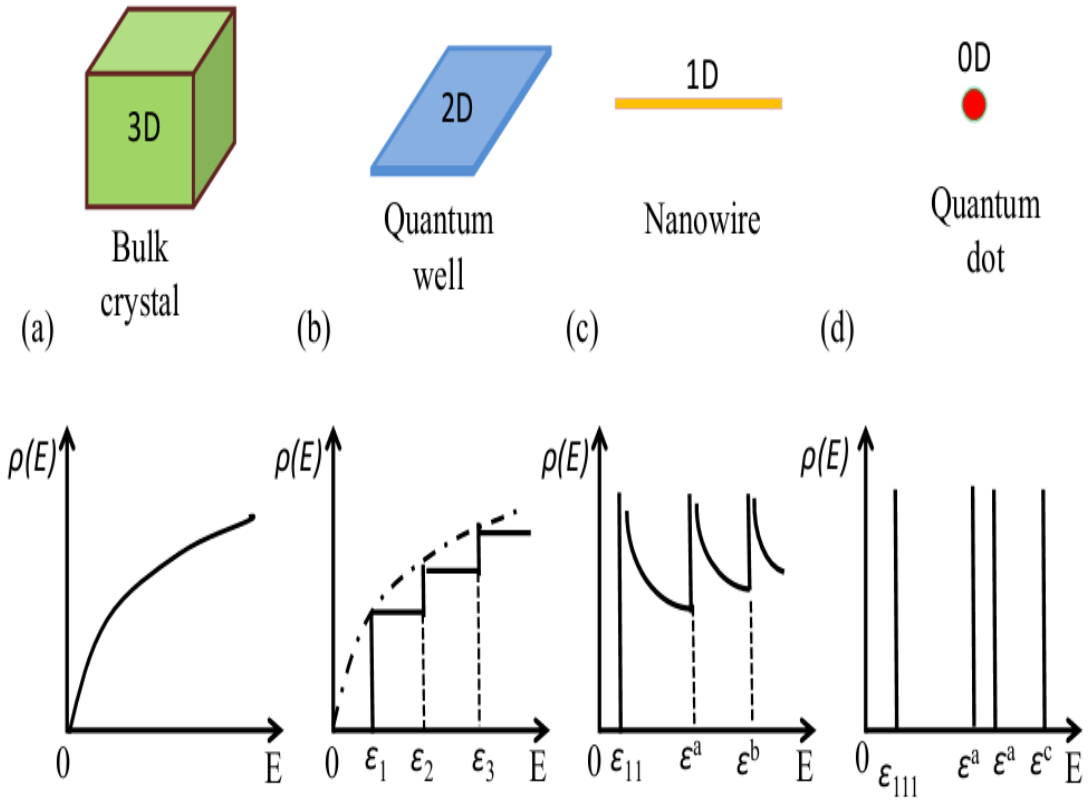

Figure 3.2 The density of states (DOS) of electrons, ρ(E), in systems of different dimensionalities. (a) a bulk crystal (3D), (b) a quantum well (2D), (c) a nanowire (1D), and (d) a quantum dot (0D). The ground states are represented as ε_1, ε_{11}, and ε_{111} in a quantum well, nanowire, and quantum dot, respectively. ε_2 and ε_3 are higher states in a quantum well and ε^a, ε^b, and ε^c are higher states in a nanowire and in a quantum dot (adapted from Ref. [76]).

3.4 Up Conversion and Down Conversion

Semiconductors have the discrete band structure and photons can be absorbed by the semiconductor if the energy of photon equal or greater than the band gap energy E_g of semiconductor. The absorption in the semiconductor is restricted by band gap values. Photons with higher energy than band gap energy, although absorbed, rapidly

thermalize to the conduction band edge of semiconductors [78]. Therefore, the energy of this kind of photon is converted to thermal energy and lost within the lattice of the semiconductor. Photons with lower energy than E_g value are transmitted through the semiconductor and do not contribute to the carriers excitation. There are two ways to minimize the energy losses due to the thermalization of excess photons by adjusting the solar spectrum: up conversion or down conversion processes. The up conversion process can generate one high energy photon for every two or more incident low energy photons and the down conversion process can generate two or more low energy photons for one incident photon [79], [80]. Up conversion and down conversion processes are both non-linear optical effects. The up conversion process can be used to convert the lower incident photon energy (such as near-IR) into the high energy emission (such as visible) and the down conversion process can be used to convert higher incident photon energy into the low energy emitted radiation (such as visible). Figure 3.3 shows the solar radiation spectrum and schematic representation of up and down conversion processes. The early proposal about up conversion idea was made by Bloembergen in 1959 which was then discovered by Auzel, Ovsyankin and P.P. Feofilov in 1966 [81]–[83]. Since then, many researches have focused on the up and down conversion materials because of their potential for optical manipulation in optoelectronic devices such as temperature sensors, solid state laser, and infrared quantum counter detectors, temperature sensors, compact solid-state, medical therapy, bio-analysis, and photovoltaic solar cells to harvest the light [84]–[87].

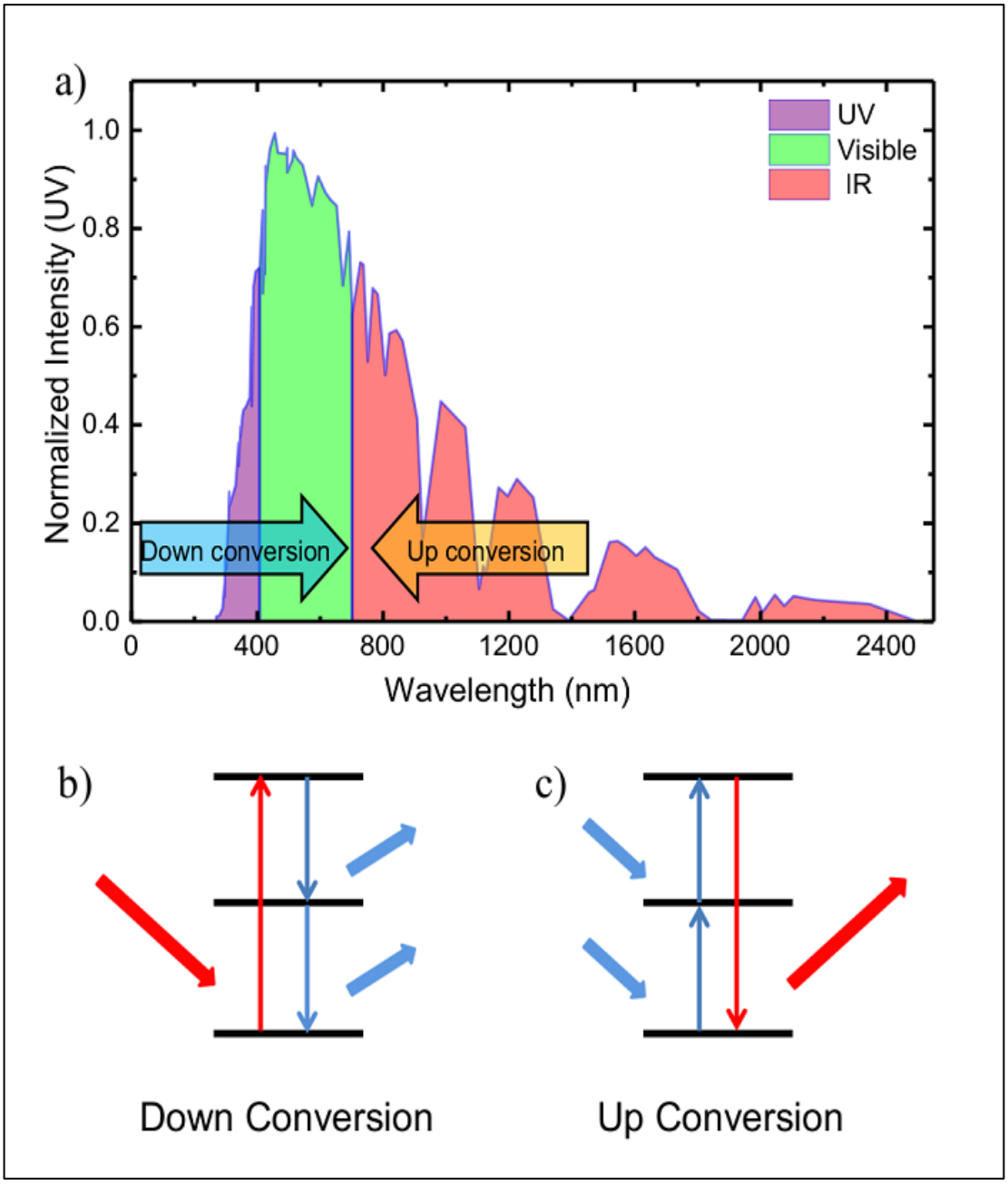

Figure 3.3 a) Solar radiation spectrum showing the down and up conversion shifts. And schematic representations of b) down conversion by sequential emission of two photons, c) up conversion with first absorption followed by second state absorption.

2.4 Multi Exciton Generations (MEG)

Inter band transitions between valence band and conduction band determine the optical properties of the bulk semiconductors. In classical semiconductor theory, one photon can excite only one electron-hole pairs if the energy of photon is equal or greater than the band gap (Eg) energy value of semiconductor. The excess energy is lost as the carriers cool or relax to the band edge of bulk semiconductors, mainly by phonon emission and scattering, becoming waste heat [78], [88]. Most of the incident energy (~47%) is lost in this way for a conventional solar cell especially in single junction silicon solar cells [89]. If this energy lost as heat can be reduced or prevented, the efficiency of solar cell would be significantly improved [90]. Impact ionization is a process for which some or all excess energy of the excited electron, having kinetic energy more than semiconductor band gap, generates the second electron form the valance band electrons and creates a new free electron-hole pairs [91]. However, impact ionization process cannot contribute to the efficiency value of solar cells because the efficiency of impact ionization does not reach the meaningful value until photon energies access to UV region of the spectrum due to the exciton-exciton annihilation which is called Auger recombination [88]. Additionally, the excess energy of photon for impact ionization exceeds that needed for energy conservation and crystal momentum must be conserved in the bulk semiconductor. Moreover, the rate of impact ionization has to compete with the rate of electron-phonon relaxation, whereas electron-phonon scattering rate is faster than the rate of impact ionization in the bulk semiconductors [92]–[94]. Figure 3.4 (a) shows the hot electron-hole pairs relaxation/cooling process in the bulk semiconductors. On the other hand, in semiconductor nanocrystals which are called quantum dots (QDs), a single atom can generate multiple electron-holes pairs which are called multi exciton generation (MEG) or carrier multiplication (CM) process due to quantum size effect. This process becomes very efficient and the threshold photon energy for the process to generate two or more electron–hole pairs (excitons) per photon can approach values of twice or more than the threshold energy for absorption. The absolute minimum satisfies energy conservation and this effect permits the threshold to happen in the IR or visible spectral regions [95]. The nanoscale dimensions of QDs can restrict the wave functions of free electrons and holes so that the valance band and conduction band turn into discretized into the distinct energy levels.

Additionally, the separation among energy levels increases as the QD size decreases and the separations become greater than the phonon energy such that cooling or relaxation by phonon emission must take place by a much less probably multi-phonon process [90]. The first direct evidence of the MEG process was observed experimentally by a group of researchers from National Renewable Energy Laboratory (NREL) - Colorado in 2011 [22]. They reported that about 4% of total photocurrent in lead selenide (PbSe) QD based solar cells derives from the MEG effect. The MEG effect measurements were performed by determining the external quantum efficiency (EQE) and internal quantum efficiency (IQE) of solar cell at zero applied bias voltage. As a result of measurements, the peaks of EQE and IQE were obtained as 114% and 130%, respectively [22]. The discovering direct evidence for MEG is important because it shows that the yield of MEG can be collected in suitable designed solar cells. The MEG has a considerable impact on photovoltaic devices, QD thin film inside solar cell structures can generate multiple excitons per photon at wavelength near the solar peak and develop the efficiency value of devices in the future. The schematic illustration of MEG process is given in the Figure 3.4 (b).

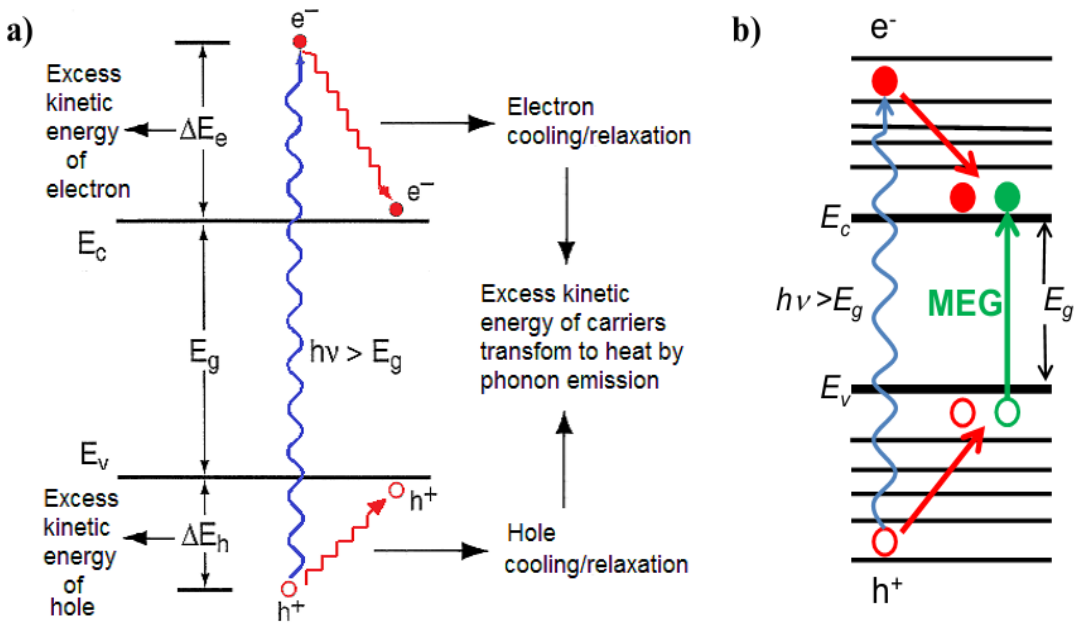

Figure 3.4 Schematic illustration of a) the hot electron-hole pairs relaxation/cooling as heat by phonon emission (adapted from ref [74]), and b) MEG process

.

CHAPTER 4

ORGANIC SOLAR CELLS

4.1 Introduction

Organic semiconductors based thin film solar cells have attracted much attention in the past decades. They are mainly based on the organic material, such as polymers, molecules and oligomer. They are significantly safe to environment due to most of the elements of organic semiconductors are carbon (C), hydrogen (H) and oxygen (O). Organic semiconductors based thin film solar cells are promising for several reasons. First of all, the electrical and chemical properties of organic semiconductors can be ordered by adjusting the chemical structure of the organic compounds in infinite combinations. Therefore, the organic semiconductors can be synthesized without concerning on the limit of source materials. The second reason, organic semiconductors can be deposited at high or low temperature and also they can be coated with several techniques like spin coating, spraying or printing processes. Spin coat, spray and print processings, atomic and molecular layer depositions, are the techniques with low manufacturing costs since there no need of high temperature and vacuum methods [96]–[99]. Additionally, organic semiconductors have high absorption coefficient and a few hundred nanometers film thickness is enough to absorb the photons in the abortion range of materials. The use of such organic materials reduces the production cost of solar cells. Finally, the organic materials can be used to build the flexible and semi-transparent solar cell devices. Consequently, organic semiconductor based thin film solar cells, with easy and low-cost production, wide application area, and environmental friendly components, are expected to be the next step in solar cell technology.

This chapter will give the detail descriptions about the chemical and physical properties of organic semiconductors and also conventional and inverted polymer solar cells will be described.

4.2 Properties of Organic Semiconductors

A carbon atom has 6 electrons and it has electronic configuration $1s^2 2s^2 2p^2$. Therefore, the carbon atom can make σ-bonds with neighbor carbon atoms or hydrogens. Carbon atoms have three strong σ-bonds and one weak π-bond due to sp^2 hybridization form. This bond structure gives the conjugates organic semiconductor a quasi-one dimensional structure form [100]. The conjugated π-electrons are basis of the electronic structure of all organic semiconductors and a typical conjugated organic system are composed of organic molecules of a sequence of single (σ-bond) and double (π-bond) carbon-carbon bonds [101]. When photon is absorbed by the conjugated organic polymer, electron-hole pair is created by transition of an electron from the π-orbital to the π*-orbital. On the other hand, the conjugated polymers are not soluble in most solvents due to the rigid bonding structure. Therefore, the side chains are added to the organic polymer structures and their solubility increase for solution-process applications. Moreover, the crystallization of polymers and carrier mobility are also improved by adding side chains [102].

The band gap (Eg) of photoactive layer is determined by the energy difference between the highest occupied molecular orbital (HOMO) level and lowest unoccupied molecular orbital (LUMO) level of material. The organic semiconductors can be p-doped by removing electron from the HOMO and can be n-doped by adding electrons to the LUMO. The band gap of organic polymer materials ranges from 1 to 4 eV [101]. In conventional polymer solar cells, the transparent electrode is mostly made up of ITO and PEDOT:PSS as a TCO and it needs to be at least 80% or more transmissivity in the visible range of spectrum in order to pass enough photons can be delivered to the photoactive layer [103]. Macroscopically, inorganic solar cells and organic solar cells have same behavior so that current-voltage (I-V) characteristics of organic solar cells can be represented with the ideal diode equation [104]. However, photo conversion mechanism in organic solar cells works very differently from the inorganic solar cells. The electron-hole pairs are only generated

in the photoactive layer by absorption of photons. Internal electric fields across the photoactive layer drives the charge carriers and the electrons and holes are collected by top and bottom electrodes due to the different work functions [105]. These excitons have diffusion length generally limited in between 5 nm and 20 nm and they can diffuse from molecule to molecule during their lifetime and afterward either separate to form free electrons and free holes or decay by recombination [106]–[108]. These excitons have to be dissociated before the carriers transport and then can be collected at the top and bottom electrodes. In order to collect the excitons, the energy level offset between the HOMOs of donors or the LUMOs of acceptors must be properly arranged. If the level between the HOMO and the LUMO is large enough to overcome the Coulombic attraction which is holding the exciton together, the electron and hole separation will be possible [105].

4.3 Structures of Organic Solar Cell

There are two types of organic solar cell structures, namely conventional polymer solar cell (CPSC) and inverted polymer solar cell (IPCS). The main differences between them are based on the opposite layer order. The CPSC has electron blocking layer between transparent electrode layer and photoactive layer while the IPCS having hole blocking layer in same place. Previously in organic solar cells, photoactive layer was produced from two different layers of donor and acceptor materials and this architecture was called bilayer heterojunction architecture. Individual organic p-type donor material and organic n-type acceptor material were used to form the heterojunction, analogous to a p-n junction in inorganic counterpart. However, the energy offset between the HOMO of donor material and the LUMO of acceptor material results inefficient exciton dissociation and photo induced charge transfer between layers due to short diffusion length of excitons. In order to overcome the limitation of the bilayer polymer solar cells, the concept of bulk heterojunction (BHJ) in polymer photovoltaics was suggested by Yu et al. from University of California- Santa Barbara (UCSB) in 1995 [109]. The photoactive layer has generally been made from a blended electron rich conjugated p-type organic material as a donor and electron deficient fullerene based n-type organic material as an acceptor to form a bulk heterojunction (BHJ) layer. In this photoactive layer,

photo generated excitons, being present everywhere in donor - acceptor interface, are within a couple of nanometers dissociate and form into free electrons and holes. Therefore, almost all the photo-generated excitons can be separated into free electrons and holes, and these free carriers move through the BHJ layer and reach the electron and holes collector electrodes to generate photocurrent. Additionally, the difference in the work function of organic component materials provides an electrical field inside photoactive layer that drives electrons flow to the low work function metal electrode (cathode) and holes to the high work function metal electrode (anode) from the blended organic active layer. On the other hand, the charge collection is directly affected by the nature of the interfaces between the photoactive layer and the electrodes. Theoretically, the contacts between photo active layer and the anode or the cathode should be ohmic. The contact resistances are very low and negligible relative to the resistance of the bulk organic materials [110]. As a result, the achitecture of organic solar cell, materials competibility, and the order of layers are very important factor to travel and to collect the exitons in electrodes, efficiently.

4.4. Device Configuration

A typical conventional polymer solar cell consists of the organic photoactive layer sandwiched as a thin film between top buffer cathode layer (BCL), mainly calcium (Ca) thin film, and bottom anode buffer layer (ABL), mainly PEDOT:PSS, a kind of polymer film. The long-term stability of PV devices is an important factor for their commercial applicability. The conventional architecture degrades the device performance due to the fact that the low work-function metal electrode of Ca and Al. These metals are easily oxidized and they affect the performance of the conventional devices [111]. On the other hand, the inverted polymer ZnO and MoO_3 thin film layers are used as a CBL and ABL instead of Ca and PEDOT:PSS layers, respectively. The order of layers are also reversed in inverted architecture, CBL is under the photoactive layer and ABL is on the photoactive layer while in the conventional architecture CBL and ABL layer are opposite places. The first inverted polymer solar cell was prepared by Shirakawa et al. from Osaka University in 2004. They used a ZnO layer as hole blocking layer and a gold layer as top anode electrode [112]. Figure 4.1 (a) and (b) show the conventional and inverted architectures of

polymer solar cells, respectively. The conventional polymer solar cell geometry has the following structure: glass substrate/ITO/hole-injecting layer/ blended photoactive layer/electron-injecting layer/ top cathode. The inverted polymer solar cell geometry has the following structure: glass substrate/ ITO/ electron-injecting layer/ blended photoactive layer/ hole-injecting layer/ top anode.

Power conversion efficiencies (PCE) and stability are markedly increased in IPSC devices compared to CPSC counterparts.

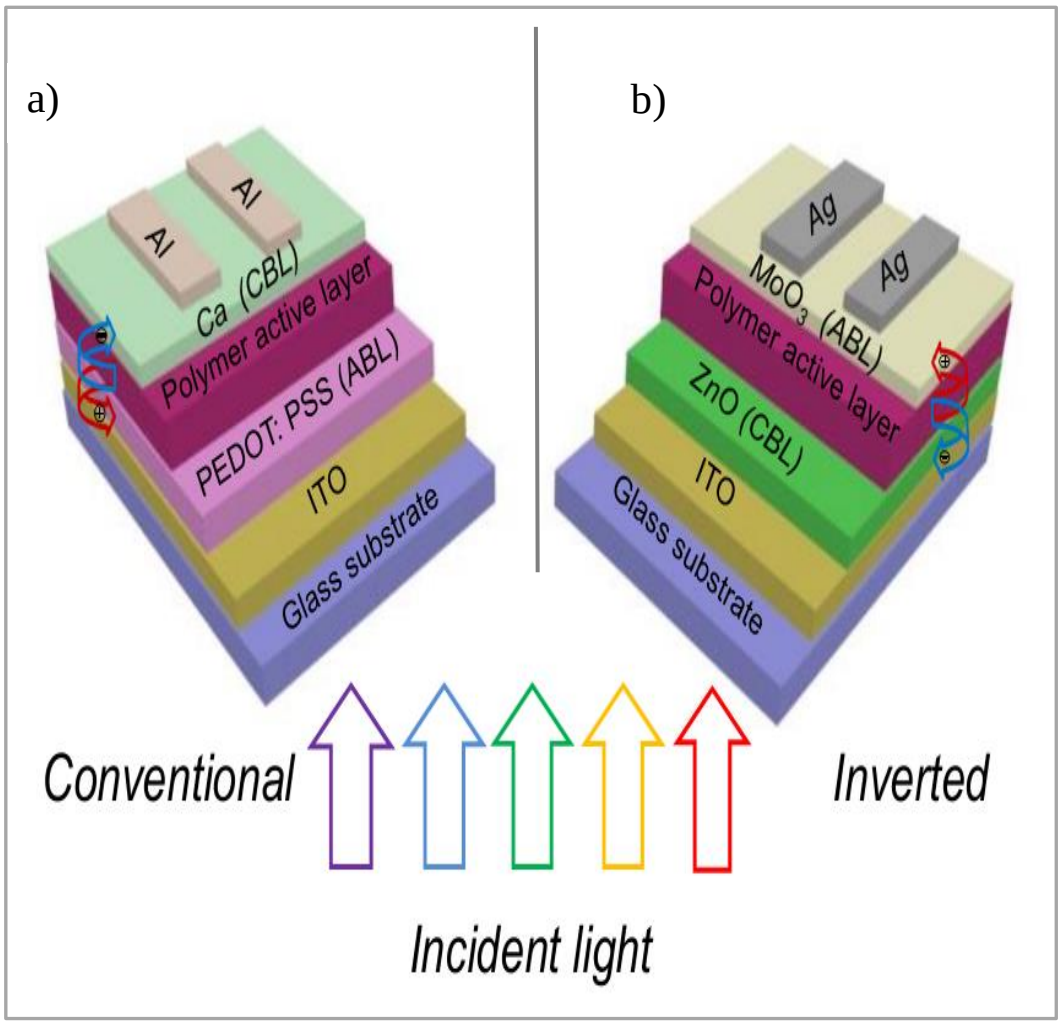

Figure 4.1 Device structures of conventional polymer solar cell (CPSC) and inverted polymer solar cell (IPSC).

4.5 P3HT and PCBM Organic Semiconductors

The blend of Poly (3-hexylthiophene-2, 5-diyl) (P3HT) and poly (6, 6-phenyl C61-butyric acid methyl ester) (PCBM) organic semiconductors are the most widely studied conducting donor and acceptor polymers, respectively.

P3HT is one of the best conjugated polymers that are stable and efficient. It has HOMO level around -5.2 eV and LUMO level around -3.5 eV [113]. The bandgap value of P3HT is reported in between 1.7 and 2.1 eV [114], [115]. This polymer can be easily doped by removing or adding electrons from the π-orbital. In the literature, the carrier concentration value of P3HT is given in between 10^{15} and 10^{17} cm^{-3} [116] and it has a hole mobility value around $3x10^{-4}$ $cm^2.V^{-1}.s^{-1}$ at room temperature conditions [117].

Fullerene and its derivatives are generally used as an acceptor in polymer solar cells. It has high mobility value and also has relatively long exciton diffusion length in pure material [118]. PCBM is a fullerene derivative and is a commonly used for photoactive layer of polymer solar cells as an n-type semiconductor with p-type P3HT due to its high electron mobility around $4.5.10^{-3}$ $cm^2.V^{-1}.s^{-1}$ [119]. The HOMO and the LUMO levels of PCBM are around -6.1 eV and -3.7 eV, respectively [113]. The bandgap value of PCBM is reported in between 2.48 and 2.85 eV [120]. The molecular structures and energy level diagrams of donor (P3HT) and acceptor (PCBM) organic semiconductor materials are illustrated in Figure 4.2. Both P3HT and PCBM polymers are soluble in chloroform, chlorobenzene, dichlorobenzene, toluene, and similar organic solvents. These properties of P3HT and PCBM polymers make them the perfect candidate for BHJ photoactive layer.

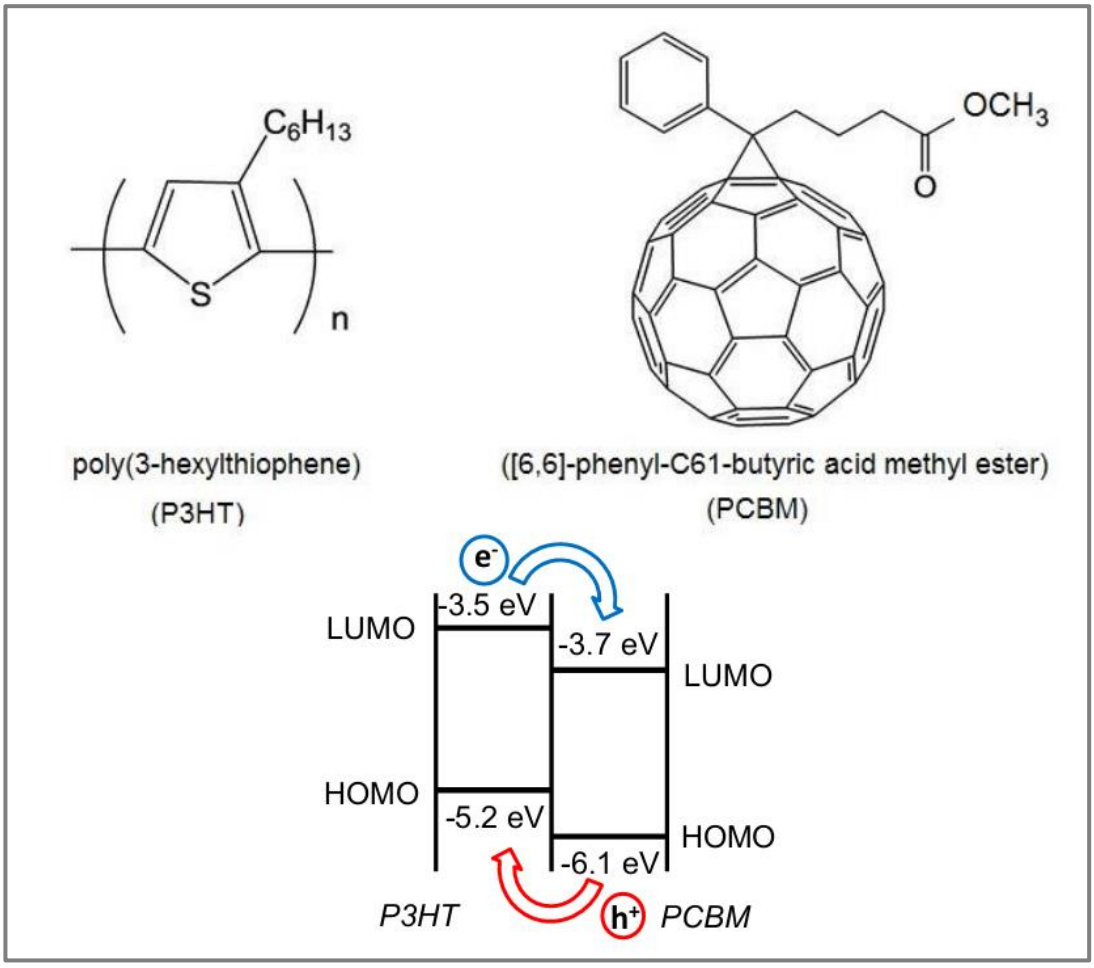

Figure 4.2 The molecular structures and energy level diagrams of n-type P3HT and p-type PCBM organic semiconductors (adapted from ref [113], [121]).

CHAPTER 5

EXPERIMENTAL TECHNIQUES

5.1 Introduction

In this chapter, the details of the preparation and deposition of $CuIn_{1-x}Ga_xSe_2$ (CIGS) thin film, CIGS and QDs layer, polymer solar cell, quantum dots are presented. It gives brief information about the physical nature of the methods and techniques which were used during the deposition, physical improvement and characterization of the thin film based and polymer based solar cell devices.

The sections which will be presented this chapter are organized as follows. Firstly, the deposition process of CIGS thin film by using thermal evaporation technique is introduced. Secondly, the preparation of CIGS and quantum dot (CIGS/QDs) layers to check the QDs effects in the inorganic solar cell structure will be detailed. This section is followed by a brief introduction of basic structural, electric, and optical characterization techniques and systems for thin films. Then, the preparation and deposition of P3HT:PCBM polymer solution and polymer active layer are presented. And then, the deposition and characterization techniques of PbS QDs are given. Finally, the characterization techniques of inorganic and organic solar cells are introduced.

5.2 Deposition of CIGS and CIGS/QDs Thin Films

5.2.1 Substrate Preparation

The deposition of CIGS thin film was carried out by using thermal evaporation technique from elemental sources. In order to analyze the film and device properties,

soda-lime glass, n-type Si (111) wafers having resistivity 1-3 (Ω.cm) were used as substrates for the deposition of p-type CIGS thin films. It is well known that the soda-lime glass satisfy many physical properties such as; transparent to visible light, suitable thermal expansion coefficient for chalcopyrite compounds, thermal survival up to 550 ^{o}C, mechanical rigidity, a good isolator, ideal for recycling, and sufficient surface smoothness [122]–[124]. It is also low cost material and available in large quantities. The sizes of the substrates were prepared as square forms with dimensions 10 mm x 10 mm and 20mm x 20mm that have compatible the substrate holder of evaporator. Cleaning process of the substrates is an important step to eliminate the contaminations before thin film coating process. Otherwise, the contaminants on the substrate surface would possibly diffuse in the thin film which results in instabilities and unsuitable thin film properties [125]. The cleaning of soda lime glass and ITO glass substrates was performed by the following several cleaning steps to remove the organic and inorganic contaminations on the surface onto which the thin film will be deposited. The main steps of substrate cleaning procedure are summarized as follows;

- The substrates were kept in a dilute solution of chemical detergent prepared from highly pure deionized water (DI water) at temperature of about 100 ^{o}C in an ultrasonic bath for 15 minutes to eliminate the unwanted organic molecules from the surface.

- The substrates were washed with boiling DI water in order to eliminate the possible residue left from previous cleaning stage due to detergent solution.

- In order to remove inorganic contaminations, substrates were transferred into the hydrogen peroxide (H_2O_2) solution, diluted with boiling DI water, nearly for 15 minutes and simultaneously the same solution were placed into ultrasonic bath for the same period of time.

- The substrates were again washed with pure boiling DI water in order to remove contaminations remain from H_2O_2 stage.

After completing all the cleaning steps, the clean soda-lime glass substrates were kept in pure methanol.

Prior to the film deposition process, the back side of n-type Si (n-Si) substrates were coated with silver (Ag) in order to make a back ohmic contact by using thermal evaporation technique. The front surface of n-Si wafers was cleaned with 10% of hydrogen fluoride (HF) and 90% of DI water solution and then washed with pure DI water sequentially blown dry in N_2 in order to eliminate the native oxide layer on the surface before placing them into the holder of evaporator chamber for the deposition process.

5.2.2 Cleaning the ITO Slide

The indium tin oxide (ITO) coated glass substrates (10 ± 5 Ω/□) were purchased from Thin Film Devices Inc. Commercially purchased ITO glasses were used as substrate to produce inverted polymer solar cell devices. The substrate cleaning procedure is a very important step to eliminate contamination effects on solar cells. All glassware, used for cleaning procedure, should be perfectly clean. Before starting cleaning procedure, all glassware were washed with detergent and rinsed with deionized water (DI water). Then, glassware was ready to use in the cleaning procedure of ITO substrates. The main steps of cleaning process of ITO substrates can be summarized as follow;

- ITO substrates in the beaker full with powdered detergent and DI water were cleaned ultrasonically for 10 minutes.

- ITO pieces were manually scrubbed by gloved hand and detergent and rinsed with DI water. Then, they again placed inside in the solution of detergent and sonicated for 20 minutes.

- ITO substrates were rinsed and placed in a new beaker with solution sodium hydroxide (NaOH) (15 gr NaOH in 150 ml DI water) and sonicated for 20 minutes.

- Substrates were rinsed with DI water and transferred to new clean beaker and sonicated inside pure acetone for 20 minutes.

- ITO substrates were rinsed and placed in a beaker and sonicated in isopropyl alcohol (IPA) for 20 minutes.

The clean ITO substrates can be stored in IPA for up to four weeks. They were dried in the vacuum oven at 80 ^{o}C for 15 minutes before using.

5.2.3 Thermal Evaporation Method

The deposition of $CuIn_{1-x}Ga_xSe_2$ thin films was performed by using a thermal evaporator of Vaksis Midas Coating System which has the lowest pressure value around 10^{-7} *Torr* and PC with special program which allows the automatic control of the system during the deposition process. The picture and schematic representation of the evaporation system is given in Figure 5.1.

Source units are Radak furnaces and they consist of alumina and quartz crucibles wrapped with molybdenum and tantalum wires in which the source materials were heated, all of which were placed into the tantalum liners in order to stabilize the source temperature. The source was heated by controlling the current passing through the molybdenum or tungsten wires with the source power unit system. The source temperatures during the growth process were measured with two types of thermocouples (type-K and type-R) and they were placed within the alumina and quartz ampoules and holder, and controlled by temperature controller. The type-K thermocouples are made from Platinum Rhodium-13%/Platinum and can be used from low temperature to very high temperatures (-50 ^{o}C to 1480 ^{o}C). The type-K thermocouples are made from Nickel-Chromium/Nickel-Alumel and working range changes in between -270 ^{o}C to 1260 ^{o}C.

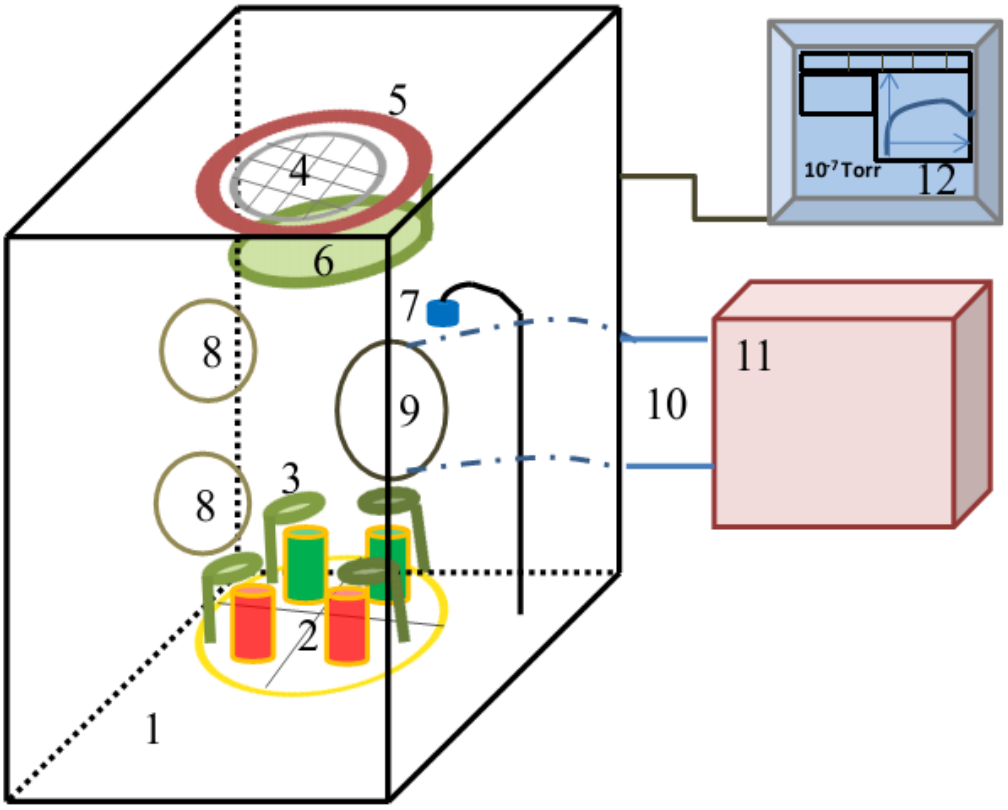

Figure 5.1 Schematic representation of Vaksis Midas Coating System used for the deposition of CIGS thin films: 1. Steel chamber, 2. source boats, 3. shutters of sources, 4. substrate holder, 5. substrate heater, 6. shutter of holder, 7. thickness monitor probe, 8. windows, 9. air outlet, 10. exhaust pipe, 11. mechanical and turbo-molecular pumps, and 12. computer.

CIGS thin films were deposited using Cu, InSe, GaSe, and Se sources through the thermal evaporation. The layer thickness optimization of Cu, InSe, GaSe, and Se thin films were carried out by conducting several deposition cycles. The deposition process was started when chamber pressure reached around 10^{-7} Torr. The same optimized deposition parameters were used during the sequential deposition of Se (50nm)/ InSe (40nm)/ GaSe (30nm) / Cu (20nm) / Se (100nm) / GaSe (50nm)/ InSe (60nm) / Cu (20nm) / Se (75nm) / InSe (50nm) / GaSe (50nm) / Se (100nm) thin film layers onto the soda-lime glass, ITO and n-Si substrates to form CIGS thin film as square and van der Pauw geometries as illustrated in Figure 5.2. During the

deposition, temperature of substrates was kept at a temperature around 300 ^{o}C and thickness of individual layers was monitored in-situ by SYCON model thickness monitor. The total thickness of thin films was measured by Dektak profilometer which vary from 700 nm to 730 nm depending on position of samples on substrate holder.

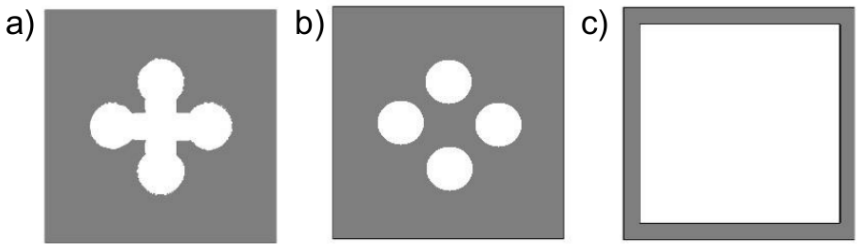

Figure 5.2 Shadow copper mask shapes for (a) thin film production of van der Pauw geometry, (b) metal contact production for thin films grown in van der Pauw geometry, and c) thin film production with 2 cm x 2 cm square geometry.

5.2.4 Post annealing process

In order to change the physical and chemical properties of deposited thin films, after deposition, subsequent post-annealing process was applied under the nitrogen atmosphere. In this process, the deposited CIGS thin films were inserted in an isolated furnace and heated gradually until the desired temperature was reached at which the temperature was kept constant for certain time, then the system was allowed to cool down to room temperature slowly.

The deposited CIGS thin films were subjected to post annealing process under the nitrogen (N_2) atmosphere at different fixed temperatures values between 300 to 450 ^{o}C for a limited time interval of 30 minutes.

5.3 Deposition of PbS Quantum Dots Thin Film

In this study, lead sulfide (PbS) quantum dots (QDs) solution was maintained from Evident Technologies with lot number Lot# 700 nm – PbS 07007-E1. The PbS QDs

solution was dispersed with toluene solvent with 1:1 ratios and diluted solution was used to deposit the QDs layer on top of the CIGS thin film by using spin coating method to provide CIGS/QDs structure. The same amount of solution and spin coating parameters used for the deposition were; 30 µL solution, 30 seconds and 2500 RPM respectively. Then two different processes were applied to solve organic legends. Initially, the QDs coated samples were kept inside pure methanol for 5 minutes, afterwards the samples were placed on the hot plate and annealed at 110 °C for 1 hour.

5.4 Structural Characterization

5.4.1 X-ray Diffraction (XRD)

X-ray diffraction (XRD) technique is one of the main instruments for the structural characterization of materials. It has been developed for the determination of orientation and phases of crystals. It can also give average grain sizes by means of the Scherrer Formula [126]. Each crystalline material has unique X-ray pattern. Therefore, it can be used as a differentiating property of material. Once the XRD diffractograms obtained, the data are compared with the International Centre for Diffraction Data (ICDD) database which records the XRD pattern of well known materials in order to match the measured data to get information about material.

In this study, a Rigaku Miniflex XRD system equipped with CuKα X-ray source (λ=1.504 Å) was used to obtain the structural properties of deposited CIGS thin film samples. All XRD patterns were recorded in between 10 and 80^{o} with a scan speed of 2^{o}/minute.

5.4.2 Raman Spectroscopy

Raman spectroscopy is a powerful, fast and non-destructive technique and it is used to provide information about vibrational, rotational, and other low-frequency modes in a sample [127], [128]. Raman effect is a physical phenomenon that results from the interaction of vibrational and/or rotational motions of molecules of structure with the electromagnetic radiation [129]. Raman spectroscopy depends on a frequency

change of incident photons after inelastic interaction with matter. In this technique, local atomic bonding structure is examined by inelastic interaction of incident photons with transverse and/or longitudinal modes of phonon. Raman spectroscopy gives the spectral characteristic of phonon vibration in solid materials, so that it can be used to provide the fingerprint of molecules which gives an opportunity for sample identification and phase qualification.

In this work, Raman measurements of CIGS thin film and CIGS/QDs samples were carried out by Horiba-Jobin Yvon i550 Raman system with Peltier cooled charge-coupled device (CCD) camera with $1cm^{-1}$ resolution in The Center for Solar Energy Research and Applications (GÜNAM) at METU. A 532 nm green laser (Nd:YAG) as a monochromatic light excitation source was used at room temperature.

5.4.3 Scanning Electron Microscopy (SEM)

A scanning electron microscope (SEM) is a tool that uses a focused high-energy electron beams to interact with atoms in the materials. Electron-atom interactions generate a variety of signals at the surface of material that can be collected and imaged by a high resolution charge-coupled device (CCD) camera at high vacuum condition. The macro-images, detected by CCD, contain information about the surface topology and morphology of materials.

In this study, SEM micro-images were provided by using a FEI Quanta 400 FEG model Scanning Electron Microscopy System in Central Laboratory of Middle East Technical University (METU).

5.4.4 Energy Dispersive X-ray Analysis (EDXA)

Energy Dispersive X-ray Analysis (EDXA) is an instrument used to decide the chemical composition of materials and elemental distribution of elements trough the materials. This technique is mostly used as an accessory that attached to SEM system. EDXA is also known as energy dispersive spectroscopy (EDS).

Compositional analyses of deposited CIGS thin films were investigated by using a FEI Quanta 400 FEG model SEM with EDXA system in Central Laboratory of METU.

5.5 Optical Characterization

The optical transmission spectrum is commonly used to obtain the optical properties of the materials. These measurements give information about band structure, absorption coefficient, and trap or impurity levels of semiconductor materials. A spectrometer basically consists of monochromator as a light source and detectors to measure transmitted light.

In this study, optical properties of CIGS thin film samples were carried out with Perkin-Elmer Lambda 950 UV/Vis/NIR spectrophotometer in the wavelength range of 350–1100 nm in GÜNAM at METU. Following the transmission measurements, the transmission data were corrected according to the background absorption of soda-lime glass substrate on which the thin film samples were deposited. Then, the optical band gaps (E_g) and absorption coefficient (α) of deposited CIGS thin film samples were calculated.

5.6 Electrical Measurements

Electrical properties of CIGS thin film and CIGS+PbS QDs samples were investigated by using the temperature dependent photoconductivity, Hall effect, current-voltage (I-V), and capacitance-voltage (C-V) measurements.

5.6.1 Temperature Dependent Photoconductivity

CIGS thin films and CIGS+QDs samples which were grown in van der Pauw geometry (see Figure 5.3 (a)) were used to measure the temperature dependent conductivity of samples. Samples were coated with indium (In) contacts by using thermal evaporation technique and copper shadow masks which were given in Figure 5.2 (b). Heat treatment was applied to metallic contacts following to the deposition at

100^{o} C for 30 minutes to obtain good ohmicity. Ohmic behavior of metal contacts is crucial for the reliability of electrical measurements. So that, the ohmicity of the metal contacts was checked by performing the linear variations of the current-voltage characteristics after coating In as a metal contact.

The temperature dependent photoconductivity of deposited CIGS thin films and QDs coated CIGS samples was studied in the temperature range of 100-350 K by means of a Janis Liquid Nitrogen VPF Series Cryostat. The Univac Rotary pump was used to create a vacuum inside the cryostat. The temperature of the samples was controlled by a LakeShore-331 temperature controller and measured with a GaAlAs diode sensor inside the cryostat. The temperature of sample was gradually increased from 100 K to 350 K by 10 K steps. The vacuum of cryostat was provided by the Univac Rotary pump. The samples were illuminated by 12-Watt halogen lamp that is located at a desirable place above the sample in order to provide certain illumination of the whole surface uniformly. The illumination intensities of the halogen lamp were arranged at five distinct light intensities of about 20, 35, 55, 80 and 115 mW/cm^2 by changing the current from 50 mA to 90 mA with 10 mA steps by means of a Keithley 220 programmable current source. Moreover, the value of illumination intensities of halogen lamp was determined by an IL Ford 1700 radiometer. Applied bias voltages and measured current were carried out by the same Keithley 2401 Multimeter and all devices in experiment were controlled by using LabVIEW computer software program.

5.6.2 Hall Effect Measurement

The Hall Effect experiment provides information on the resistivity, the carrier type, the carrier concentration, Hall coefficient, and the mobility of the carriers at a given temperature. It was discovered by E.H. Hall in 1879 during an investigation on the force acting on a current carrying conductor in a magnetic field before electron was not experimentally discovered [130].

When a material is placed inside a magnetic field which is perpendicular to the direction of current flow, the carriers will be deflected due to the Lorentz force and an electric field is built up and resulting from the accumulated carriers at the surface

of the semiconductor as shown in Figure 5.3. The electric field created by the deflected carriers is called the Hall field and the direction of this field depends on the type of carriers (n-type or p-type). The carrier density and type (n-type or p-type) of semiconductor materials can be determined from direct measurement of Hall voltage.

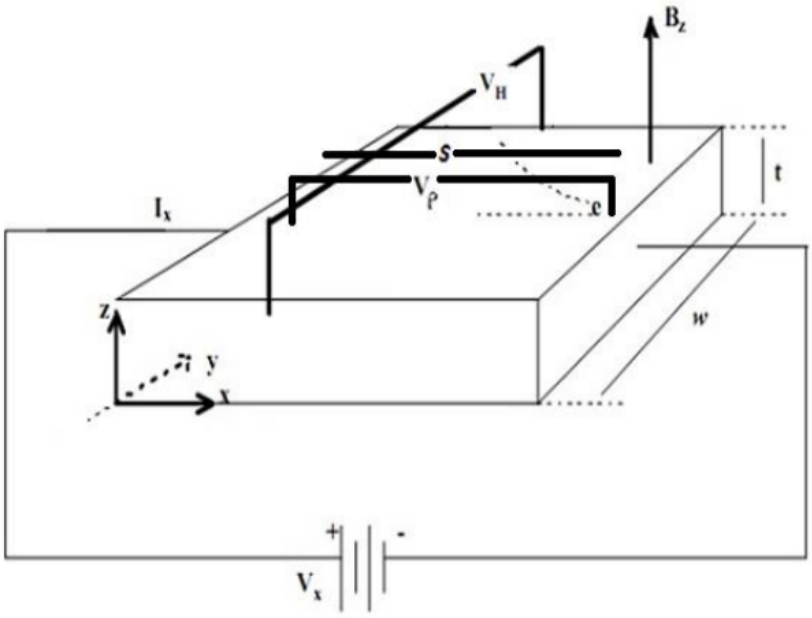

Figure 5.3 Schematic illustration of Hall effect [131].

In this work, the Hall Effect experiment was carried out at room temperature condition by using automatically controlled Hall Effect set-up and the magnetic field produced by Walker Magnion Model FFD-4D electromagnet which was controlled by a personal computer with special software program in GÜNAM at METU. CIGS and CIGS+QDs thin film samples were prepared as van der Pauw geometry and they were coated with In contacts as illustrated in Figure 5.2.

5.6.3 Current-Voltage Measurement

Ag/n-Si/p-CIGS/In and Ag/n-Si/p-CIGS/QDs/In hetero-structures were fabricated by using thermal evaporation and spin coater. After deposition of the CIGS thin films, annealing process was applied to the samples. Annealed samples were coated with

QDs by using spin coating technique as described in section 5.3. The front dot contacts were grown by metallic thermal evaporation technique and annealed at 100 ^{o}C for 30 minutes to provide good ohmicity. The dot contact area of In metal contact was 7.85x10^{-3} cm^{2}.

In order to figure out the rectifying behaviors of the devices, dark and illuminated current-voltage (I-V) characteristic were performed at room temperature and in the temperature range of 220-360 K. A Bias voltage in between -2 V and 2V by 0.02 V-increment was applied to the front and back contact of the devices and current drop was measured with Keithley 2401 source meter which was controlled by a Labview PC program. Dark I-V measurements were executed in a shielded dark four probe-box to avoid illumination effects and external field on the devices. In illuminated case, same experimental set up was used and the devices were illuminated by using 12-Watt halogen lamp. The illumination intensity of the halogen lamp was arranged to 80 mW/cm^{2} by applying the current 80 mA by means of a Keithley 220 programmable current source.

In order to obtain the temperature dependencies of I-V measurements, devices were placed into a cryostat and the low temperatures were provided by The Model 22 CTI Cryogenics closed-cycle helium refrigeration system and the temperature was controlled by LakeShore DRC-91C temperature controller. Temperature dependence of I-V of the devices was measured in between 220 K and 360 K with 20 K increments. These measurements were carried out with the computer-controlled measurement setup in GÜNAM at METU.

5.6.4 Capacitance-Voltage Measurements

The frequency dependent capacitance-voltage (C-V) measurements were carried out to analyze the junction region structure of Ag/n-Si/p-CIGS/In and Ag/n-Si/p-CIGS/QDs/In devices. The C-V characteristic of devices gives information about barrier height and impurity concentration of the materials. The C-V measurements with conductance-voltage (G-V) measurements at high frequencies and high forward bias region give the series resistance (R_S) of the devices.

The C-V and G-V measurements were carried out by using a HP 4192A LF Impedance Analyzer which was controlled by a personal computer using LabVIEW software program. The analyzer device uses a linear voltage ramp in the bias range to sweep the voltage from accumulation to inversion or vice versa at a defined bias ramp rate. A small AC voltage is unified on the ramp voltage to measure the differential capacitance change in the depletion region. The built- in frequency synthesizer can be adjust to measuring frequency in between 5 Hz to 13 MHz with maximum resolution of 1 MHz. Oscillation level of the AC voltage can be changed from 5 mV to 1.1 Vrms and it can be increased with 1 mV steps. The internal DC bias voltage source can supply ±35 V with 10 mV steps [132].

The C-V and G-V measurements of Ag/n-Si/p-CIGS/In and Ag/n-Si/p-CIGS/QDs/In heterojunction devices were performed within the frequency range of 1 kHz - 10 MHz. The amplitude of the DC bias voltage ramp was changed from -2 V to 2 V with 0.2 V increments and the oscillation level of the AC voltage was set to 0.05 V for dark and illuminated measurements at room temperature condition. The illumination of the devices was provided by 12-Watt halogen lamp and it was arranged to 80 mW/cm^2 by applying the current 80 mA by means of a Keithley 220 programmable current source.

5.7 Organic Solar Cell

5.7.1 Preparation of ZnO Precursor

The sol-gel method was used for deposition of ZnO layer and commercially purchased zinc acetate dihydrate ($Zn(CH_3COO)_2 \cdot 2H_2O$, Sigma-Aldrich, 99.999% trace metals basis, 25 g), ethanolamine ($NH_2CH_2CH_2OH$, Sigma-Aldrich, ≥99.5%, purified by redistillation), and 2-methoxyethanol ($CH_3OCH_2CH_2OH$, Sigma-Aldrich, 99.8%, anhydrous) were used to prepare the ZnO precursor.

The ZnO precursor was prepared by dissolving 0.2 gram of zinc acetate dihyrate in 56 µl of ethanolamine and 2 ml of 2-methoxyethanol under vigorous stirring for minimum 8 h at room temperature in closed bottle to avoid the reaction with air.

5.7.2 Deposition of ZnO layer

The ZnO precursor was spin coated on top of the clean ITO substrates by using 40 seconds and 4000 RPM of spin coater parameters as a cathode buffer layer (CBL). Then, they were annealed with hot plate or oven at 200 ^oC for 1 hour. The thickness of ZnO layer was in the range of 30 nm and 40 nm, as determined by profilometer. Then, the ZnO coated substrates were transferred to glovebox. The glovebox is a sealed container that is created to provide a separate desired atmosphere and manipulate materials.

In this study, the MBRAUN UNIlab Plus glovebox workstation in Device Research Laboratory (DRL) in the Electrical Engineering Department at University of California, Los Angeles (UCLA) was used to product the polymer solar cell devices. The glovebox has box pressure control w/ foot switch in the range of -15 mbar and +15 mbar with attainable purity level $H_2O < 1$ ppm and $O_2 < 1$ ppm. The atmosphere and purity level of glovebox are controled automatically. The picture of glovebox is given in Figure 5.4.

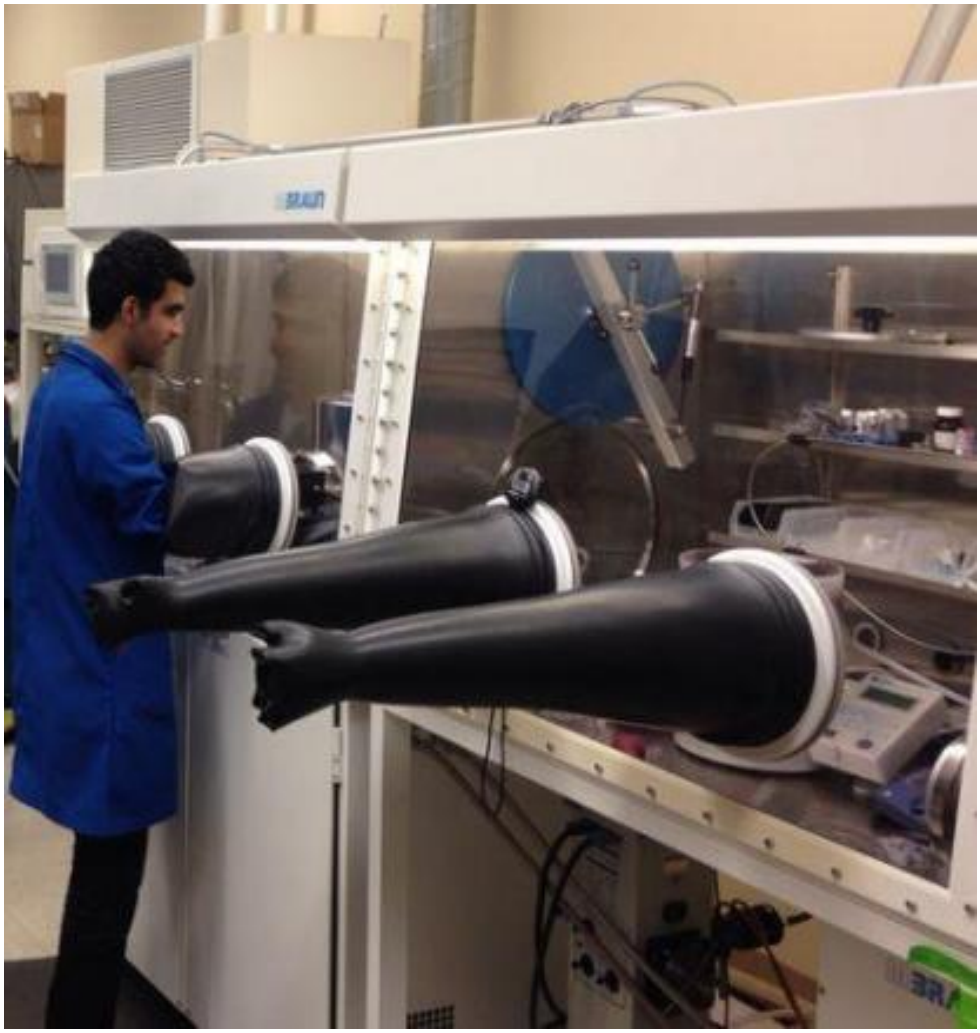

Figure 5.4 Picture of the glovebox used for the production of IPCS.

5.7.3 Polymer Active Layer

A solution of mixture poly(3-hexylthiophene) (P3HT) and phenyl-C61-butyric acid methyl ester (PCBM) was dispersed in a mixed solvent of dichlorobenzene at the concentration of 20 mg/ml with magnetic stirrer inside an isolated glovebox. The mixture of P3HT:PCBM solution was kept at a constant temperature of 80 ^{o}C for 14 hours.

The P3HT:PCBM solution was then spin coated on top of the ZnO coated ITO/glass substrate with 600 RPM for 20 seconds and 1100 RPM for 9 seconds inside glovebox. The samples were kept inside glovebox until they dry. And then, they were annealed at 150 ^{o}C for 5 min by using a hot plate in the glovebox.

5.7.4 Deposition of MoO_3 and Ag Electrode

The thermal deposition of the 10 nm molybdenum trioxide (MoO_3) was conducted on top of the polymer coated ZnO/ITO/glass substrates as an anode buffer layer (ABL). 100 nm of the silver (Ag) top electrode was thermally coated from elemental source on top of the MoO_3 coated substrates inside the same evaporator chamber and the thickness of layers was monitored by INFICON SQC-310C deposition controller. The picture of fabricated IPSC was given in Figure 5.5.

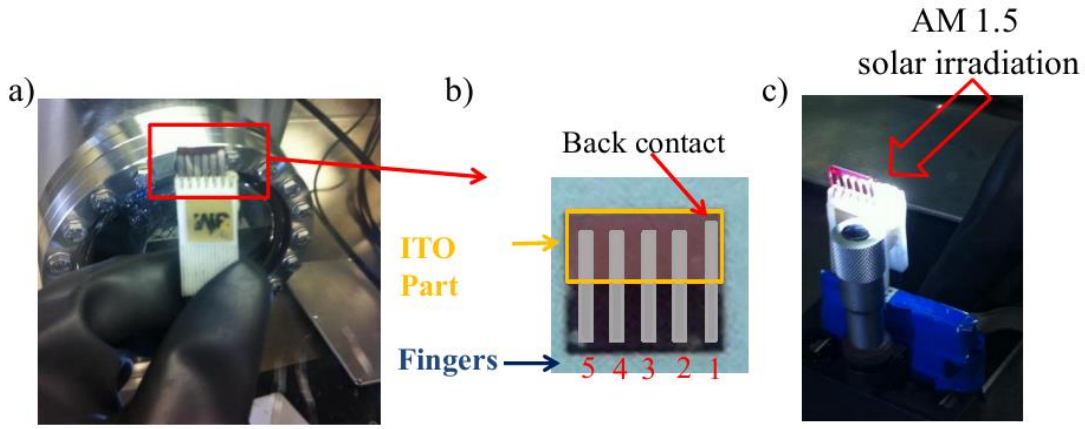

Figure 5.5 Picture of a) fabricated IPCS, b) details of fabricated IPSC, and c) ICPS under the 1.5 AM solar irradiation inside glovebox.

5.7.5 Deposition of Quantum Dots in IPSC

In this study, commercially purchased lead sulfide quantum dots (PbS QDs) (Evident Technologies with lot number Lot# 700 nm – PbS 07007-E1) was dispersed with toluene solvent with 1:1 ratios and diluted solution was used to deposit the QDs layer on top of the ZnO film by using spin coating method. Five different sample groups were prepared with different spin coating times to study the effect of the QDs amount on the device efficiency. For each group of prepared samples the amount of solution and the spin coating parameters used were the same as; 30 µL solution, for 30

seconds and at 2500 RPM. Then two different processes were applied to solve organic legends. Initially, the QDs coated samples were kept inside pure methanol for 5 minutes. After that, the samples were placed inside vacuum oven and annealed at 110 °C for 1 hour under the pressure lower than 10^{-3} mbar. Then samples were transferred to glove box.

5.7.6 Characterization of Polymer and Quantum Dots

5.7.6.1 TEM Sample Preparation and Measurement

10 µl of P3HT:PCBM polymer solution and PbS QDs were diluted in 100ml Isopropyl alcohol (IPA) solvent, separately. Firstly, the diluted polymer solution was used to coat polymer layer on top of the copper grid of TEM substrate. Then, it was kept at room temperature conditions over night to dry the polymer layer well. Secondly, the diluted QDs solution was used to coat the QDs particles on the dried polymer layer. Finally, the sample was again kept in room condition over night to dry the QDs layer.

TEM images were obtained by using FEI Tecnai G^2 Spirit BioTwin CTEM device in Central Laboratory of METU.

5.7.6.2 Optical and Structural Characterizations

In order to identify the optical and structural properties of P3HT:PCBM polymer, QDs and polymer + QDs layers, optic and structural characterizations measurements were performed.

Transmittance and absorbance spectra for layers of polymer, QDs and polymer+QDs were separately obtained and the results were compared to understand the effects of QDs on polymer layer. The measurements were performed by using UV-VIS spectroscopy system (Ocean Optics, USB2000+UV-Vis).

The photo luminance (PL) emission spectra of QDs solution (in toluene) and QDs thin film which was coated on glass substrates were measured using the 488 nm

excited wavelength with an argon ion laser and emission peaks were recorded by CCD detector and special PC program.

The effects of QDs on polymer layer were also investigated by using Raman methods at room temperature. Polymer, QDs and polymer+QDs thin film samples were prepared and the confocal Raman measurements were carried out by Jobin Yvon Horiba i550 confocal Raman with a Nd:YAG laser (532 nm) excitation source in GÜNAM at METU. Double monochromator and Peltier cooled CCD detector with 1 cm^{-1} resolution were used to designate Raman shifts. The affected peak areas of all samples were compared and analyzed by means of Raman area peak analyses.

5.7.7 Solar Cell Measurements

Current density-voltage (J-V) characteristics of the investigated IPSC for forward and reverse DC bias voltages ranging from -1.5 V to +1.5 V at room temperature for dark and under 1.5AM global light with different amount of QDs and without QDs layer were measured using Oriel Xenon lamp and optical filters in DRL at UCLA.

Air mass (AM) is the optical route length through Earth's atmosphere for radiation from the sun and shown in Figure 5.6. The intensity and spectral distribution per of incident light is effected by the ozone (O_3), Oxygen gas (O_2), water (H_2O), and carbon dioxide (CO_2) molecules in the Earth's atmosphere [133]. AM0 represents to the solar spectrum in outer space, and AM1.5 was defined as the reference spectrum for Standard Test Conditions [134].

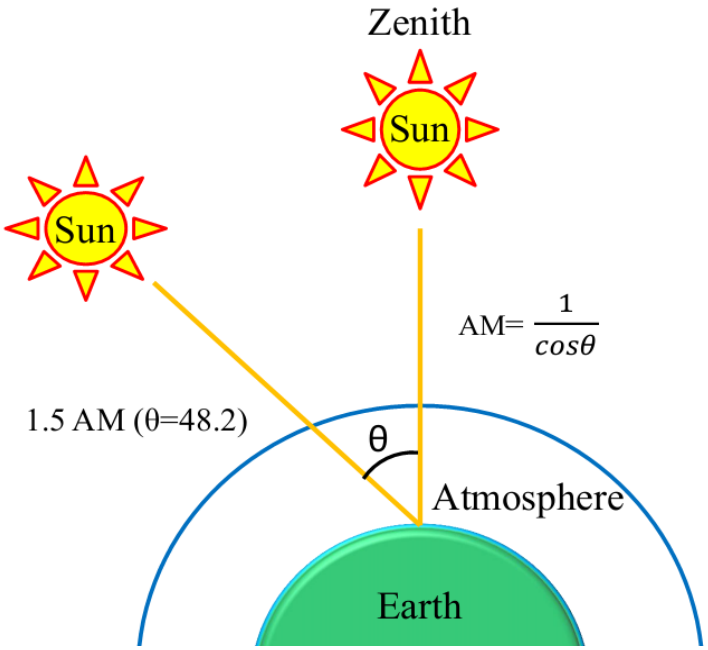

Figure 5.6 The path length of solar irradiation (Air Mass).

Current density-voltage (J-V) measurements of devices under solar simulated illumination were performed using a Keithley 2400 source meter and air mass (AM) 1.5 solar irradiation was generated by using Oriel Xenon lamp and optical filters.

For further understanding of the effect of QDs layer inside the device structures, capacitance-voltage (C-V) and electrochemical impedance spectroscopy measurements were performed. All devices can be treated as a parallel plate capacitor during the measurements performed at room temperature and in dark [135]. C-V measurements and electrochemical impedance measurements were conducted with Agilent 4294A Precision Impedance Analyzer in DRL at UCLA. The C-V measurements were done at 1 kHz frequency as a function of the bias between -1 V and +1 V and constant oscillating amplitude of 50 mV for devices with and without QDs layer. The experimental electrochemical impedance in the complex plane for forward bias voltage 0.58 V and different oscillating frequency in between 40 Hz to 1 MHz was carried out for some devices which were used in C-V measurements.

CHAPTER 6

RESULTS AND DISCUSSIONS

6.1 Inorganic Thin Film Based Devices

6.1.1 Introduction

This section covers the results of structural, optical and electrical measurements obtained for the CIGS thin film samples deposited by thermal evaporation method. Section is divided into two parts. First part deals with structural, optical, and electrical characterizations of thermally CIGS thin films deposited on soda-lime glass substrates. In the second part of this section, the effect of QDs layer inside p-n heterojunction devices (p-CIGS/n-Si) are introduced in detail.

In order to examine the effects of quantum dots (QDs) inside inorganic solar cells, PbS QDs layer was inserted in to the p-n heterojunction device of p-CIGS and n-Si. The QDs layer was coated on top of the CIGS thin film by using spin coating method. Figure 6.1 shows the schematic illustration of band position p-n heterojunction solar cell junction device which was used in this study. The results of experimental studies on the complete Ag/n-Si/p-CIGS/In and Ag/n-Si/p-CIGS/PbS QDs/In solar cell structures without and with QDs layer and all the thin film layers in the structure are presented in this chapter.

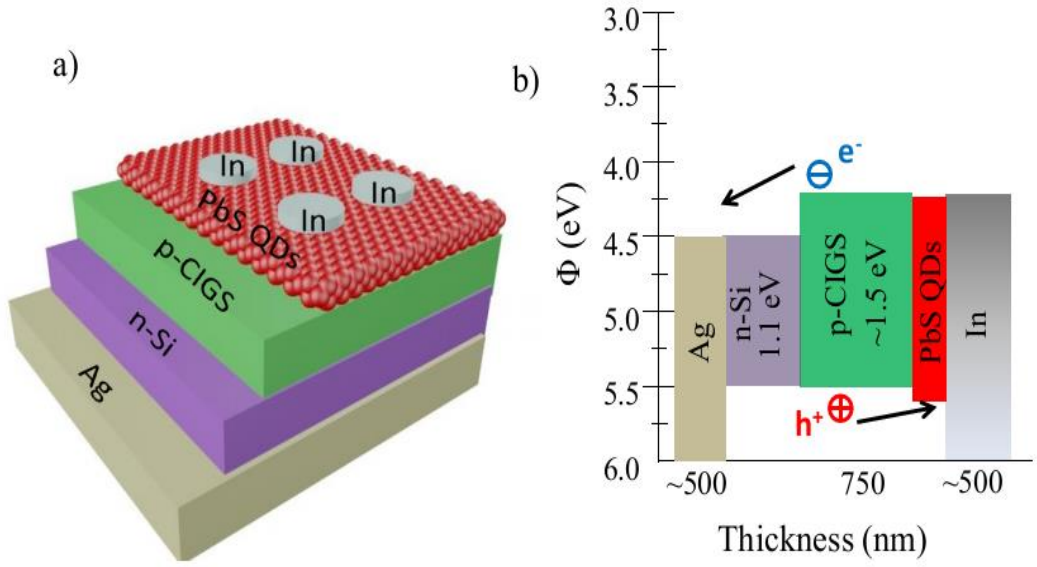

Figure 6.1 Schematic diagrams of PbS QDs incorporated a) the p-n junction device with QDs thin film layer containing Ag/n-Si/p-CIGS/PbS QDs/In layers, and b) band position of n-Si/CIGS p-n junction device with QDs layer.

6.1.2 Structural, Compositional and Surface Analysis of CIGS Films

In order to obtain the structural and compositional properties, and surface morphology of deposited thin films layers, $CuIn_{1-x}Ga_xSe_2$ (CIGS) thin film samples were thermally deposited onto soda lime glass substrates by using Cu, InSe, GaSe, and Se sources. The temperature of substrates was kept at 300 ^oC during the deposition process. CIGS thin films were annealed at 350, 400 and 450 ^oC temperatures following to the growth under nitrogen atmosphere for 30 minutes. The XRD and Raman spectroscopy measurements were performed for the analyses of the quality of deposited samples. The XRD pattern and Raman shift of as grown and the annealed CIGS samples were illustrated in Figure 6.2 and Figure 6.3, respectively.

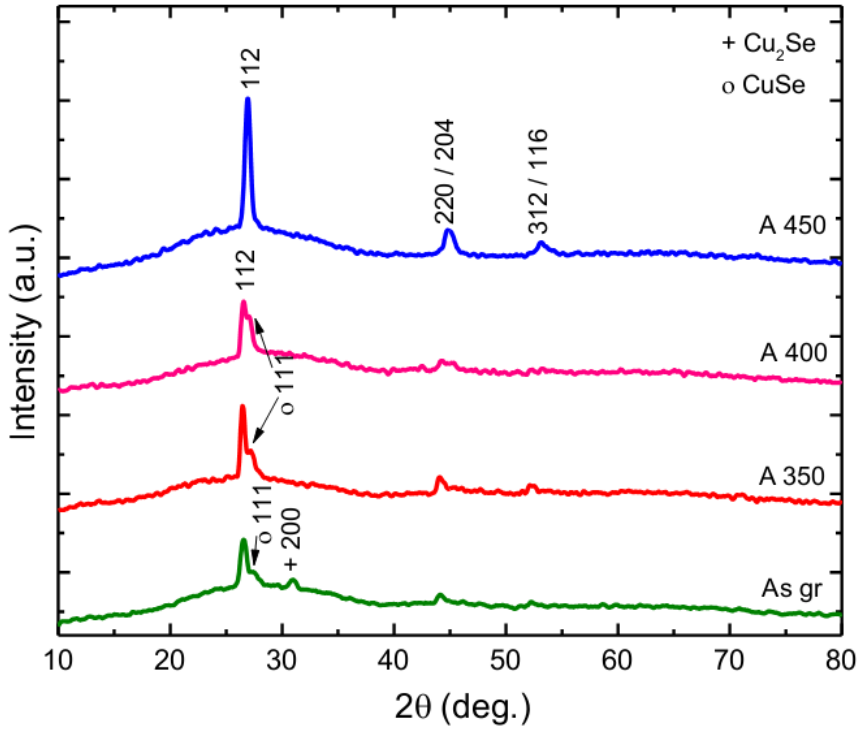

Figure 6.2 XRD patterns of the thermally evaporated of the thermally evaporated as-grown and annealed CIGS thin film samples at 350, 400 and 450 ^{o}C for 30 minutes.

As observed in Fig.6.2, the main diffraction observed at 2θ ~ 26.9^{o} was identified as to belong to the CIGS chalcopyrite structure with the (112) preferred orientation, while the secondary peaks observed at 2θ ~ 44.8^{o} and 2θ ~ 53.1^{o} with (220) / (204) and (312) / (116) orientations, respectively. Phase existing in the samples were identified as to belong to CIGS having tetragonal structure like the zinc blende with the lattice constants of lattice a: 5.7, b: 5.7 and c: 11.3 Å [136]. This is a good confirmation of that the CIGS has chalcopyrite structure with the preferred orientation direction along the (112) plane.

The intensity of (112) peak increased with increasing annealing temperature from 350 to 450 ^{o}C. On the other hand, the binary phases of CuSe with orientation of (111) at 2θ ~ 27.4^{o} and Cu_2Se with orientation of (200) at 2θ ~ 30.9^{o} were observed for the as grown and annealed samples at 350 and 400 ^{o}C. The sphalerite structures of CuSe and Cu_2Se were exist due to the low substrate temperature at 300 ^{o}C [137]. The sphalerite structures completely disappeared and the structure turned to chalcopyrite

structure after samples annealed at 450 ^{o}C. The reasons for the transformation to chalcopyrite structure at this temperature may be due to deposition of the films at low substrate temperature, since the impinging of atoms place at fixed positions due to the insufficient thermal energy for the migration and nucleation processes during deposition.

The grain size D was evaluated from the full width half maximum (FWHM) value of main XRD peak using the the Scherrer's formula [138]. The calculated *D* values depending on annealing temperatures were found to be in between 161 and 207 nm for CIGS samples which increase with increasing annealing temperature. It means that the increase in grain size is the indication of improvement in the crystallinity with the annealing process as observed in XRD patterns of CIGS samples.

The XRD pattern shows only an overall picture of the phases contained in the CIGS thin film samples. Therefore, the further information about structure of CIGS thin films was studied by the Raman spectroscopy.

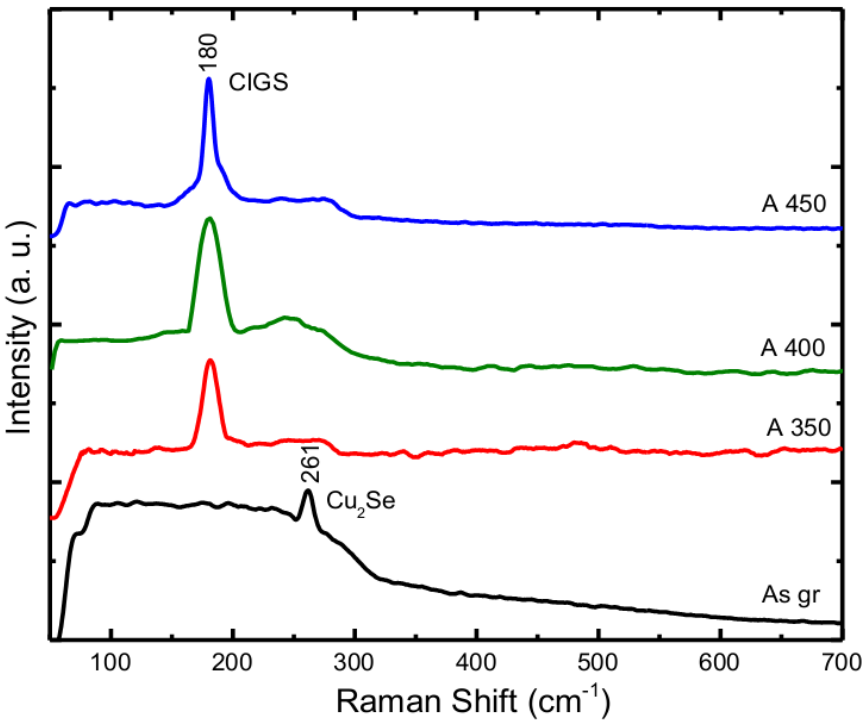

Figure 6.3 Raman spectra of the thermally evaporated as-grown and annealed CIGS thin film samples at 350, 400 and 450 ^{o}C for 30 minutes.

$CuIn_{1-x}Ga_xSe_2$ crystallizes in the chalcopyrite structure belonging to the space group $I\bar{4}2d$, i.e. to the point group D_{2d}^{12} [139], [140]. In the general vibration for group D_{2d}, the primitive cell's vibrations including acoustic and optical modes are separated as Γ_σ: $A_1 + 2A_2 + 3B_1 + 4B_2 + 7E$. The symmetry of the acoustic modes is $B_2 + E$ and there are 19 Raman active modes ($A_1 + 2A_2 + 3B_1 + 3B_2 + 6E$) [141]. The tetragonal ternary (I-III-VI_2) compound can be visualized as two interpenetrating face centered cubic (fcc) lattice, the first anion lattice consist of group VI atoms and the other being an ordered array group I and III cations. As a result, super lattice structure reduces the sphalerite (cubic zinc blende) symmetry to that of a tetragonal chalcopyrite structure (A$_I$ B^{III} C^{IV}) [142]. There are generally two structural differences between the sphalerite and chalcopyrite structure. These are; a) tetragonal distortion where c/a is not equal to 2.0. b) Displacement of the group VI atom from its ideal value of u=25, where u is the tetrahedral distortion [139].

In this study to determine the Raman active modes in the film, Raman spectra of CIGS thin films were measured at room temperature. As clearly seen from Figure 6.3, the most intensive line at 180 cm^{-1} could be assigned to the A_1 mode which is the strongest mode observed in the Raman spectra of chalcopyrite structure [139]. On the other hand, as-grown sample had the most intensive line at 261 cm^{-1} which is the mode of E and this peak indicated the existence of Cu_2Se compounds for as grown sample [143]. The peak at 261 cm^{-1} completely disappeared with annealing process. The annealed CIGS samples had only one dominant peak at 180 cm^{-1}. This peak is the strong line of A_1 mode that could be the result of segregation of Se atom in the structure [144]. It means that the annealing has the pronounced effect on the crystallinity and the content of the thin film samples. Raman results suited perfectly with XRD results as discussed in the structural analysis part.

In order to investigate the effect of the heat treatment on the surface morphology and chemical compositions, scanning electron microscopy (SEM) and the energy dispersive X-ray analysis (EDXA) measurements were carried out for as-grown and annealed CIGS thin films at 350 ^oC and 450 ^oC under the nitrogen atmosphere for 30 minutes. The SEM images and EDXA results of CIGS thin films were given in Figure 6.4 and Table 6.1, respectively.

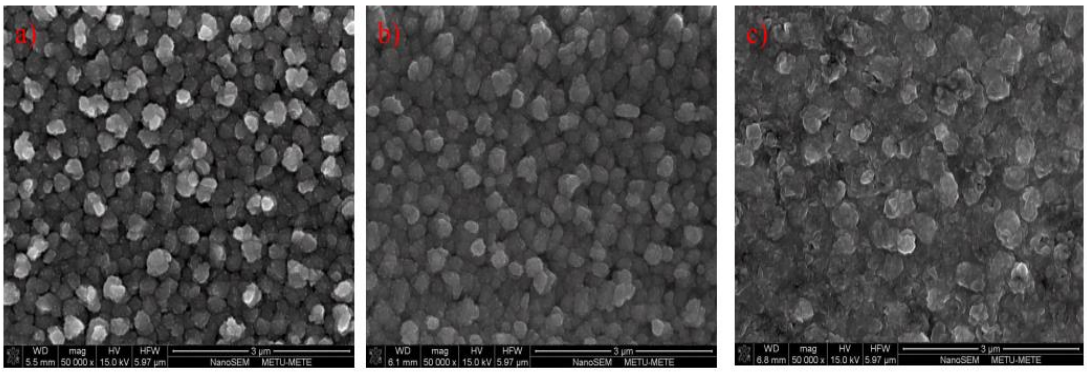

Figure 6.4 SEM micrographs of CIGS thin films for (a) as-grown, (b) annealed 350 ^{o}C, and (c) annealed at 450 ^{o}C for 30 minutes.

Table 6.1 The atomic ratio of as-grown and annealed CIGS thin films at different temperatures for 30 minutes under the nitrogen atmosphere.

	Cu (%)	**In (%)**	**Ga (%)**	**Se (%)**
Asgr	19	16	15	50
A 350	23	14	15	48
A 450	21	16	15	48

The SEM images of CIGS thin films showed uniform formation of the films with slight increase in the grain size with annealing as given in Fig.6.4. As observed from Table 1, Cu, In and Ga atomic compositions of as-grown films were found as 19%; 16%, 15% and 50%, respectively. Cu atomic ratio increased due to the Se segregation or re-evaporation from the samples with the post annealing process. In and Ga ratios almost stayed the same with annealing. No other impurities were detected during these analyses.

In order to investigate the effect of the quantum dots (QDs) on the structure, the confocal Raman spectroscopy measurements of CIGS thin film, PbS QDs layer and

CIGS thin film with QDs layer samples were performed at room temperature with 532 nm excitation laser source and Raman shifts were shown in Figure 6.5.

As clearly seen from Figure 6.5 (a), the most intensive Raman peak of CIGS is at 180 cm^{-1} which was at the same position of the one in Figure 6.3. Moreover, the QDs layer had the most intense Raman peak at 78 cm^{-1} and the other Raman peaks of QDs layer are at 444, 557, and 776 cm^{-1}. When both layers were brought together, the effects of QDs on thin film were explicitly seen. The most intense peak of CIGS and QDs together was also at 180 cm^{-1}. However, assembling of both layers resulted new peaks emerging or activated and increasing in some existent peak intensities as shown in Figure 6.5 (a). The inactive or weak B_1 mode of CIGS thin film was activated by coating of QDs layer. The CIGS thin films normally have the mode of B_1 at the position of 78.6 cm^{-1} [139]. However, B_1 mode is very weak and we could not see that peak in our experimental results. We also analyze the Raman shift peak areas for specific effected region of 78 cm^{-1}. In Figure 6.5 (b), the peak area of 78 cm^{-2} is given as an example. The peak area analysis of Raman shift at 78 cm^{-1} showed that, this peak did not appeared for the CIGS thin film samples, but after the QDs layer is coated on the CIGS surface, i.e for the CIGS + QDs samples, it emerged and the area under the peaks from 25.8 to 54.2 cm^2 increased the values of which were plotted in Figure 6.5 (c) for comparison. On the other hand, no considerable effect of QDs layer on the most intense peak of CIGS thin film at 180 cm^{-1} was observed, due to the strong vibration of A_1 mode of CIGS layer and weak vibration of PbS QDs.

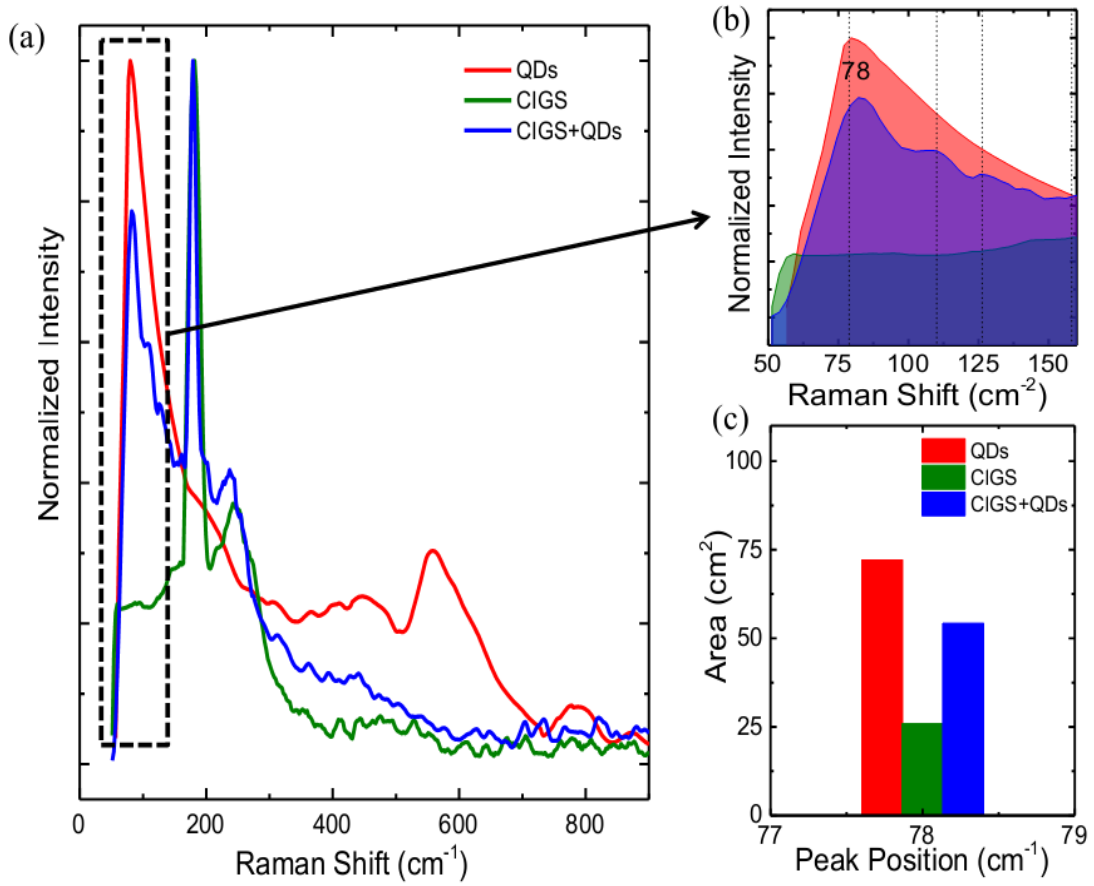

Figure 6.5 a) Normalized Raman spectra of CIGS thin film, PbS QDs thin film, and CIGS with PbS QDs layer b) Raman shift area at 78 cm^{-2} c) Comparison of Raman shift areas for QDs, CIGS and CIGS+QDs at 78 cm^{-1}.

6.1.3 Optical Characterization

Figure 6.6 shows the transmission spectra measured in the range of 400 - 1100 nm for the as-grown and CIGS thin film samples annealed at 350 and 550 ^{o}C for 30 minutes. As clearly seen from the figure, the transmission value of CIGS thin films increased with increasing annealing temperature. There was considerable change in transmission as the annealing temperature increases and transmission percent increased with increasing annealing temperature.

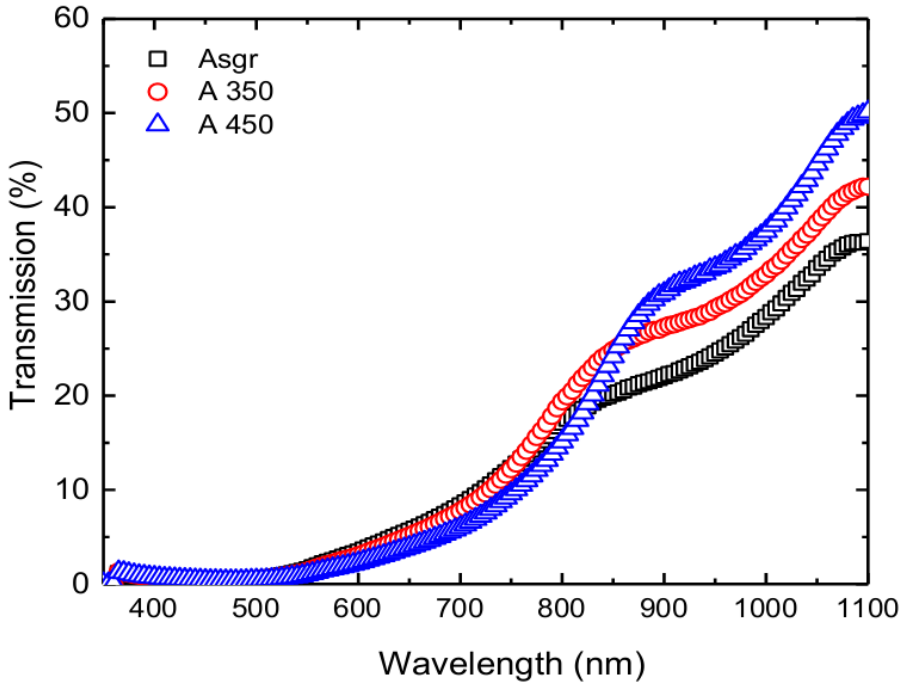

Figure 6.6 Transmission spectra for the as-grown, and CIGS thin films annealed at 350 and 450 ^{o}C for 30 minutes.

In order to determine the optical band gap of the thin film samples, absorption coefficient was calculated by using the relation;

$$\alpha = \frac{1}{d}\mathrm{Ln}\left(\frac{I_0}{I}\right) \tag{6.1}$$

where d is the thickness of the sample, I is the intensity of transmitted light, and I_0 is the incident light perpendicular to the surface of the sample. After calculating the absorption coefficient in the studied spectral region, Tauc plot [145] was used to calculate the optical band gap E_g values;

$$\alpha h\nu = A(h\nu - E)^n \tag{6.2}$$

where A is a constant and n is an power exponent, which changes according to the transition types, for direct transition, n = ½, and n = 2 for indirect transition [146]. It is possible to determine the type of transition, namely, direct or indirect by plotting $(\alpha h\nu)^{1/n}$ versus $h\nu$. In our case, $(\alpha h\nu)^2$ versus $h\nu$ were plotted to obtain the E_g values from extrapolation on the energy axis of linear regressions.

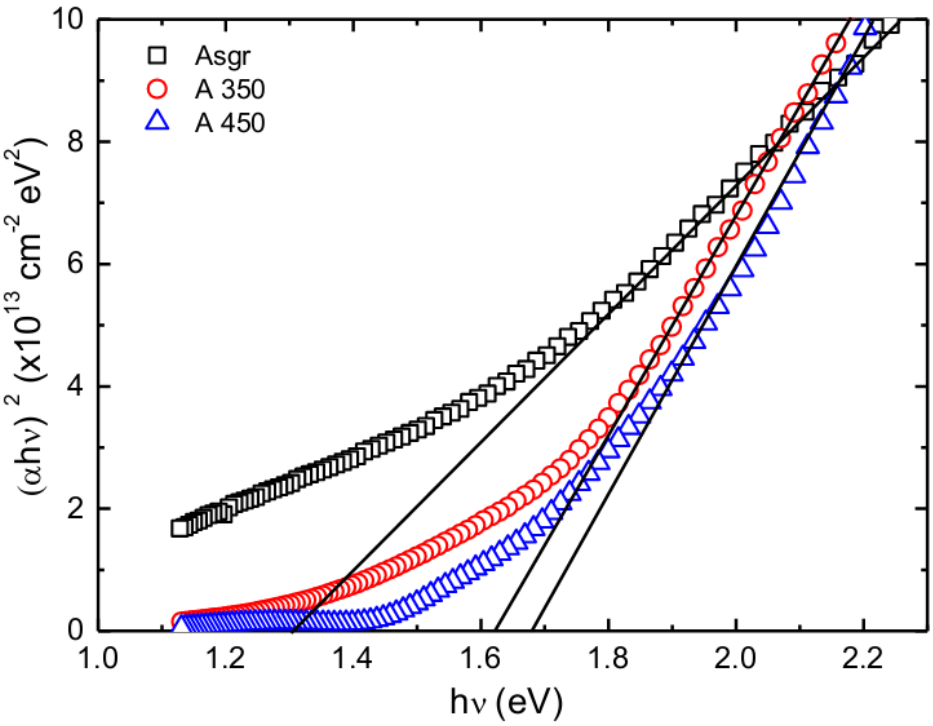

Figure 6.7 Plot of $(\alpha h\nu)^2$ against $(h\nu)$ for as-grown and CIGS thin films annealed at 350 ^{o}C and 450 ^{o}C for 30 minutes.

The Figure 6.7 represents the variation of the absorption coefficient as a function of incident photon energy $(h\nu)$ for the as-grown, and the CIGS thin films annealed at 350 and 450 ^{o}C. The absorption coefficient at room temperature was found to be in the range of 1.7x10^{3}- 5.6x10^{4} cm^{-1} for the incident photon energies of 1.1 – 2.3 eV. The general behavior of absorption coefficient as a function of photon energy in all plots is almost the same except the shifting of absorption edge slightly to infrared region with annealing. The band gap values were found to be 1.30 eV, 1.62 eV and 1.68 eV for as-grown and annealed CIGS thin film samples at 350 and 450 ^{o}C, respectively. In general, the decrease in disorder and defect density in the structure results in an increase in the optical band gap. The change in band gap values might be due to the existence CuSe and Cu_2Se phases observed in XRD patterns. A similar behavior was reported for InSe thin films by B. Thomas et al. [147] and C. Julien et al. [148].

6.1.4 Electrical Characterization

In this section, the results of the electrical and photoelectrical measurements performed on the CIGS thin film without and with QDs layer and Ag/n-Si/p-CIGS/In and Ag/n-Si/p-CIGS/PbS QDs/In are presented.

6.1.4.1 Photoconductivity Analysis

The photoconductivity measurements were carried out as a function of illumination intensity in the temperature range of 100-350 K. The measurements were performed at different light intensities (Φ), which were 20, 35, 55, 80, and 115 mW/cm^2, and the illumination was supplied by the halogen lamp. In order to analyze the effect of QDs on CIGS thin film and to determine the characteristics of the defects centers, the photocurrent (I_{ph}) versus illumination intensity (Φ) was plotted in Log-Log scale at constant temperatures of 150, 250, and 350 K for CIGS and without and with QDs layer as seen in Figure 6.8 and Figure 6.9.

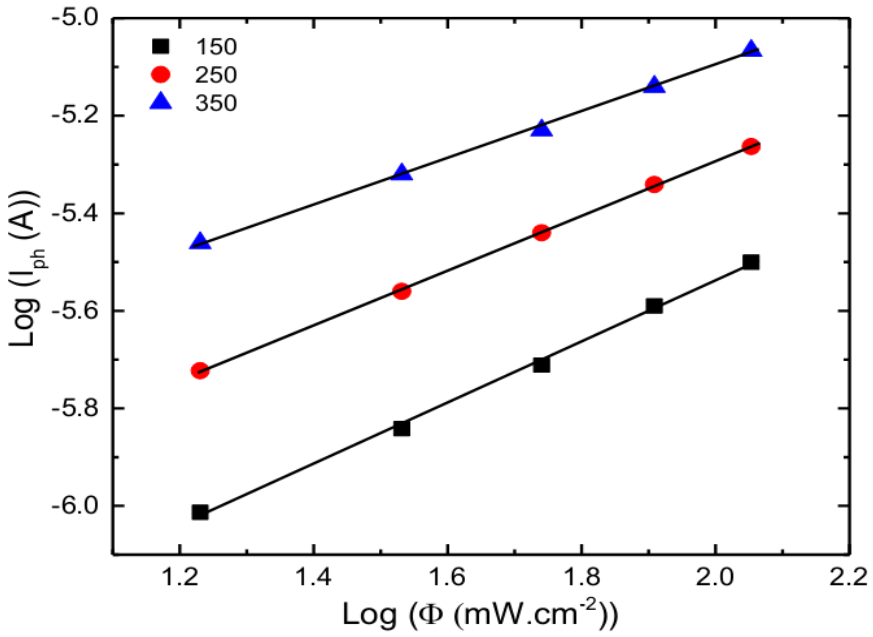

Figure 6.8 Variation of Log (I_{ph}) – Log (Φ) at 150, 250, and 350 K for CIGS thin film sample.

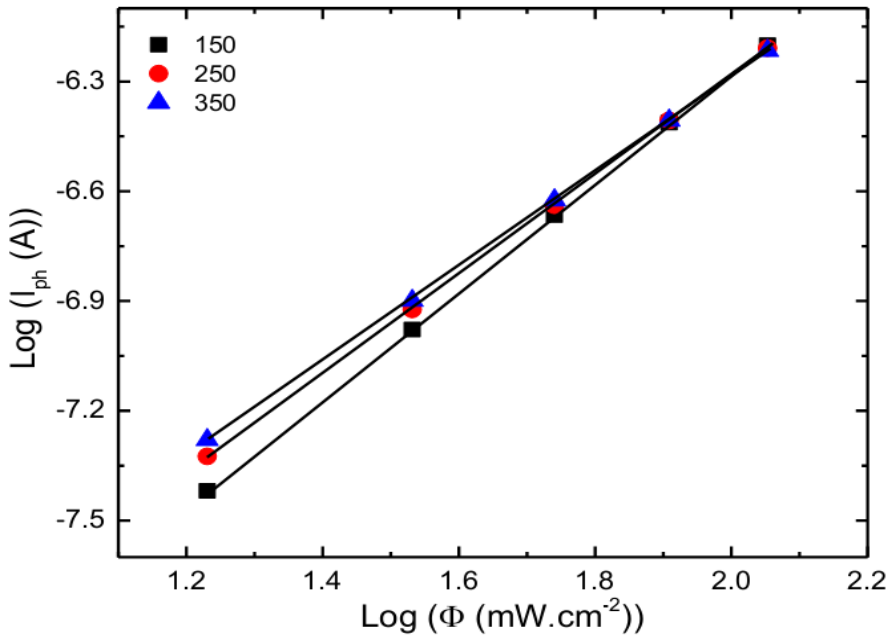

Figure 6.9 Variation of Log (I_{ph}) – Log (Φ) at 150, 250, and 350 K for QDs coated CIGS thin film sample.

As clearly seen from the figures, photocurrent (Iph) increased with increasing light intensity. Photocurrent associated with illumination intensity as I_{ph} α Φ^n, where power exponent n was calculated from the slope of Log (I_{ph}) vs. Log (Φ). The case of n<1, and n>1 correspond to "sublinear" and "supralinear" photoconductivities, respectively. The calculated n values were given in Table 6.2.

For the CIGS thin film sample, the n values were calculated from the slope of Figure 6.8 and were found to be 0.63, 0.56, and 0.47 for 150, 250, and 350 K, respectively. The character of photocurrent for CIGS thin film sample was sublinear. On the other hand, n values of QDs coated CIGS thin film sample were calculated from the slope of Figure 6.9 and were found as 1.48, 1.35, and 1.29 for 150, 250, and 350 K, respectively. These results indicated that the character of photocurrent for CIGS thin film sample changed with coating QDs layer from sublinear to supralinear. This change implies an increase in lifetime with photoexcitation intensity with existing of QDs layer.

Table 6.2 n values of CIGS thin films without and with QDs layer found from Log (I_{ph}) – Log (Φ) plots.

	n value		
Sample / Temperature (K)	**150**	**250**	**350**
CIGS	0.63	0.56	0.47
CIGS+QDs	1.48	1.35	1.29

6.1.4.2 Hall Effect Measurement

The Hall Effect measurements of CIGS thin film samples without and with PbS QDs layer were performed at room temperature condition and results were tabulated in Table 6.3.

Table 6.3 The values of resistivity, sheet resistance, carrier density, Hall coefficient and mobility of CIGS thin film samples without and with PbS QDs layer which were found from Hall Effect measurements.

Sample Name	**Resistivity [Ω.cm]**	**R_{sheet} [Ω/□]**	**Carr.Density [1/cm^3]**	**Hall Coeff. [cm^3/C]**	**μ [cm^2/(V.s)]**
CIGS	$6.44x10^{-1}$	$6.35x10^{6}$	$1.71x10^{18}$	3.64	9.56
CIGS+QDs	$6.45x10^{-1}$	$1.08x10^{6}$	$6.12x10^{17}$	10.21	15.81

It is known that the conductivity is expressed in terms of mobility (μ) and free charge carrier concentration (n or p) related by σ= nqμ or σ= pqμ expressions depending on material type. Here, n and p are the free electron and free hole concentrations, respectively. Since both samples were found to be conducting as p-type confirmed by both hot-probe and Hall effect measurements, the room temperature hole concentration of the CIGS thin film samples without and with PbS QDs layer was calculated as $1.71x10^{18}$ and $6.12x10^{17}$ cm^{-3}, respectively. As seen from Table 6.3, the Hall coefficient values were found as 3.64 and 10.21 cm^3/C for CIGS and QDs

coated CIGS, respectively. The resistivity value of sample were almost the same and were found as $6.64x10^{-1}$ to $6.65x10^{-1}$ Ω.cm for CIGS thin film and CIGS+QDs samples, respectively. The mobility values CIGS thin film samples without and with PbS QDs layer were calculated as 9.56 to 15.81 $cm^2/(V.s)$, respectively. The mobility inproved with coating QDs layer. The sheet resistance (R_{sheet}) values were calculated as $6.35x10^6$ and $1.08x10^6$ Ω/□ for CIGS and CIGS+QDs samples, respectively. As seen from Table 6.3, R_{sheet} value and carrier density decreased and other parameters incresed with coating QDs layer on CIGS thin film. This result showed that coating QDs layer on the CIGS thin films improve the electrical properties of samples.

6.1.4.3 Current-Voltage Characteristics of the n-Si/p-CIGS and n-Si/p-CIGS/QDs p-n Heterojunction Devices

In order to investigate the effect of QDs layer inside CIGS thin film based devices, the photovoltaic behavior of the n-Si/p-CIGS and n-Si/p-CIGS/QDs p-n heterojunctions were studied as explained in the experimental section. Both devices were deposited at the same deposition conditions and n-type Si (111) wafers having the resistivity of 1-3 (Ω.cm) were used as the substrates. The device structure of (Ag/n-Si/p-CIGS/In) used as a reference for the ones with QDs layer on the surface of CIGS thin film (Ag/n-Si/p-CIGS/QDs/In). Both devices had $7.5x10^{-3}$ cm^3 top metal contact area in circular shape. Figure 6.10 and Figure 6.11 show current-voltage (I-V) characteristics of investigated devices for forward and reverse DC bias voltages ranging from -2 V to +2 V in dark and the temperature range of 220K and 360 K for the reference sample and the one with QDs layer, respectively.

In order to investigate the rectifying behavior of the devices, the data were analyzed by the standard diode equation (Eqn. 2.13). The ideality factor, saturation current, barrier height, series resistance, and shunt resistance of the two device structures were calculated from the slope and intercept of the linear region of the semi-logarithmic plots of I-V curves and tabulated in Table 6.4, Table 6.5, and Table 6.6.

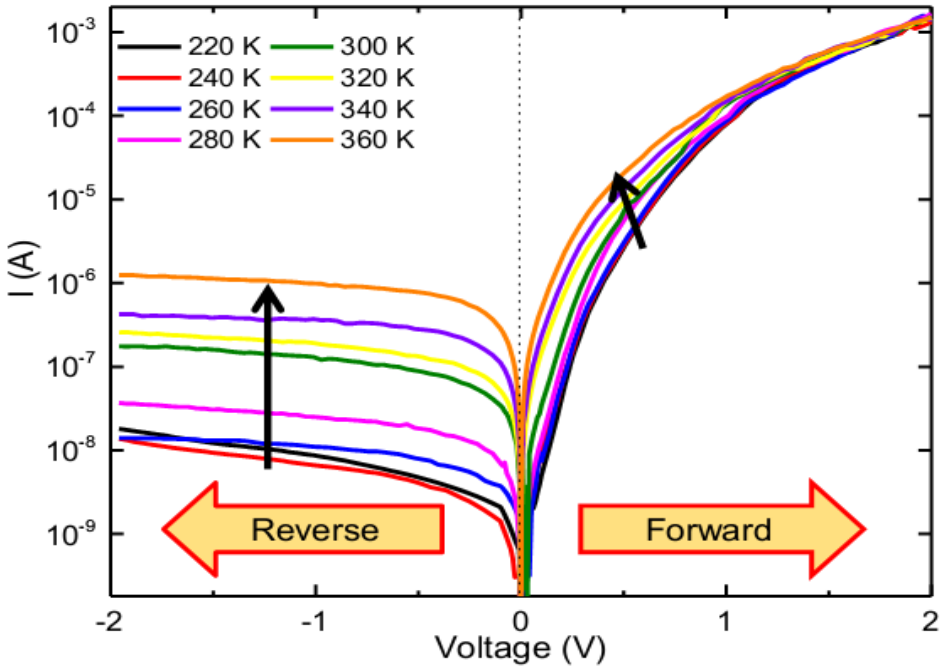

Figure 6.10 Dark forward and reverse semi-logarithmic I-V characteristics for a typical Ag/n-Si/p-CIGS/In (reference device) structure in the temperature range of 220 - 360 K.

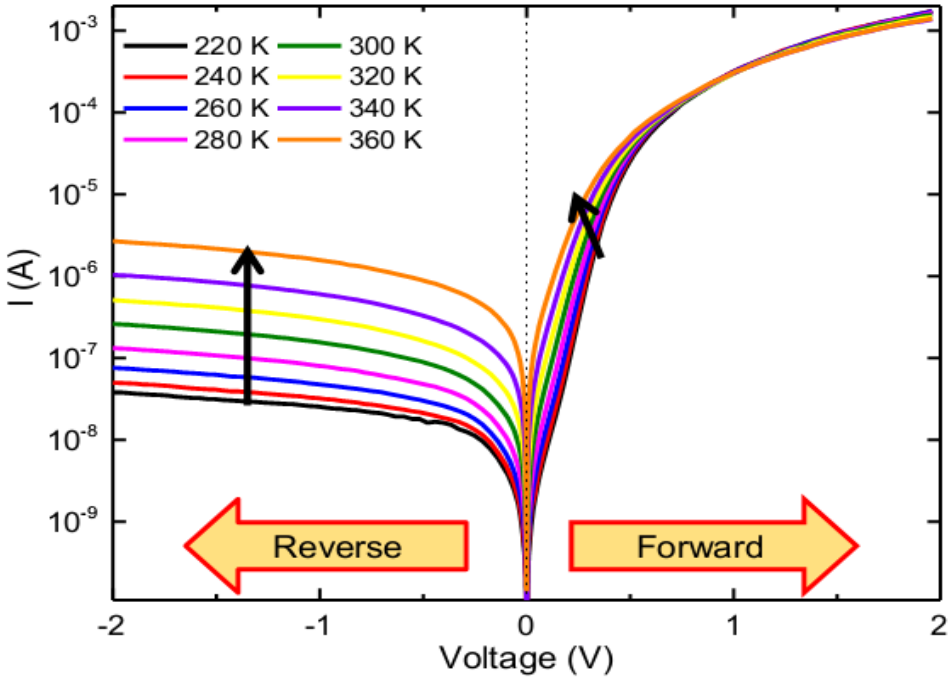

Figure 6.11 Dark forward and reverse semi-logarithmic I-V characteristics for typical Ag/n-Si/p-CIGS/PbS QDs/In structure in the temperature range of 220 - 360 K.

Table 6.4 The ideality factor and saturation current for the reference device and for the one with QDs layer calculated from the temperature dependent I–V analysis.

T (K)	n (ref.)	n (with QDs)	Io (A) (ref.)	Io (A) (with QDs)
220	2.54	2.36	9.40×10^{-10}	9.62×10^{-10}
240	2.33	2.12	1.22×10^{-9}	1.06×10^{-9}
260	2.13	1.94	4.46×10^{-9}	1.82×10^{-9}
280	1.91	1.77	2.47×10^{-8}	2.98×10^{-9}
300	1.88	1.66	3.76×10^{-8}	5.60×10^{-9}
320	1.87	1.60	6.28×10^{-8}	9.87×10^{-9}
340	1.85	1.57	1.81×10^{-7}	2.92×10^{-8}
360	1.80	1.43	7.59×10^{-7}	8.06×10^{-8}

Table 6.5 The barrier height for the reference device and for the one with QDs layer calculated from the temperature dependent I–V analysis.

T (K)	qΦb (eV) (ref.)	qΦb (eV) (with QDs)
220	0.60	0.60
240	0.65	0.65
260	0.68	0.70
280	0.69	0.74
300	0.73	0.78
320	0.77	0.82
340	0.79	0.85
360	0.80	0.87

The ideality factors were calculated in between 1.80 and 2.54 for the reference device and in between 1.43 and 2.36 for the device with QDs layer in the temperature range of 220-360K. The ideality factor decreased with increasing temperature. Moreover, the introduction of the QDs layer improves the device performance and causes the decrease in the ideality factor. In general, n=1 indicates pure thermionic emission mechanism which is the thermally induced flow of carriers from a surface or over a potential energy barrier and n>1 represents the contribution of the other conduction mechanisms to the carrier transport in the junction region, such as recombination and tunneling. The values of n were found to be greater than one for both samples which implies that the recombination might be dominant transport mechanism model and the thermally assisted tunneling and minority carrier injection might also contribute to the conduction mechanism for both devices [149], [150].

The saturation currents were calculated in between 9.40×10^{-10} A and 7.59×10^{-7} A for reference device and 9.62×10^{-10} A and 8.06×10^{-8} A for device with QDs layer. The barrier height value were found in between 0.60 V and 0.80 V for the reference and 0.60 V and 0.87 V for QDs layer inserted device. The barrier height increased with adding QDs layer and also increased with increasing temperature.

Table 6.6 The series resistance and shunt resistance of the reference device and the one with QDs layer calculated from the temperature dependent I–V analysis.

T (K)	**Rs (Ω cm^{-2}) (Ref)**	**Rs (Ω cm^{-2}) (with QDs)**	**Rsh (Ω cm^{-2}) (Ref)**	**Rsh (Ω cm^{-2}) (with QDs)**
220	121.5	18.5	2021.6	3591.8
240	97.2	17.6	2294.3	2847.7
260	87.6	15.3	1994.3	2670.2
280	63.5	15.5	1826.0	2262.1
300	56.6	15.4	1438.1	2072.4
320	43.8	14.6	1311.6	1909.1
340	32.2	13.6	1216.3	1857.3
360	22.7	11.9	1029.2	1889.3

The main contribution of adding QDs layer was observed for series resistance (R_S) value. R_S dramatically decreased from 121.5 $\Omega \cdot cm^2$ to 18.5 $\Omega \cdot cm^2$ after inserting the QDs layer inside devices at the temperature of 220 K. The temperature also affected the R_S value and it was calculated 22.7 $\Omega \cdot cm^2$ at temperature of 360 K without QDs layer. On the other hand, for device with QDs at that temperature, the R_S was found 11.9 $\Omega \cdot cm^2$ which was nearly half of the R_S value of reference device. Therefore, QDs layer made device less resistance and improved the carrier's mobility in structure. The same behavior was observed for shunt resistance (R_{Sh}) values. The possible reason for decreasing in R_S and increasing in R_{Sh} is the faster recombination in the space charge region between CIGS layer and PbS QDs layer and this case leads to rapid depletion of the separated generated charge in the interface layer. Additionally, increase in temperature might cause de-trapping or bond breaking mechanisms so the density of the free charge carriers may be increased by these mechanisms and decrease the values of R_S and R_{Sh} [151]–[153].

In order to clarify the effect of QDs layer inside structure, the dark I-V of reference and with QDs layer was plotted in same graph for room temperature and it was given in Figure 6.12. As clearly seen from figure, QDs layer improves current in the forward bias region.

The illuminated I-V measurements of reference device and QDs layer added device were also carried out and given in Figure 6.13. The results of experiment was almost the same as a result of dark I-V measurements of devices.

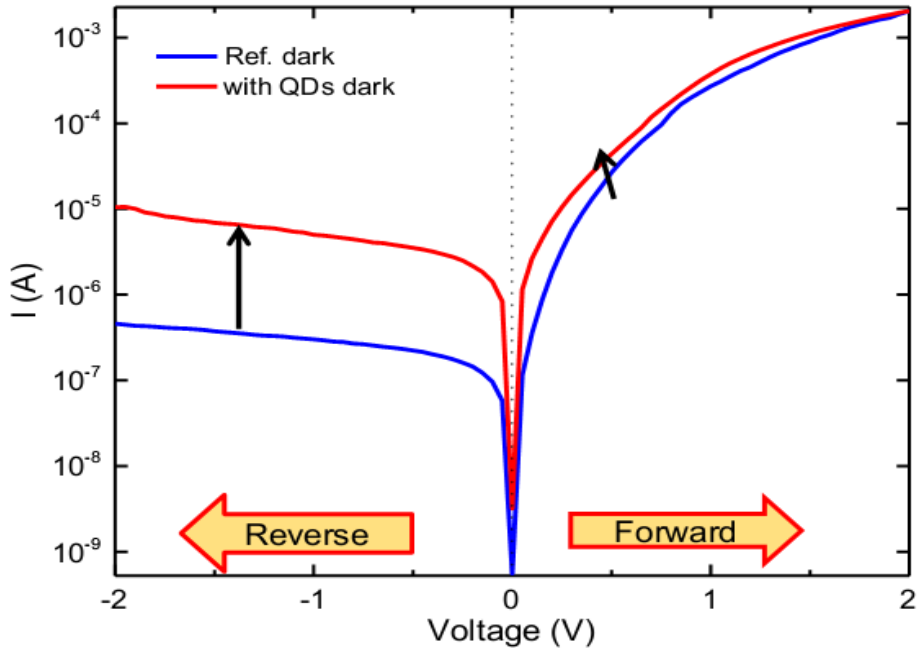

Figure 6.12 The comparison of dark current –voltage (I-V) characteristic of the Ag/n-Si/p-CIGS/In (reference device) and Ag/n-Si/p-CIGS/PbS QDs/In devices at room temperature.

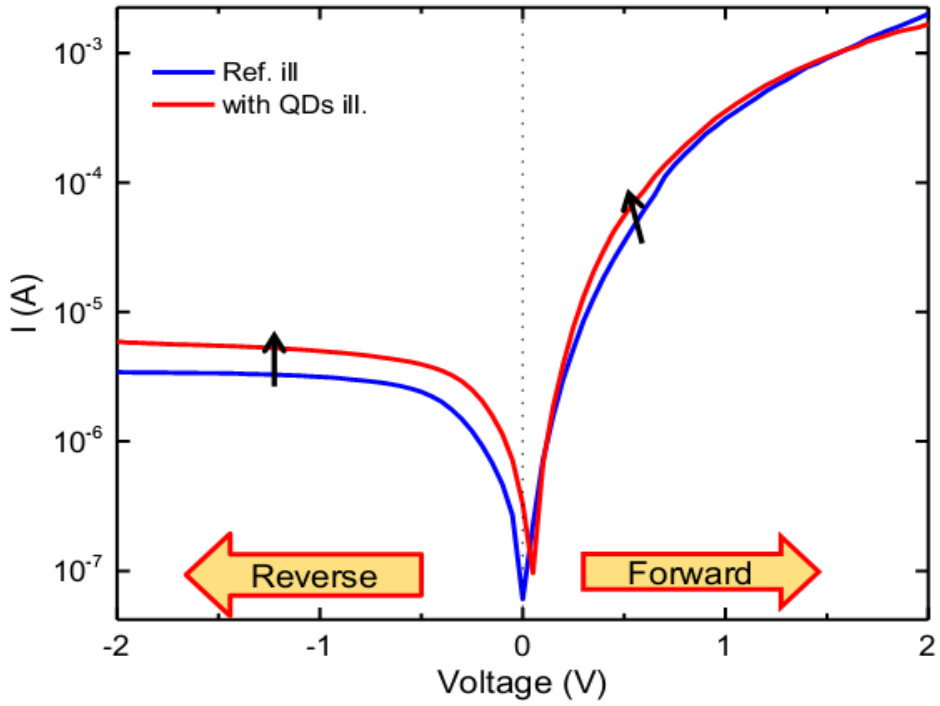

Figure 6.13 The comparison of current –voltage (I-V) characteristic of the Ag/n-Si/p-CIGS/In (reference device) and Ag/n-Si/p-CIGS/PbS QDs/In devices under the illumination at room temperature.

6.1.4.4 Capacitance-Voltage Characteristics of the n-Si/p-CIGS and n-Si/p-CIGS/QDs p-n heterojunction Devices

The dark capacitance-voltage (C-V) measurements at different frequencies were performed to obtain the further information about adding QDs layer inside the junction at room temperature and the results are shown in Figure 6.14 and Figure 6.15 for the two device structures under investigation. All devices were treated as a parallel plate capacitor during the measurements and C-V measurements as a function of frequency have been executed by applying the bias voltage in between -2 V and +2 V and in the frequency range of 10 kHz - 1000 kHz. The C-V variation of both devices showed diode behavior and built in voltage (V_{bi}) occurred in the CIGS thin film due to high resistance of this layer. As seen from figures, the C-V variations showed the same behavior at different frequencies for both devices. The capacitance value at forward bias region remained almost constant and capacitance value decreased with increasing frequencies. The zero bias capacitance values of reference device and QDs added device changed in between 0.60 - 0.34 nF and 0.80 - 0.30 nF, respectively. The zero bias capacitance value increased with adding QDs layer while it decreased with increasing frequency values.

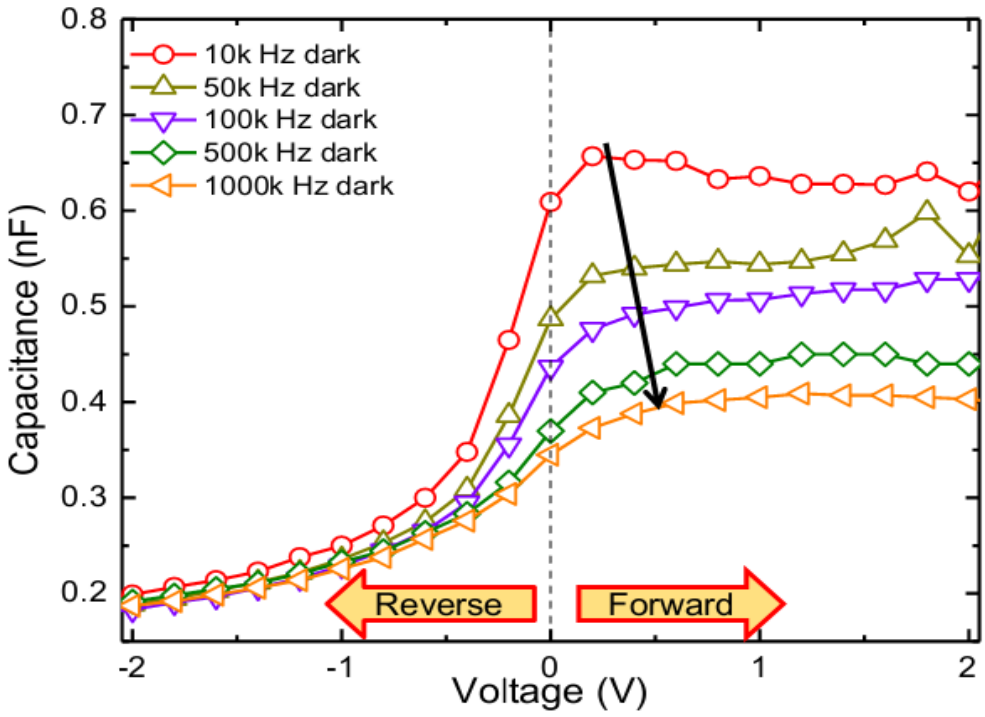

Figure 6.14 Capacitance versus voltage (C-V) plots of Ag/n-Si/p-CIGS/In p-n heterojunction at room temperature for different frequencies.

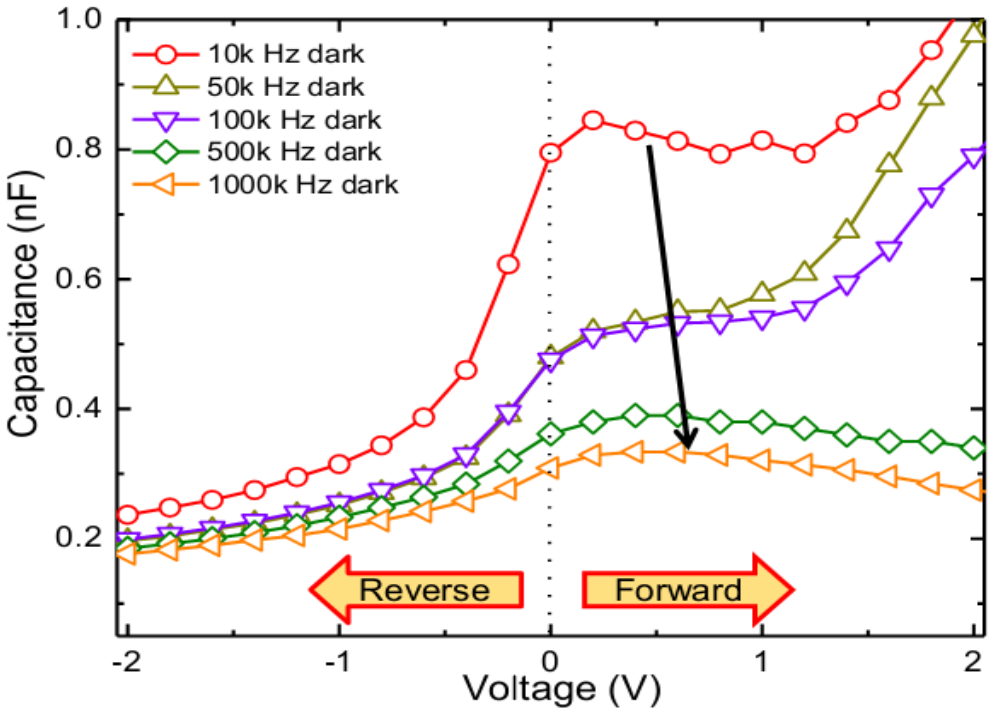

Figure 6.15 Capacitance versus voltage (C-V) plots of Ag/n-Si/p-CIGS/PbS QDs /In p-n heterojunction at room temperature for different frequencies.

In order to compare the effect of QDs layer inside structure, the dark and illuminated room temperature C-V variations of the two device structures at 10 kHz were plotted on the same graph as illustrated in Figure 6.16. As clearly seen from figure, QDs layer improve the the capacitance values for dark and illuminated conditions.

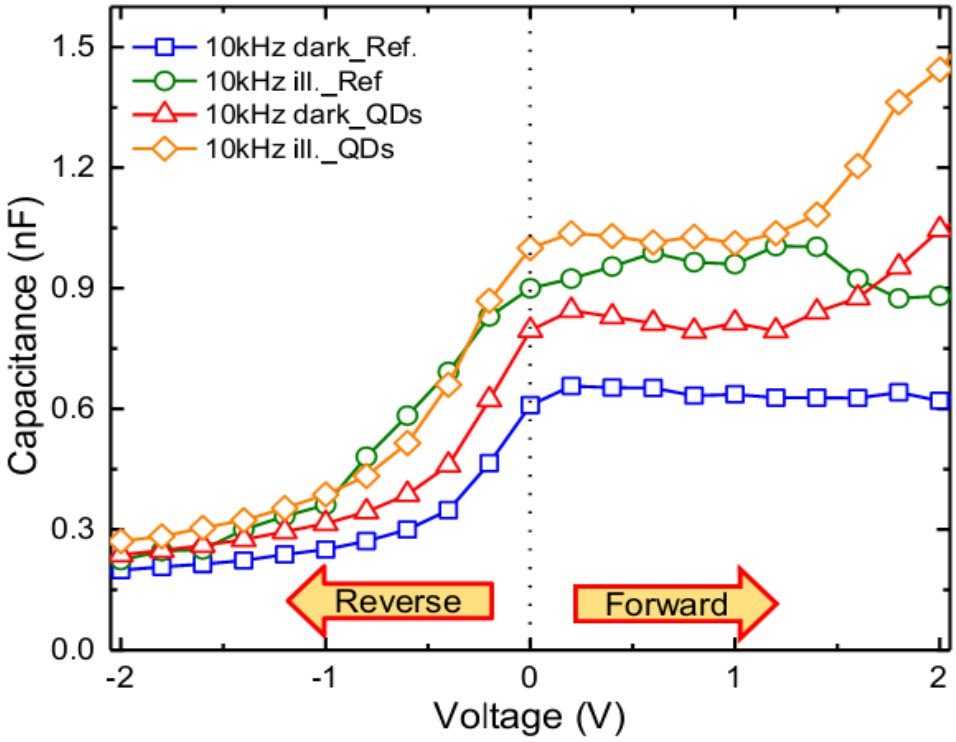

Figure 6.16 The comparison of the room temperature capacitance–voltage (C-V) characteristic of the Ag/n-Si/p-CIGS/In (reference device) and Ag/n-Si/p-CIGS/PbS QDs/In device in dark and under the illumination.

Because of very low resistivity value of n-Si wafer with respect to p-CIGS thin film, it was assumed that the p-CIGS/n-Si heterojunction behave as one sided abrupt junction. Therefore, the acceptor concentration (N_A) of the absorber layer (p-CIGS) and built in voltage (V_{bi}) values for the reference device and the device with QDs layer were calculated from Mott–Schottky curves by using C-V measurements and following equation [154], [155].

$$C^{-2} = 2\left[\frac{(V_{bi} - V - {}^{kT}/_{q})}{qA^2\varepsilon\varepsilon_0 N_A}\right] \quad (6.3)$$

Mott-Schottky curves (C^{-2} versus V) for dark and illuminated conditions at the frequency value of 10 kHz were given in Figure 6.17 and Figure 6.18, respectively. The values of N_A and V_{bi} in dark condition were obtained as about 5.2 $x10^{15}$ cm^{-3} and 1.15 V for the reference device and 7.1$x10^{15}$ cm^{-3} and 1.01 V for the device with QDs layer, respectively. The values of N_A and V_{bi} under the illumination were calculated as 6.5 $x10^{15}$ cm^{-3} and 0.90 V for the reference device and 8.2$x10^{15}$ cm^{-3} and 0.76 V for the device with QDs layer, respectively. All calculated N_A and V_{bi} values were tabulated in Table 6.7.

Table 6.7 Calculated acceptor concentration and built in voltage values for the reference and QDs layer added devices in dark and under the illumination.

Sample Name	**N_A (cm^{-3})**	**V_{bi} (V)**
Ref. dark	5.2$x10^{15}$	1.13
With QDs dark	7.1$x10^{15}$	1.01
Ref. illuminated	6.5$x10^{15}$	0.90
With QDs illuminated	8.2$x10^{15}$	0.76

The relative improvement in acceptor concentration of junction was found as 39 % and 26 % with adding QDs layer for dark and illuminated conditions, respectively. The results indicated that the existence of QDs layer inside device increased the acceptor concentration and decreased the built in voltage values for both conditions dark and illumination.

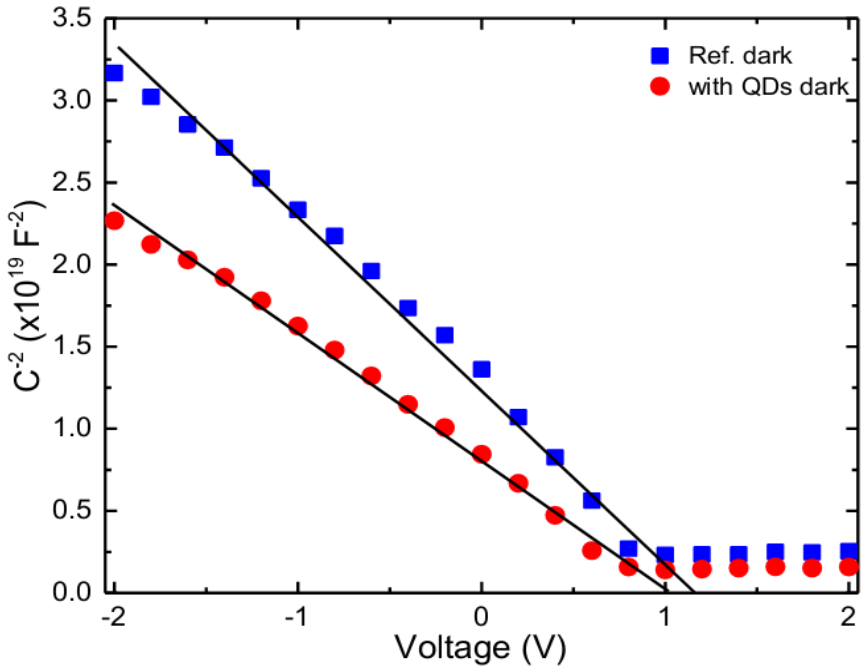

Figure 6.17 C^{-2} versus V plot of n-Si/p-CIGS and n-Si/p-CIGS/PbS QDs p-n heterojunction devices in dark at room temperature.

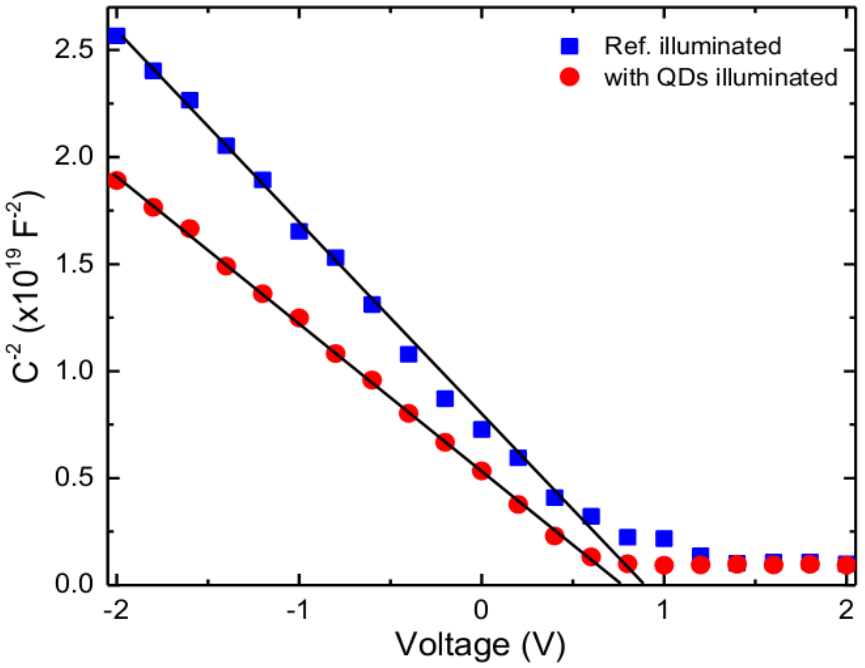

Figure 6.18 C^{-2} versus V plot of n-Si/p-CIGS and n-Si/p-CIGS/PbS QDs p-n heterojunction devices under illumination at room temperature.

6.2 Organic Solar Cell Devices

6.2.1 Introduction

In order to collect photon having energy in the near IR region, PbS QDs layer was inserted inside polymer solar cell devices. Figure 6.19 shows the main idea of the work. As clearly explained from illustration, Poly (3-hexylthiophene) (P3HT) and poly (6,6-phenyl C61-butyric acid methyl ester) (PCBM) polymer active layer collects the photons from visible side of solar spectrum and PbS QDs, having emission value at 842 nm and absorption at 718 nm, collects the photons from near-IR that is not collected by polymer active layer. Therefore, the absorption ranges of P3HT:PCBM and PbS QDs complement each other and make these two materials appropriate for using in the same device structure. The structure of the inverted polymer solar cell (IPSC) with PbS QDs was illustrated in Figure 6.20 (a). As clearly seen from illustration, QDs thin film layer sandwiched in between the ZnO and P3HT:PCBM polymer active layers. The band structure of IPSC and PbS QDs was shown in Figure 6.20 (b). In inverted solar cell, solar irradiation comes from ITO coated glass side and passes to polymer active layer. After light coming to the device, electron - hole pairs are created in active polymer layer. Then, electrons and holes move to back and top electrodes, respectively. In IPSC devices, ZnO layer was used as an electron transport layer and MoO_3 was used as a barrier.

The purpose of this chapter is to show inserting the QDs thin film layer in IPSC and increase the power conversion efficiency (PCE) value of solar cells by means of collecting the photon in near-IR which is normally not collected by IPSC devices. Moreover, we also showed that the increasing percent in PCE was depending on QDs amounts.

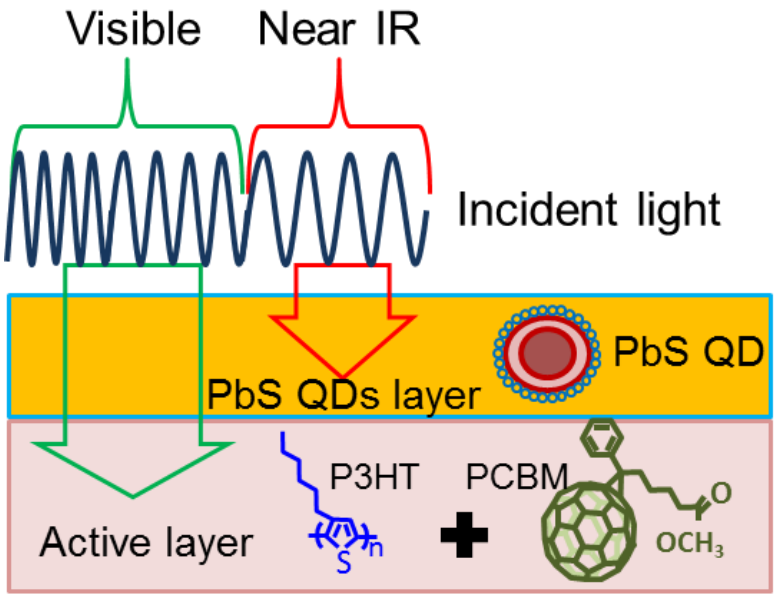

Figure 6.19 Schematic representation of quantum dots thin film layer and active polymer layer inside inverted polymer solar cells.

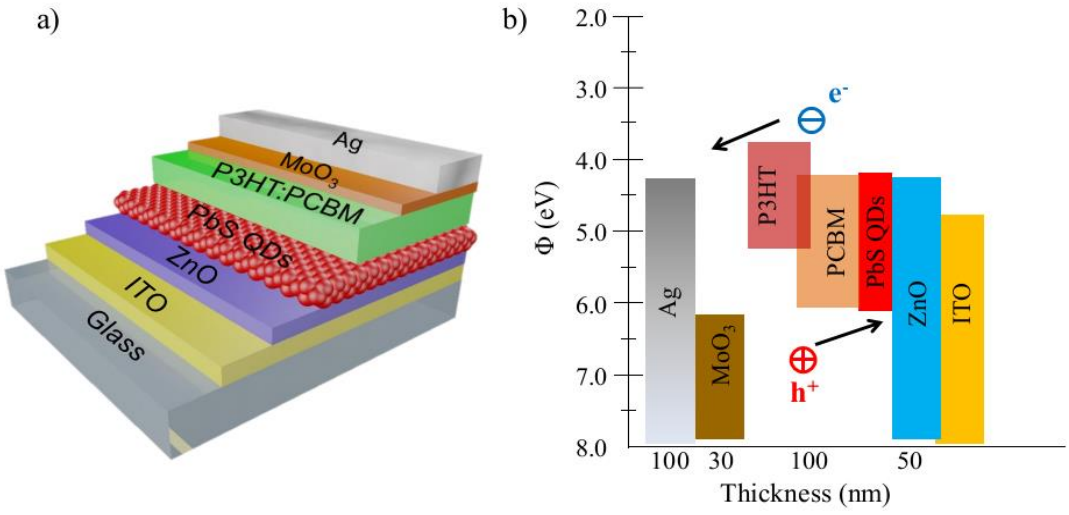

Figure 6.20 Schematic representations of a) the inverted low band gap polymer solar cell device with QDs thin film layer containing glass/ITO/ZnO/PbS QDs/P3HT:PCBM/MoO_3/Ag layers, respectively. And b) band position diagram of PbS QDs incorporated Inverted polymer solar cell (IPSC).

6.2.2 Characterization of Quantum Dots and Polymer Layers

In order to understand the structure of IPSC device with QDs layer, we performed some characterization methods. Figure 6.21 and Figure 6.22 show the transmission and the normalized absorbance of PbS QDs, polymer and polymer+QDs, respectively. As clearly seen from figures, polymer active layer has absorption value in the visible range while PbS QDs contributes the absorbance value in the range of near-IR. When these layers were brought together, absorbance significantly changed with contribution of QDs layer. The main contribution of QDs was in the near-IR region as theoretically expected.

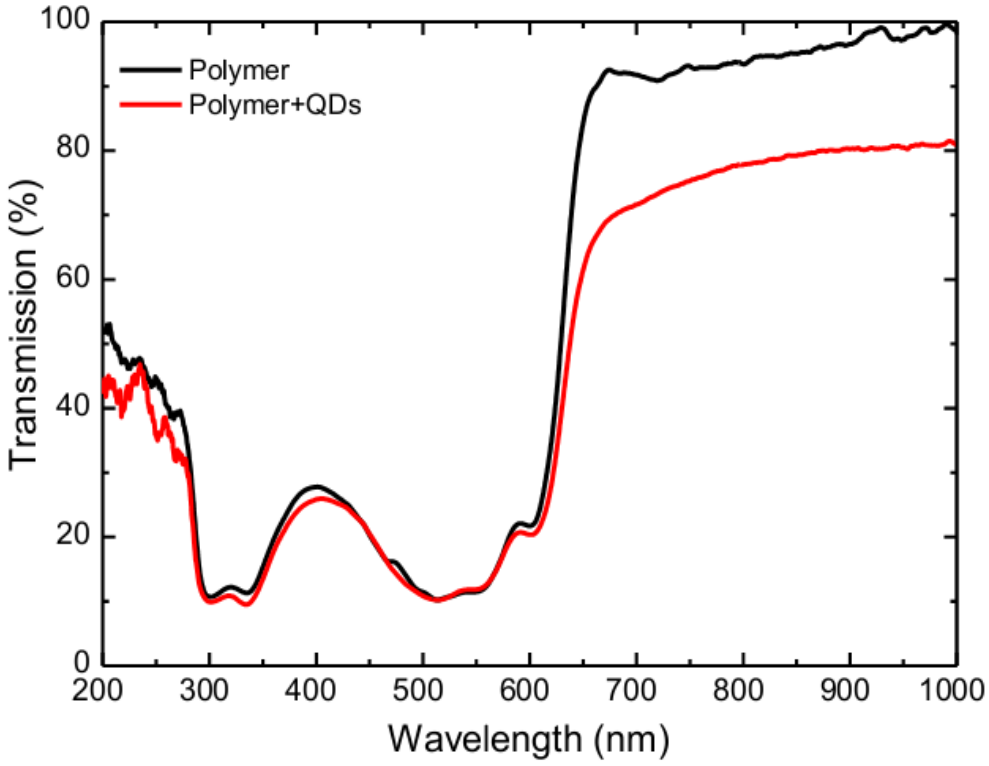

Figure 6.21 Transmission graph of P3HT:PCBM polymer with and without PbS QDs.

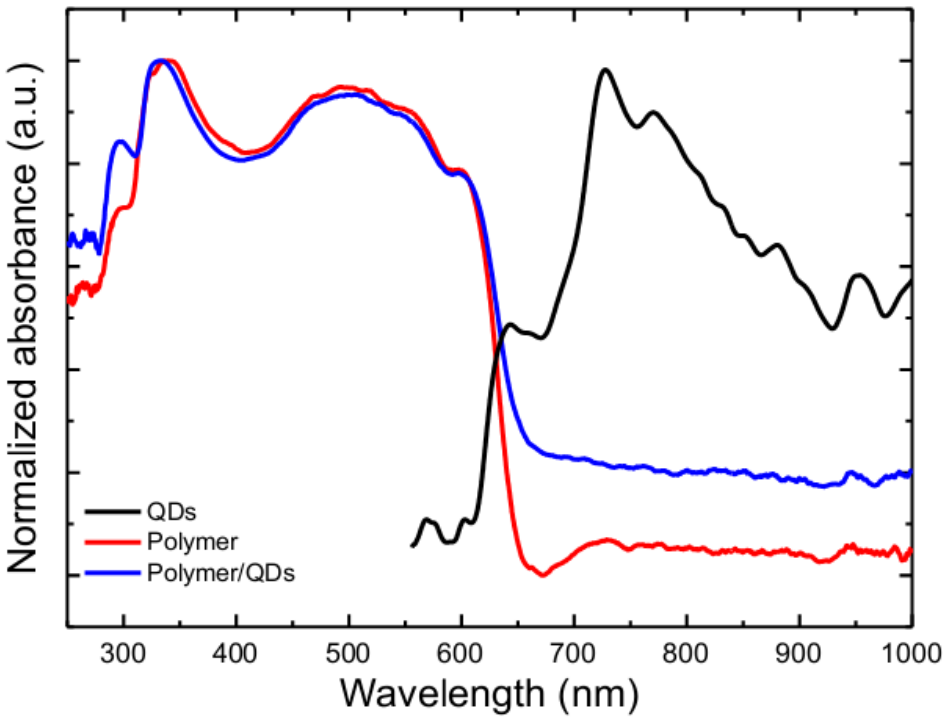

Figure 6.22 Normalized absorbance of P3HT:PCBM polymer, PbS QDs, and P3HT:PCBM polymer with PbS QDs layer.

The confocal Raman spectrum of PbS QDs, polymer and polymer + QDs thin films were recorded at room temperature condition with the Nd:Yag laser, having 532 nm excitation wavelengths and the results were shown in Figure 6.23. As clearly seen from Figure 6.23 (a), the most intensive Raman peak of P3HT:PCBM polymer is at 1442 cm^{-1} which is assigned to the symmetric C=C stretching and the other Raman peaks are at 728, 1088, 1376, and 1509 cm^{-1} which are assigned to the C-S-C ring deformations, C–H bending, C3–C4 stretching, and antisymmetric C=C stretching, respectively [156]–[165]. Furthermore, the QDs layer has a most intense Raman peak at 78 cm^{-1} and the other Raman peaks of QDs layer are at 444, 557, 776 870, 1088, 1300, 1440, and 1650 cm^{-1}. When both layers were brought together, the effects of QDs on polymer were explicitly seen. The most intense peak of polymer and QDs together is also 1442 cm^{-1}. However, assembling of both layers resulted in new peaks emerging and increasing in some existent peak intensities as shown in Figure 6.23 (a).

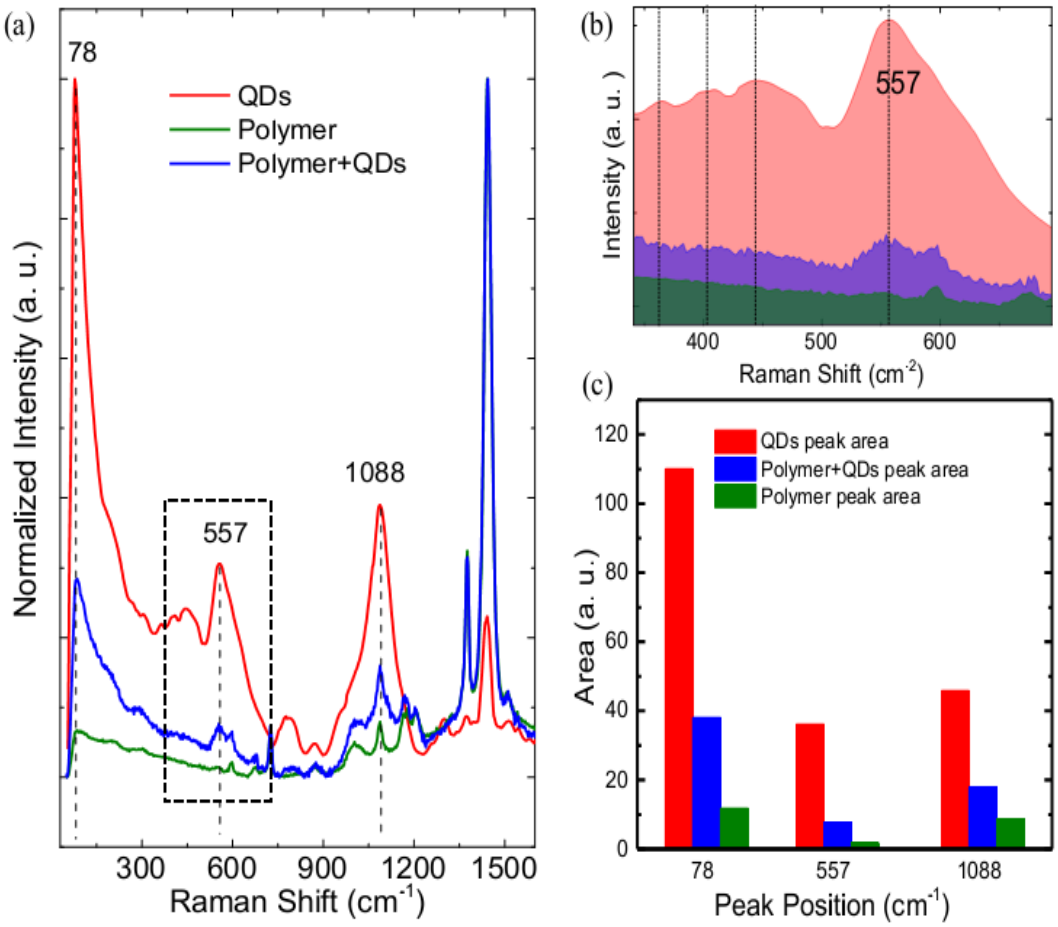

Figure 6.23 a) Normalized Raman spectra of P3HT:PCBM polymer, PbS QDs thin film, and P3HT:PCBM polymer with PbS QDs b) Raman shift area at 557 cm^{-1} c) Comparison of Raman shift areas for QDs, polymer and polymer+QDs at 78 cm^{-1}, 557 cm^{-1}, and 1088 cm^{-1}.

We also analyzed the Raman shift peak areas for specific effected regions, namely 78, 557 and 1088 cm^{-1}. In the Figure 6.23 (b), the peak area of 557 cm^{-2} is given as an example. The peak area analysis of Raman shift at 557 cm^{-1} shown that polymer did not have this peak but in the polymer + QDs sample it emerged after coating QDs layer and increased the area size under the peaks from 1.7 to 7.6 cm^2. This result is clear proof of the existence of QDs layer in the device architecture made same structural changes on the polymer layer. The Raman shift area calculation was also done for the most effected regions, namely 78 cm^{-1} and 1088 cm^{-1} and the comparison of areas was plotted in the Figure 6.23 (c). As seen from figure, all affected regions increased in areas with adding QDs layer. The change in the areas of Raman shift peaks were calculated as 11.8 to 38.1 cm^2 and 8.6 to 17.8 cm^2 for the

peaks at 78 cm^{-1} and 1088 cm^{-1}, respectively. On the other hand, there was no considerable effect of QDs layer for the most intense peak at 1442 cm^{-1} due to strong vibration of A_1 mode of P3HT:PCBM polymer layer and weak vibration of PbS QDs.

In order to obtain the further information about distribution of QDs on the polymer layer, the transmission electron microscope (TEM) measurements were carried out for QDs coated polymer sample and the TEM micrographs were demonstrated in Figure 6.24. The distribution of QDs over polymer layer can be clearly seen from TEM micrographs.

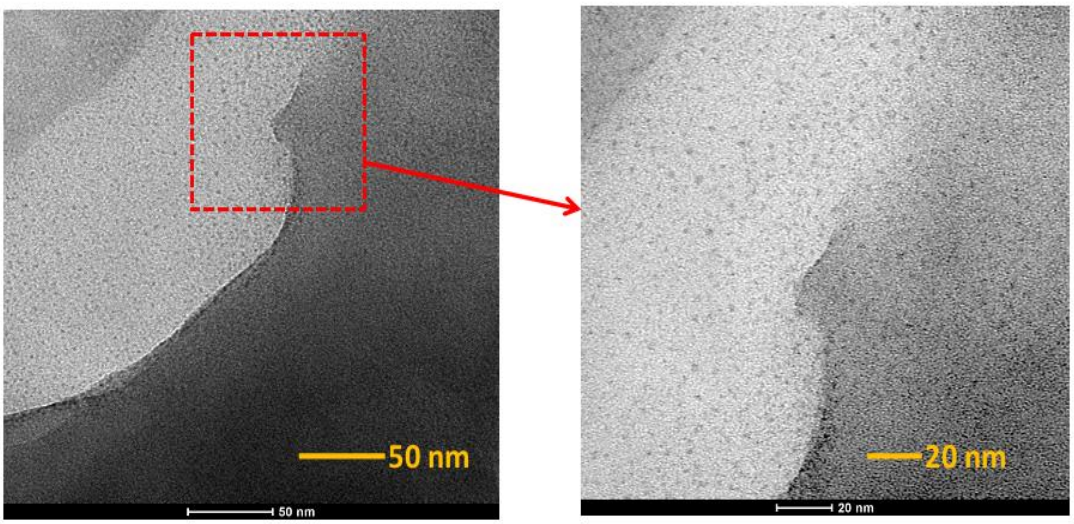

Figure 6.24 TEM micrographs of P3HT:PCBM and PbS QDs at resolutions of 50 nm and 20 nm.

The PL emission spectra of PbS QDs in toluene solution and also of the thin film were measured using the 488 nm excited wavelength with an argon ion laser and both measurements showed one major emission peak at 913 nm and 917 nm for the QDs in toluene solution and thin film, respectively as shown in Figure 6.25. The shift in the peak position from 913 nm to 917 for the thin film might be due to the small increase in the QDs size when coated on glass substrate as the thin film form.

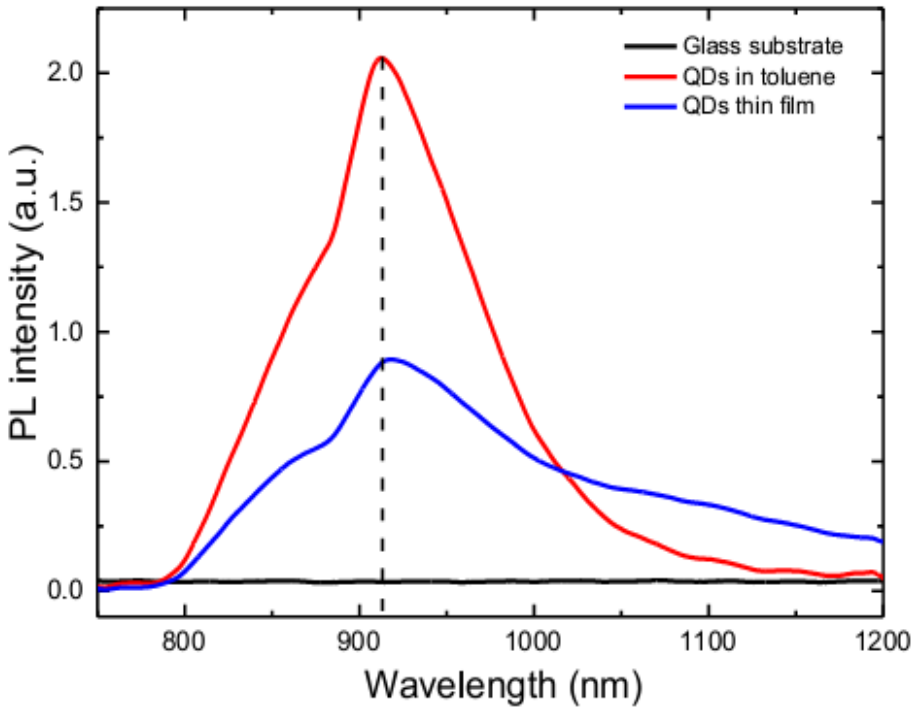

Figure 6.25 Photoluminescence spectra of glass substrate, PbS QDs in toluene and PbS QDs thin film.

6.2.3 Current-Voltage Characteristics of IPSC with and without QDs layer

A typical set of room temperature dark and illuminated Current- Voltage variations in forward and reverse bias regions ranging from -1.5 V to +1.5 V under 1.5AM global light were given Figure 6.26 for the IPSC devices with and without QDs layer. The reference IPSC device structures of glass/ITO/ZnO/P3HT:PCBM/MoO_3/Ag, were fabricated as described elsewhere [96]. The IPSC devices with QDs layers were produced using glass/ITO/ZnO/PbS QDs/P3HT:PCBM/MoO_3/Ag structure. All other layers in the solar cell were kept identical excluding QDs thin film layers to understand the effect of QDs amount in the structure. The thicknesses of the QD thin film layers were changed from 1 to 5 layers. Figure 6.26 represents current density-voltage (J-V) characteristics of the fabricated devices without QDs layer and with different amount of QDs layers.

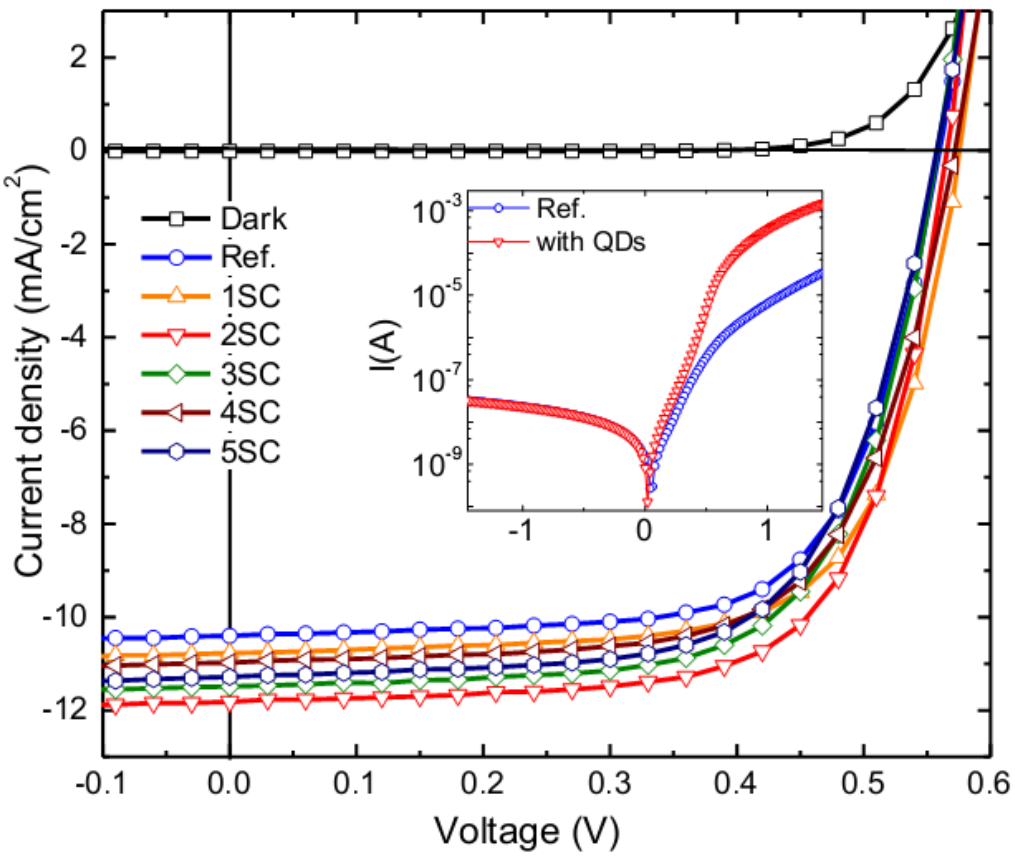

Figure 6.26 Current density – Voltage characteristic of the IPSC devices containing different layers of QDs thin film in dark and 1.5AM solar irradiation. Inset shows the dark semi-logarithmic current density - voltage characteristics of the device without QDs thin film layer and the device with QDs thin film layer.

PCE and all the other parameters of the solar cell devices were calculated from J-V variations given in Figure 6.26. The variation in PCE with changing in QDs layer thickness was shown in Figure 6.27. As clearly seen from the figure, PCE values changed in between 3.95% and 4.58%. The maximum efficiency value of 4.58% was found for device with 2 QDs layers. After that, PCE value of the device decreased with more than 2 layers QDs but still all devices having QDs layers had more PCE values than that of the reference device without QDs layer. It means that adding QDs thin film layer inside IPSC device structure improved the device performance relatively in between 5% and 16% when compared with reference device.

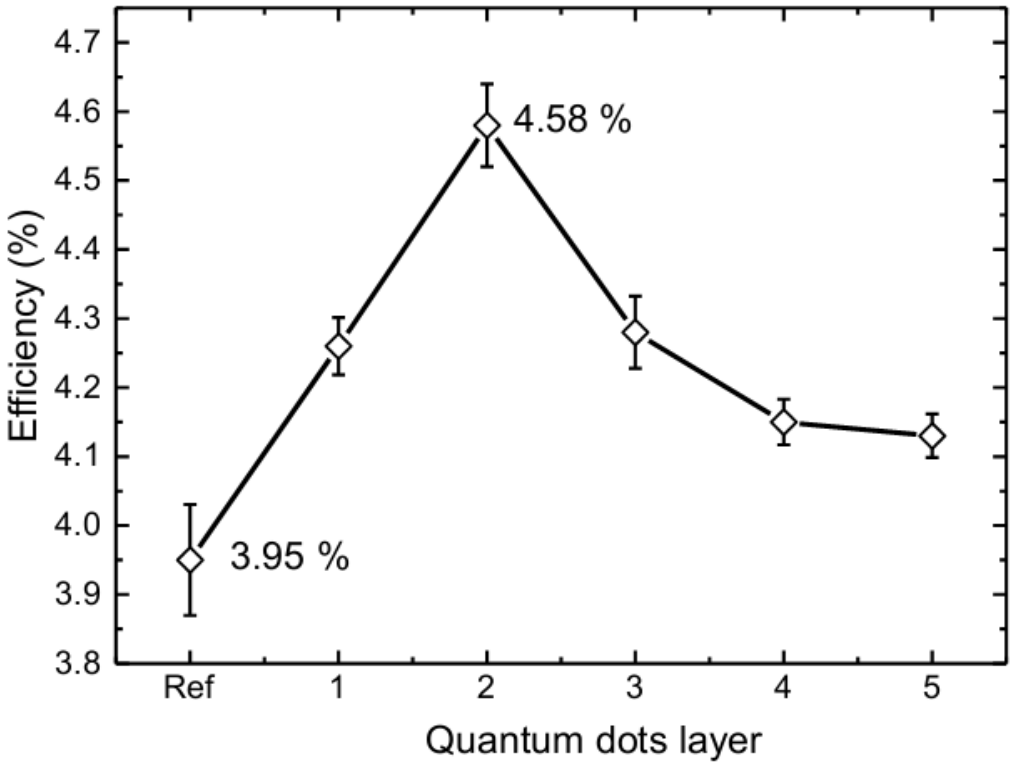

Figure 6.27 Variations of power conversion efficiency (PCE) of the IPSC device with the thickness of the QD thin film layer.

The PCE improvement in the IPSC devices with QDs thin film layer was mainly due to the lower series resistance (R_S) (6.74 Ω/cm^2 versus 5.11 Ω/cm^2) and higher short circuit current (J_{SC}) (10.40 mA/cm^2 versus 11.82 mA/cm^2) as given in Figure 6.28. The relative improvement in R_S value was calculated as 24% for most the efficient device (2 layers QDs). Therefore, the presence of the QDs layer resulted in the device with lower series resistance and the improvement the carrier's mobility. And also, QDs thin film layer covers the ZnO layer and blocks the direct contact between polymer and ITO. Hence, there are some possible reasons for the decrease in R_S value and the improvement of device parameters. The first possible reason is the faster recombination in the space charge region between ZnO and PbS QDs layer which leads to rapid depletion of the separated photo-generated carriers and decrease the series resistance (R_S) [166]. The second possible reason is the absorption of the illumination in the PbS QD sensitizer which leads the generation of electron–hole pairs. The photo generated electrons (or holes) are then transferred to the electron conductor (ZnO) and hole conductor (MoO_3) [167]. Additionally, multi exiton

generation (MEG) in colloidal PbS QDs may also improve the device efficiency and short circuit current (J_{sc}). In this process, very efficient multiple electron-hole pairs (multi excitons) are created by one photon and carrier concentration increases significantly [22], [168], [169].

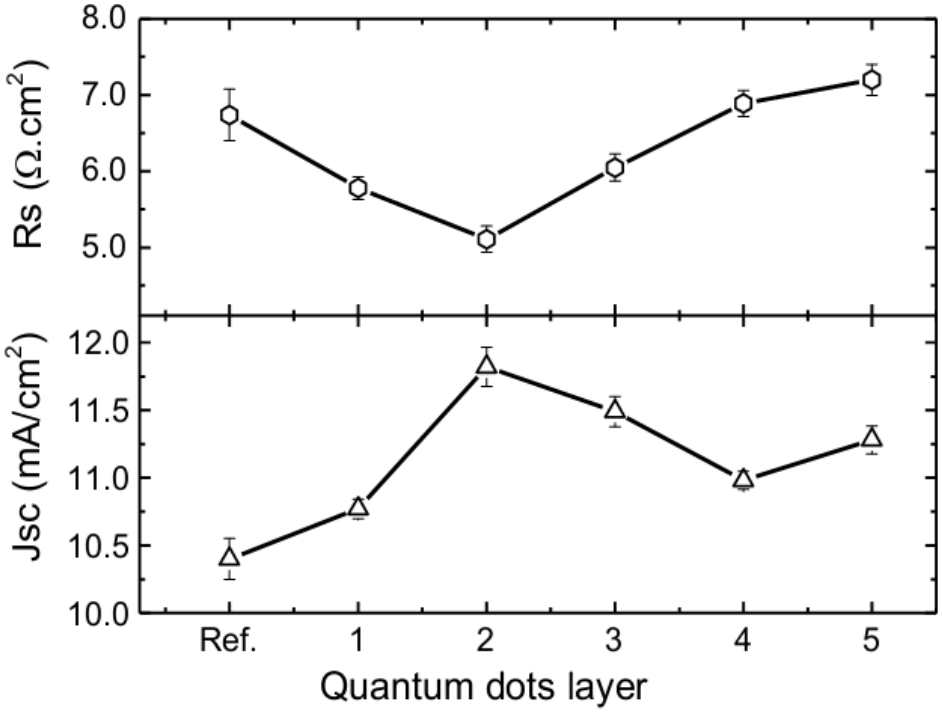

Figure 6.28 Variations of the series resistance (R_S) and short circuit current (J_{SC}) of the IPSC with the thickness of the QD thin film layers.

All IPSC parameters (R_S, FF, J_{SC} and R_{Sh}) with different QDs layer thickness were calculated from J-V measurements and the results are illustrated in Figure 6.28 and Figure 6.29. It was obvious from the figures that the structure with 2 layers QDs has the best solar cell parameters with the lowest R_S (5.11 Ω.cm^2), the highest J_{SC} (11.82 mA/cm^2) and shunt resistance (R_{Sh}) (2105 Ω.cm^2) values and also gives the highest solar cell PCE (4.58±0.06%). As seen from Figure 6.29, fill factor (FF) was calculated in between 0.65 and 0.68. Open-circuit voltage (V_{OC}) remained nearly the same in between 0.55 and 0.56 V. Moreover, after the certain amount of QDs layers the contact resistance decreases, the leakage current between layers is suppressed and R_S also decreases which refers the improvement of the carrier collection and transportation between the layers with existing QDs layer as well.

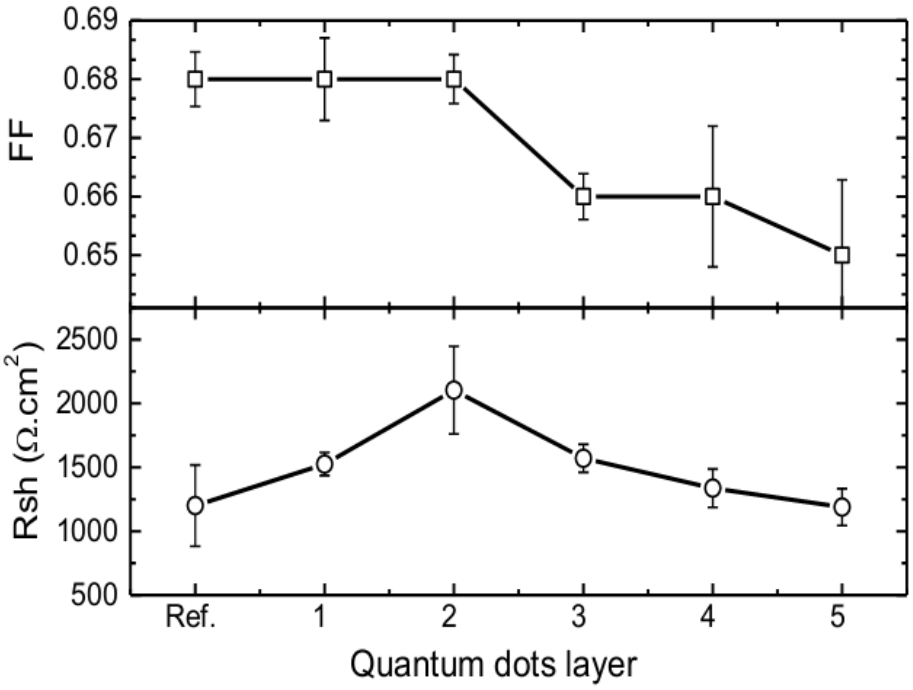

Figure 6.29 Variations of fill factor (*FF*) and shunt resistance (R_{Sh}) of the IPSC with the thickness of the QD thin film layers.

6.2.4 External Quantum Efficiency (EQE)

Quantum efficiency (QE) is defined as the ratio of the number of charge carriers collected by a photosensitive device to the number of incident photons. There are two types of quantum efficiency; namely, external quantum efficiency (EQE) and internal quantum efficiency (IQE). The EQE is ratio of the number of charge carriers collected by light converting device to the number of photons of incident radiation from outside of the device. The EQE includes the effect of optical losses such as transmission and reflection. However, the term of IQE refers to the ratio of the number of charge carriers collected by light converting device to the number of photons of incident light absorbed by device. The IQE of a device is normally computed from the ratio of its EQE and spectral absorptance as

$$IQE = \frac{EQE(\lambda)}{[1-F(\lambda)-\tau(\lambda)]} \tag{6.4}$$

here F(λ) is the spectral reflectance and τ(λ) is the device transmittance which is usually zero [170].

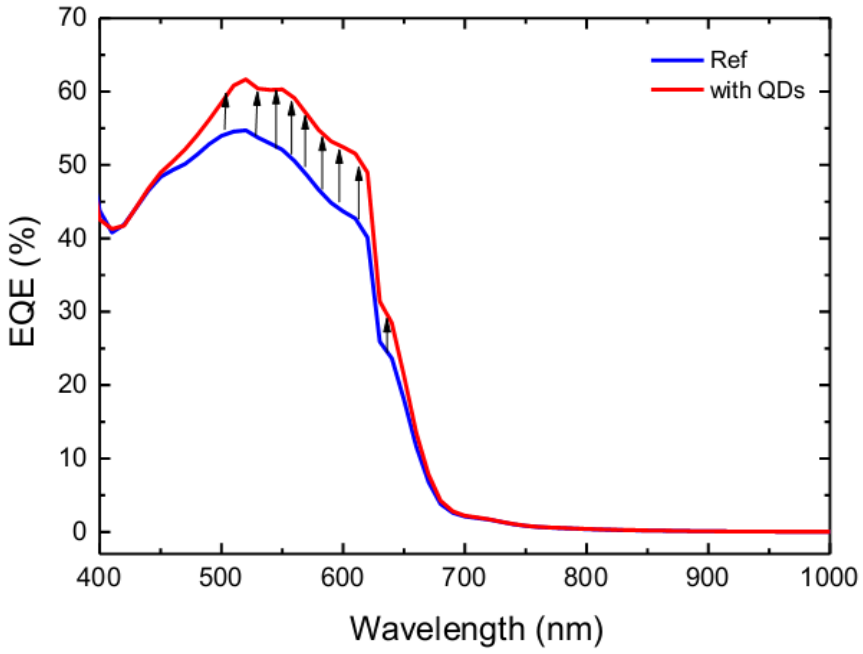

Figure 6.30 Variation of External Quantum Efficincy values of IPSC devices with and without QDs thin film layer as a function of wavelength of the incident photon.

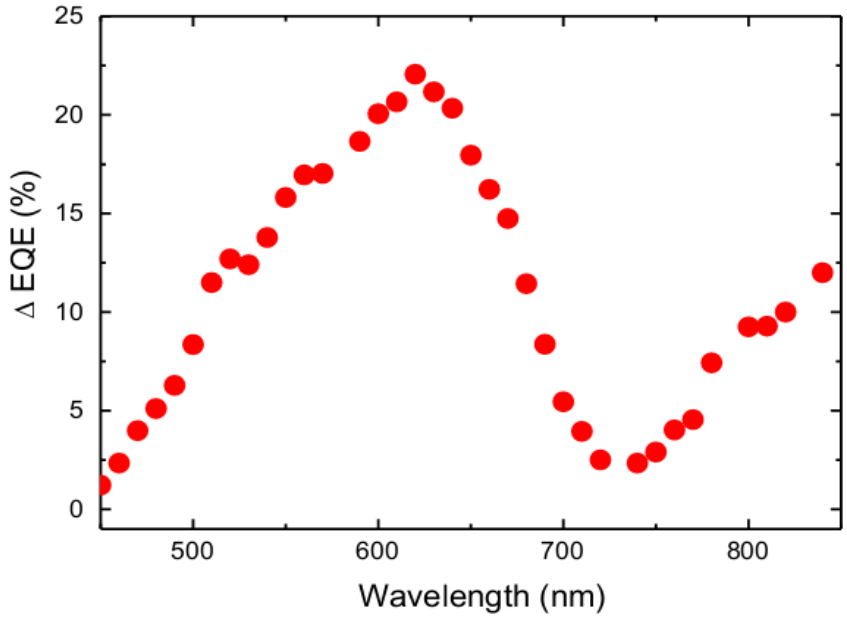

Figure 6.31 The variation of the relative change in EQE with the wavelength of the incident photons.

In order to clarify the effect of QDs layer inside IPSC, the EQE measurements were carried out and the EQE curves of devices are given in Figure 6.30 with maximum EQEs respose values of of 61% and 55% for the devices with and without QDs layer, respectively. The relative increase in EQE value was calculated in between 12% and 22% in the visible region (500 nm-700 nm) and in between 3% and 12% in the near-IR region (700 nm-850 nm) after the QDs layer is introduced as shown in Figure 6.31. Similar relative percentage increase was observed in the PCE value as mentioned before. Meanwhile, EQE results showed that the contribution of QDs thin film layer is not only in the near-IR but also in the visible range.

6.2.5 Capacitance - Voltage of IPSC Devices with and without QDs layer

For further investigation of the effect of the presence of the QDs layer on the device properties, capacitance-voltage (C-V) measurements were performed. All devices were treated as a parallel plate capacitor during the measurements and performed at room temperature and in the dark condition [135]. Figure 6.32 shows the measured capacitance of the devices with and without QDs layer, at 1 kHz frequency as a function of the applied bias between -1 V and +1 V with constant oscillating amplitude of 50 mV for devices with and without QDs layer. The device capacitances increased in the forward bias direction for both samples. Meanwhile, the capacitance value of device with QDs layer was much more than the reference device as seen from Figure 6.32. The device capacitance can disintegrate into two distinct regions. At low bias region ($V < V_{bi}$), both devices behaved as a depletion layer modulated capacitance (C_{dep}) while at high bias region ($V>V_{bi}$) they behaved as a chemical capacitance (C_{μ}) [135].

The capacitance value of both devices at forward bias region remained almost constant. Whereas, capacitance value significantly increased with adding QDs layer inside IPSC. The specific range (0.3 V- 0.8 V) of applied bias voltage is given in Figure 6.32 because the lower values of bias voltage below 0.3 V were almost the same for both devices and for further increasing bias voltage over 0.8 V, the high capacitance value of QDs added device cannot be compared to the low capacitance value of reference device. The zero bias capacitance values of reference device and QDs added device changed in between 3.83 – 3.93 nF and 4.11 – 4.23 nF,

respectively. The increasing was observed in zero bias capacitance value with adding QDs layer.

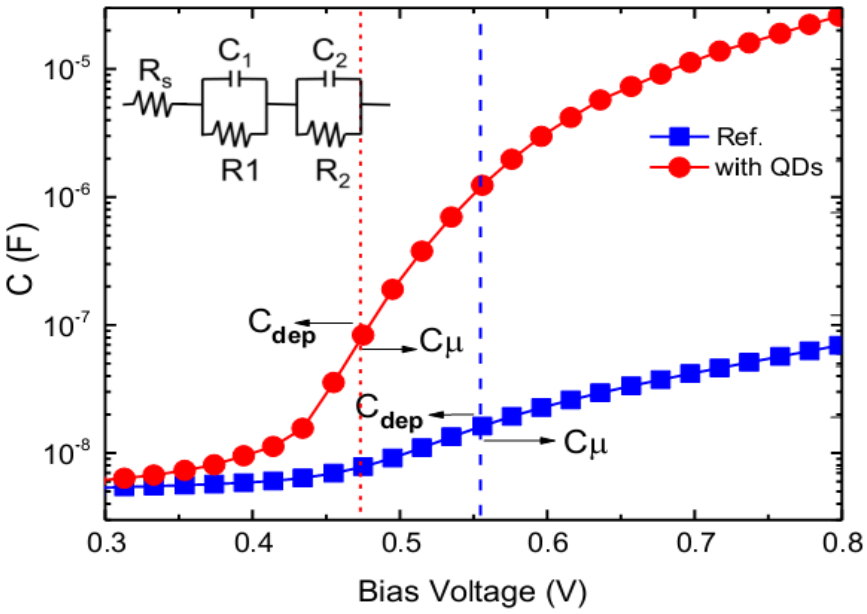

Figure 6.32 Capacitance densities versus voltage characteristics of IPSC for reference and with QDs layer in dark condition. Equivalent circuit was shown in the figure inset.

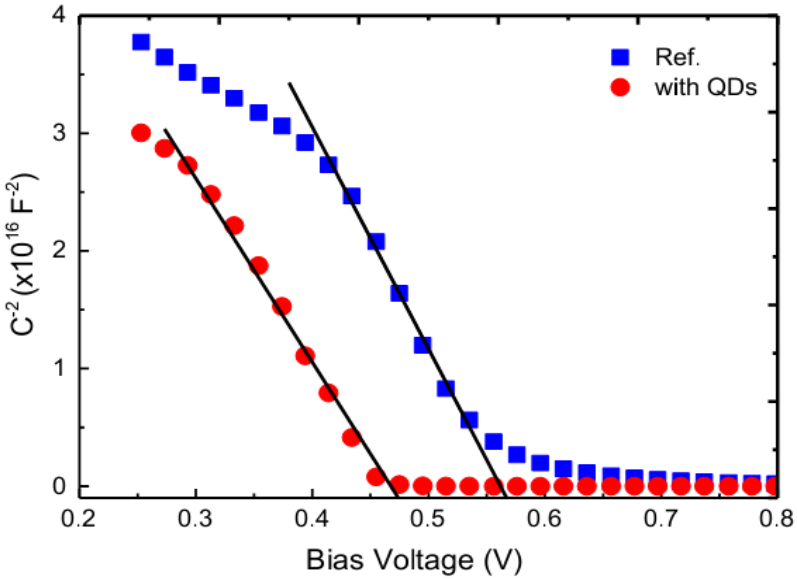

Figure 6.33 The Mott -Schottky curve for reference and with QDs layer devices derived from capacitance density versus voltage measurements.

Mott–Schottky curves obtained from the C-V measurements were represented in Figure 6.33. The built in voltage (V_{bi}) and acceptor consantration (N_A) of active polymer layer were calculated from Mott-Schottky plots. The values of V_{bi} and N_A were obtained as 0.47 V and $3.04x10^{17}$ cm^{-3} for reference device and 0.56 V and $3.67x10^{17}$ cm^{-3} for device with QDs layer, respectively. The relative improvement in acceptor concentration of IPSC was 21% with adding QDs layer as same improvement behavior of the PCE and R_S values as indicated above.

6.2.6 Impedance Spectroscopy of IPSC Devices with and without QDs layer

Impedance spectroscopy is a powerful method for characterization of the electrical properties of materials and their interfaces with electrodes. It can be used to investigate the dynamics of bound or mobile charge in the interfacial regions or bulk [171]. It was first introduced by Oliver Heaviside in the 1880s. Thereafter, vector diagrams and complex representation of impedance was developed by A. E. Kennelly and C. P. Steinmetz. The concept of impedance is more general than resistance since it involves phase differences. Impedance spectroscopy measurements can deduct carrier mobility and lifetime [135], [154]. Conventional plot of imaginary impedance with real impedance was experimentally resulted in semicircles for polymer solar cells [172].

The experimental electrical impedance in the complex plane for forward bias voltage 0.58 V and different oscillating frequency in between 40 Hz to 1 MHz was shown in Figure 6.34 for the devices with and without QDs layer. As clearly seen from Figure 6.34, the decrease in series resistance with the presence of the QDs layer was confirmed by impedance measurements. Carrier effective lifetimes were calculated by using recombination frequencies (f_0) which is corresponding frequency for the maximum in imaginary Z value [135], [154]. The carrier effective lifetimes were found as $8.32x10^{-5}$ s and $1.14x10^{-5}$ s for the devices without and with QDs layer, respectively. The carrier mobility values of the reference device and the one with QDs layer were also calculated by using the Nernst–Einstein relationship and found as $2.91x10^{-4}$ to $2.11x10^{-3}$ $cm^2V^{-1}s^{-1}$respectively [135], [154].

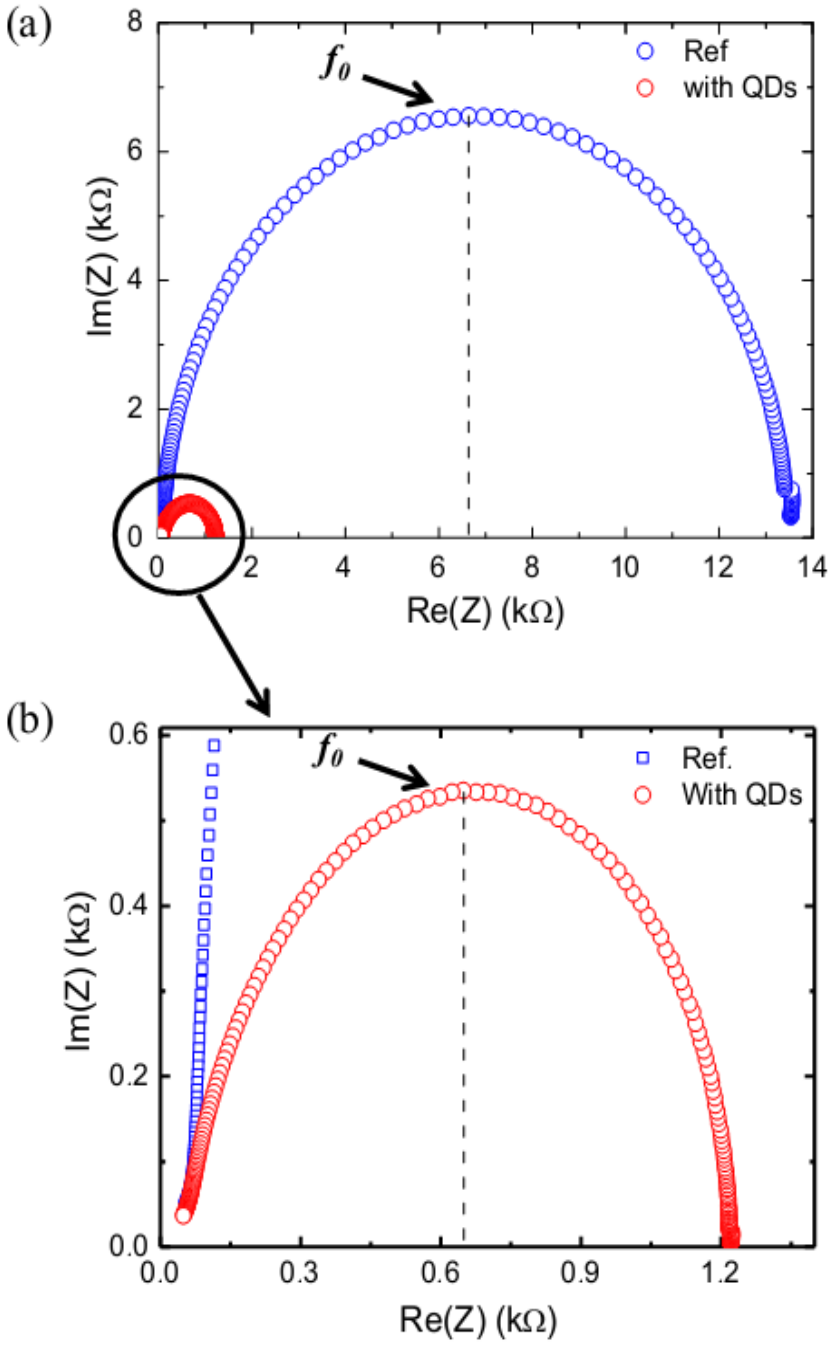

Figure 6.34 a) Impedance spectra of IPSC devices with and without QDs layer in dark. b) Impedance spectra of IPSC device with QDs layer at low impedance region.

CHAPTER 7

CONCLUSIONS

The main purpose of this work was to investigate the effects of quantum dots (QDs) thin film layer inside inorganic and organic based light converting devices and the possibility of improving the power conversion efficiency of solar cell devices beyond the Shockley-Queisser limit. The thesis has mainly two parts based on the studies of the solar cell devices and materials with the inorganic and organic semiconductor absorber layer. In the first part, the polycrystalline chalcopyrite $CuIn_{1-x}Ga_xSe_2$ (CIGS) thin films were used as an inorganic absorber semiconductor. In second part, a blend of Poly (3-hexylthiophene-2, 5-diyl) and poly (6, 6-phenyl C61-butyric acid methyl ester) (P3HT: PCBM) were studied as the organic semiconductor layers to cooperate with QDs thin film layer for the production of light converting devices. Lead sulfide quantum dots (PbS QDs) were used inside both device architectures because they have high photo sensitivity in the infrared (IR) region of electromagnetic spectrum and can be produced with the band gap values in between 0.7 and 2.1 eV.

CIGS thin film samples were thermally deposited onto soda lime glass and n-type Si wafer substrates by using Cu, InSe, GaSe and Se sources and the substrate temperature was kept at 300 ^{o}C during the deposition process. Post annealing treatment was applied to CIGS thin film samples at 350, 400 and 450 ^{o}C under nitrogen atmosphere for 30 minutes. The structural properties of CIGS thin films were examined by means of SEM, EDXA, XRD and Raman spectroscopy measurements. The optical properties of samples were carried out by using transmission and absorption measurements. Additionally, the electrical properties of CIGS and CIGS+QDs samples were studied by means of photo-conductivity and Hall Effect measurements.

The XRD pattern of CIGS samples was confirmed that the annealed sample at 450 ^{o}C was polycrystalline with a preferred orientation in the plane of (112) in the tetragonal structure. Raman spectra of CIGS thin films were measured at room temperature and the most intensive line was found at 180 cm^{-1} which is assigned to the strongest A_1 mode observed in the Raman spectra of chalcopyrite structure.

The atomic percentages of constituent elements (Cu, In, Ga and Se) of as-grown sample were found as 19%, 16%, 15%, and 50% from EDXA measurement, respectively. Cu atomic ratio was increased with annealing due to the indication of Se segregation or re-evaporation from the samples with the post annealing process. In and Ga ratios almost stayed the same during the heat treatment.

In order to investigate the effect of QDs on the thin film structure, CIGS thin film was coated with PbS QDs layer. After that, the confocal Raman spectroscopy measurements of CIGS thin film, PbS QDs thin film and CIGS thin film with QDs layer on it were performed at room temperature condition with 532 nm excitation laser sources. CIGS had the most intensive Raman peak at 180 cm^{-1} which is the A_1 mode of chalcopyrite structure. When CIGS thin film was coated with QDs layer, the effects of QDs on thin film were explicitly observed. The most intense peak of QDs coated sample was also at 180 cm^{-1}. However, assembling of both layers resulted in activation of B_1 mode of CIGS thin film. The Raman shift peak area the effected region of 78 cm^{-1} was also analyzed. The area under the peak increased from 25.8 to 54.2 cm^2 with coating QDs layer.

The absorption measurements of the CIGS thin film at room temperature indicated that room temperature values of the absorption coefficient were in between $1.7x10^3$ and $5.6x10^4$ cm^{-1} for the incident photon energies of 1.1 – 2.3 eV. The absorption spectra revealed the direct band gap of samples were around 1.30 eV, 1.62 eV and 1.68 eV for as grown and the annealed CIGS thin film samples at 350 and 450 ^{o}C for 30 minutes, respectively.

The photoconductivity measurements were performed as a function of illumination intensity in the temperature range of 100-350 K. Photocurrent associated with illumination intensity as $I_{ph} \alpha \Phi^n$, where power exponent n was calculated from the slope of Log (I_{ph}) vs. Log (Φ). The case of $n<1$, and $n>1$ correspond to “sublinear” and “supralinear” photoconductivities, respectively. For the CIGS thin film sample,

the n values calculated from the slope of Log (I_{ph}) vs. Log (Φ) and were found to be 0.63, 0.56, and 0,47 for 150, 250, and 350 K, respectively. The character of photocurrent for CIGS thin film sample was found as sublinear. Moreover, n values of QDs coated CIGS thin film sample were found as 1.48, 1.35, and 1.29 for 150, 250, and 350 K, respectively. These results indicated that the character of photocurrent for CIGS thin film sample was change with coating QDs layer from sublinear to supralinear. This change referred an increase in lifetime with photoexcitation intensity with existing of QDs layer.

The Hall Effect measurements were carried out for CIGS thin films without and with QDs layer. The room temperature hole concentration of the CIGS and CIGS+QDs thin films were calculated as $1.71x10^{18}$ and $6.12x10^{17}$ cm^{-3}, respectively. The Hall coefficient values were found as 3.64 and 10.21 cm^3/C for CIGS thin film without and with QDs layer, respectively. The resistivity value of sample decresed from $6.64x10^{-1}$ to $6.65x10^{-2}$ Ω.cm with coating QDs layer on the CIGS thin film. The mobility value of CIGS and CIGS+QDs was calculated as 9.56 to 15.81 $cm^2/(V.s)$, respectively. The sheet resistance of the samples was also calculated by software and found as $6.35x10^6$ and $1.08x10^8$ Ω/□ for CIGS and CIGS+QDs samples, respectively. The existing of QDs layer improved the electrical properties of samples.

In order to produce p-n heterojunction device structure, p-CIGS films were deposited on n-Si wafers with Ag back and In front contacts and Ag/n-Si/p-CIGS/In sandwich structure as a reference device was obtained. All deposited CIGS thin samples exhibited p-type conduction, defined by hot probe technique and Hall Effect measurements. The QDs layer was coated on Ag/n-Si/p-CIGS sample and In front contacts were coated on Ag/n-Si/p-CIGS/QDs to investigate effects of QDs layer on the device structure.

In order to investigate the rectifying behavior of the Ag/n-Si/p-CIGS/In and Ag/n-Si/p-CIGS/QDs/In devices, temperature dependent dark current-voltage measurements were carried out in temperature range of 220-360 K. The both devices showed very good device behavior with the rectification factor in between 5 and 3 orders of magnitude depending on temperature. The ideality factors were calculated in between 1.80 and 2.54 for reference device and in between 1.43 and 2.36 for the device with the QDs layer in the temperature range of 220-360 K. The series

resistances of both devices were calculated from the deviation of I-V slope from linearity as 121.5 $\Omega \cdot cm^2$ for reference device at the temperature of 220 K. However, the corresponding R_S value for the device with QDs layer was calculated as 18.46 $\Omega \cdot cm^2$. It was observed that the ambient temperature also affected the value of R_S value and it decreased with increasing temperature. The values of R_S were found as 22.7 $\Omega \cdot cm^2$ and 11.9 $\Omega \cdot cm^2$ for reference device and the device with QDs layer, at the temperature of 360 K, respectively. Therefore, the presence of the QDs layer resulted a device structure with lower with series resistance. The same behavior was observed for the shunt resistance (R_{Sh}) values.

The capacitance-voltage (C-V) measurements were also performed for the Ag/n-Si/p-CIGS/In and Ag/n-Si/p-CIGS/QDs/In hetero-structures for different frequencies at room temperature. The zero bias capacitance values of reference device and the device with QDs layer were measured in between 0.61 - 0.34 nF and 0.80 - 0.30 nF, respectively. The built in voltage (V_{bi}) and acceptor concentration (N_A) of both devices were calculated from Mott–Schottky curves by using C-V measurements. The values of V_{bi} and N_A were obtained as 1.13 V and $5.2x10^{15}$ cm^{-3} for reference device and 1.01 V and $7.1x10^{15}$ cm^{-3} for device with QDs layer, respectively.

In order to investigate the effects of QDs layer on power conversion efficiency (PCE) and other device parameters of the organic solar cells, the structure of inverted polymer solar cell (IPSC) was used as an organic light converting device. The ZnO buffer layer was coated on the half ITO coated glasses and the organic photoactive layer of P3HT: PCBM was coated on glass/ITO/ZnO substrates by using spin coating technique. Molybdenum trioxide (MoO_3 interface) layer and Ag front contact were deposited by thermal deposition technique and glass/ITO/ZnO/P3HT: PCBM/MoO_3/Ag IPCS structure as a reference device was obtained. In order to improve the PCE value of IPCS, PbS QDs layer was inserted in between ZnO buffer layer and active polymer layer by using spin coating technique and glass/ITO/ZnO/PbS QDs/P3HT: PCBM/MoO_3/Ag device structure was obtained. Additionally, the effect of the QDs layer thickness on the IPCS parameters was also investigated by changing the number of QDs layers.

The transmission and absorbance measurements of polymer and polymer+QDs layers confirmed that the main contribution of PbS QDs layer was in the near-IR region as theoretically expected.

The confocal Raman spectrum of polymer, QDs, and polymer + QDs thin film layers supported that some new Raman peaks emerged after coating QDs layer and it changed the structure. The Raman shift area calculation was also done for the most effected regions, namely 78 cm^{-1}, 557 cm^{-1}, and 1088 cm^{-1}. All affected regions increased in areas with adding QDs layer. The changing in the areas of Raman shift peaks were calculated from 11.8 to 38.1 cm^2 for peak at 78 cm^{-1}, 1.7 to 7.6 cm^2 for peak at 557 cm^{-1}, and 8.6 to 17.8 cm^2 for peak at 1088 cm^{-1}. These results are clear proof of the existence of QDs layer in the device architecture made same structural changes on the polymer active layer.

A typical set of forward and reverse bias I-V measurements with the applied voltage ranging from -1.5 V to +1.5 V at room temperature, both in dark and under 1.5AM global light were performed for the IPSC devices with and without QDs layer. In order to understand the effect of QDs amount in the IPSC structure, all other solar cell device layers were kept identical except the number of QDs thin film layers. The QD thin film layers were changed from 1 layer to 5 layers. The PCE and other device parameters were calculated from J-V curve and the PCE was found as 3.95±0.08% for the reference device and 4.58±0.06% for the device with 2 layers QDs film. The PCE value increased and reached the maximum value for 2 layers coated device. The PCE value of the devices decreased when the QDs layers more than 2, but still all the devices having QDs layers had higher PCE values than the reference device. The QDs thin film layer inside device structure improved the device performance relatively in between 5% to 16% when compared with reference IPCS device.

The parameters of reference IPSC device and the device with QDs layer were also calculated from J-V measurements. The series resistance (R_S) values were found as 6.74 Ω/cm^2 and 5.11 Ω/cm^2 for the reference and with 2 QDs layers coated devices, respectively. The relative improvement in R_S value was calculated as 24% for the most efficient device (2 layers QDs). The short circuit current (J_{SC}) of the reference and QDs layer inserted devices were calculated as 10.40 mA/cm^2 and 11.82 mA/cm^2, respectively. Therefore, QDs layer made device less resistance and improved the

carrier's mobility in structure due to the generation of electron-hole pairs with illumination of PbS QDs sensitizers and the faster recombination in the space charge region between ZnO and PbS QDs layer.

For further investigation of the effect of the presence of the QDs layer in IPSC, the EQE measurements were carried out and the maximim responces of EQEs were found as 61% and 55% fort he devices with and without QDs layer, respectively.The relative increase in EQE value was in between 12% and 22% in the range of 500 nm and 700 nm (visible region) and in between 3% and 12% in the range of 700 nm and 850 nm (near-IR region) after coating the QDs layer. Therefore, EQE results showed that the contribution of QDs thin film layer inside IPCS devices was not only in the near-IR but also in the visible range.

To further understand effect of QDs layer inside IPSC structure, capacitance-voltage (C-V) and impedance spectroscopy measurements were performed for devices with and without QDs layer. The device capacitances increased in the forward bias direction for both samples. The capacitance value increased 4 orders of magnitude with QDs layer. The zero bias capacitance values of reference device and QDs added device were compared and found as in between 3.83 – 3.93 nF and 4.11 – 4.23 nF, respectively. The small increasing was observed in zero bias capacitance value in QDs cooperated device.

The built in voltage (V_{bi}) and acceptor consantration (N_A) were calculeted from Mott-Schottky plots obtaned from C-V measurement. The values of V_{bi} and N_A were obtained as 0.47 V and 3.04×10^{17} cm^{-3} for reference device and 0.56 V and 3.67×10^{17} cm^{-3} for device with QDs layer, respectively. The experimental electrical impedance in the complex plane for forward bias voltage 0.58 V and different oscillating frequency in between 40 Hz to 1 MHz was carried out for devices with and without QDs layer. Carrier effective lifetimes were calculated by using recombination frequencies (f_0) which is corresponding frequency value for the maximum in imaginary Z value and they were found as 8.32×10^{-5} s and 1.14×10^{-5} s for reference and with QDs devices, respectively. The carrier mobility of reference and with QDs devices was also calculated by using the Nernst–Einstein relationship and they found as 2.91×10^{-4} to 2.11×10^{-3} $cm^2V^{-1}s^{-1}$ for reference and with QDs layer samples, respectively.

As a result it can be concluded that, placing QDs layer inside inorganic and organic solar cell devices the performance of both devices improved. The solar cell efficiency of the organic solar cell device enhanced mainly due to the collection of the extra photons having energies near IR region, the decrease in the series resistance and the increase in the carrier mobility values. The new approach for light converter devices is promising for further studies to increase the efficiency values. The QDs inside the solar cells architecture as a thin film layer is the new candidate and opportunity for efficiency increase of the solar cells. Structural, optical and electrical measurements of inorganic and organic devices have shown that the contribution of QDs as a thin film inside device structure deserves attention.

REFERENCES

[1] N. S. Lewis, "Toward cost-effective solar energy use," *Science*, vol. 315, pp. 798-801, 2007.

[2] E. A. Becquerel, "Recherches sur les effets de la radiation chimique de la lumiere solaire au moyen des courants electriques," *Comptes Rendus L´Academie des Sci.*, vol. 9, pp. 145–149, 1839.

[3] C. E. Fritts, "On a new form of selenium photocell," *Am. J. Sci.*, vol. 33, p. 97, 1883.

[4] L. L. Tobin, T. O'Reilly, D. Zerulla, and J. T. Sheridan, "Characterising dye-sensitised solar cells," *Opt. - Int. J. Light Electron Opt.*, vol. 122, pp. 1225–1230, 2011.

[5] R. S. Ohl, "Light-Sensitive Electric Device Including Silicon," 1948.

[6] D. M. Chapin, C. S. Fuller, and G. L. Pearson, "Solar Radiation into Electrical Power," *J. Appl. Phys.*, vol. 25, pp. 676–677, 1954.

[7] D. C. Reynolds, G. Leies, L. L. Antes, and R. E. Marburer, "Photovoltaic Effect in Cadmium Sulfide," *Phys. Rev.*, vol. 96, pp. 533–534, 1954.

[8] M. A. Green, "Photovoltaics: coming of age," *IEEE Conf. Photovolt. Spec.*, 1990.

[9] H. J. Queisser, "Detailed balance limit for solar cell efficiency," *Mater. Sci. Eng. B*, vol. 159–160, pp. 322–328, 2009.

[10] L. L. Kazmerski, F. R. White, and G. K. Morgan, "Thin-film $CuInSe_2$/CdS heterojunction solar cells," *Appl. Phys. Lett.*, vol. 29, pp. 268–270, 1976.

[11] P. Jackson, *et al*, "Properties of $Cu(In,Ga)Se_2$ solar cells with new record efficiencies up to 21.7%," *Phys. status solid-Rapid Res. Lett.*, vol. 9, pp. 28–31, 2015.

[12] I. Gur, N. A. Fromer, M. L. Geier, and A. P. Alivisatos, “Air-Stable All-Inorganic Nanocrystal Solar Cells Processed from Solution,” *Science*, vol. 310, pp. 462–465, 2005.

[13] K.-T. Lee, J. Y. Lee, S. Seo, and L. J. Guo, “Colored ultrathin hybrid photovoltaics with high quantum efficiency,” *Light Sci. Appl.*, vol. 3, p. 215, 2014.

[14] E. T. Yu and J. van de Lagemaat, “Photon management for photovoltaics,” *MRS Bull.*, vol. 36, pp. 424–428, 2011.

[15] J. Y. Kim, K. Lee, N. E. Coates, D. Moses, T.-Q. Nguyen, M. Dante, and A. J. Heeger, “Efficient Tandem Polymer Solar Cells Fabricated by All-Solution Processing,” *Science*, vol. 317, pp. 222–225, 2007.

[16] S. Sista, M.-H. Park, Z. Hong, Y. Wu, J. Hou, W. L. Kwan, G. Li, and Y. Yang, “Highly efficient tandem polymer photovoltaic cells.,” *Adv. Mater.*, vol. 22, pp. 380–383, 2010.

[17] G. Conibeer, “Third-generation photovoltaics,” *Mater. Today*, vol. 10, pp. 42–50, 2007.

[18] M. A. Green, “Third generation photovoltaics: Ultra-high conversion efficiency at low cost,” *Prog. Photovoltaics Res. Appl.*, vol. 9, pp. 123–135, 2001.

[19] J. J. Peterson and T. D. Krauss, “Photobrightening and photodarkening in PbS quantum dots,” *Phys. Chem. Chem. Phys.*, vol. 8, pp. 3851–3856, 2006.

[20] M. Yamaguchi, T. Takamoto, and K. Araki, “Super high-efficiency multi-junction and concentrator solar cells,” *Sol. Energy Mater. Sol. Cells*, vol. 90, pp. 3068–3077, 2006.

[21] G. Konstantatos and E. H. Sargent, “Nanostructured materials for photon detection,” *Nat. Nanotechnol.*, vol. 5, pp. 391–400, 2010.

[22] O. E. Semonin, J. M. Luther, S. Choi, H.-Y. Chen, J. Gao, A. J. Nozik, and M. C. Beard, “Peak External Photocurrent Quantum Efficiency Exceeding 100% via MEG in a Quantum Dot Solar Cell,” *Science*, vol. 334, pp. 1530–1533, 2011.

[23] E. Arici, N. S. Sariciftci, and D. Meissner, “Hybrid solar cells based on nanoparticles of $CuInS_2$ in organic matrices,” *Adv. Funct. Mater.*, vol. 13, pp. 165–170, 2003.

[24] W. J. E. Beek, M. M. Wienk, and R. A. J. Janssen, “Hybrid Solar Cells from Regioregular Polythiophene and ZnO Nanoparticles,” *Adv. Funct. Mater.*, vol. 16, pp. 1112–1116, 2006.

[25] S. Mokkapati, F. J. Beck, A. Polman, and K. R. Catchpole, “Designing periodic arrays of metal nanoparticles for light-trapping applications in solar cells,” *Appl. Phys. Lett.*, vol. 95, p. 053115, 2009.

[26] S. Pillai, K. R. Catchpole, T. Trupke, and M. A. Green, “Surface plasmon enhanced silicon solar cells,” *J. Appl. Phys.*, vol. 101, p. 093105, 2007.

[27] M. Law, L. E. Greene, J. C. Johnson, R. Saykally, and P. Yang, “Nanowire dye-sensitized solar cells,” *Nat. Mater.*, vol. 4, pp. 455–459, 2005.

[28] W. J. E. Beek, M. M. Wienk, and R. A. J. Janssen, “Efficient Hybrid Solar Cells from Zinc Oxide Nanoparticles and a Conjugated Polymer,” *Adv. Mater.*, vol. 16, pp. 1009–1013, 2004.

[29] H.-G. Im, S.-H. Jung, J. Jin, D. Lee, J. Lee, D. Lee, J.-Y. Lee, I.-D. Kim, and B.-S. Bae, “Flexible Transparent Conducting Hybrid Film Using a Surface-Embedded Copper Nanowire Network: A Highly Oxidation-Resistant Copper Nanowire Electrode for Flexible Optoelectronics,” *ACS Nano*, vol. 8, pp. 10973–10979, 2014.

[30] M. Danek, K. F. Jensen, C. B. Murray, and M. G. Bawendi, “Synthesis of luminescent thin-film CdSe/ZnSe quantum dot composites using CdSe quantum dots passivated with an overlayer of ZnSe,” *Chem. Mater.*, vol. 8, pp. 173–180, 1996.

[31] A. J. Nozik, “Quantum dot solar cells,” *Phys. E Low-dimensional Syst. Nanostructures*, vol. 14, pp. 115–120, 2002.

[32] C.-H. M. Chuang, P. R. Brown, V. Bulović, and M. G. Bawendi, “Improved performance and stability in quantum dot solar cells through band alignment engineering,” *Nat. Mater.*, vol. 13, pp. 796–801, 2014.

[33] G. H. Carey, L. Levina, R. Comin, O. Voznyy, and E. H. Sargent, “Record Charge Carrier Diffusion Length in Colloidal Quantum Dot Solids via Mutual Dot-To-Dot Surface Passivation,” *Adv. Mater.*, vol. 27, pp. 3325–3330, 2015.

[34] A. H. Ip, S. M. Thon, S. Hoogland, O. Voznyy, D. Zhitomirsky, R. Debnath, L. Levina, L. R. Rollny, G. H. Carey, A. Fischer, K. W. Kemp, I. J. Kramer, Z. Ning, A. J. Labelle, K. W. Chou, A. Amassian, and E. H. Sargent, “Hybrid passivated colloidal quantum dot solids,” *Nat. Nanotechnol.*, vol. 7, pp. 577–582, 2012.

[35] N. Zhao, T. P. Osedach, L.-Y. Chang, S. M. Geyer, D. Wanger, M. T. Binda, A. C. Arango, M. G. Bawendi, and V. Bulovic, “Colloidal PbS quantum dot solar cells with high fill factor.,” *ACS Nano*, vol. 4, pp. 3743–3752, 2010.

[36] Y. L. Lee and Y. S. Lo, “Highly efficient quantum-dot-sensitized solar cell based on co-sensitization of CdS/CdSe,” *Adv. Funct. Mater.*, vol. 19, pp. 604–609, 2009.

[37] Z. Ning, H. Tian, C. Yuan, Y. Fu, H. Qin, L. Sun, and H. Ågren, “Solar cells sensitized with type-II ZnSe–CdS core/shell colloidal quantum dots,” *Chem. Commun.*, vol. 47, pp. 1536–1538, 2011.

[38] S. Kim, B. Fisher, H.-J. Eisler, and M. Bawendi, “Type-II Quantum Dots : CdTe / CdSe (Core / Shell) and CdSe / ZnTe (Core / Shell) Heterostructures,” *J. Am. Chem. Soc.*, vol. 125, pp. 11466–11467, 2003.

[39] L. Yang, C. McCue, Q. Zhang, E. Uchaker, Y. Mai, and G. Cao, “Highly efficient quantum dot-sensitized TiO_2 solar cells based on multilayered semiconductors (ZnSe/CdS/CdSe),” *Nanoscale*, vol. 7, pp. 3173–3180, 2015.

[40] P. Hoyer and R. Könenkamp, “Photoconduction in porous TiO_2 sensitized by PbS quantum dots,” *Appl. Phys. Lett.*, vol. 66, pp. 349–351, 1995.

[41] J. a. Smyder and T. D. Krauss, “Coming attractions for semiconductor quantum dots,” *Mater. Today*, vol. 14, pp. 382–387, 2011.

[42] P. R. Brown, D. Kim, R. R. Lunt, N. Zhao, M. G. Bawendi, J. C. Grossman, and V. Bulovi, “Energy Level Modification in Lead Sulfide Quantum Dot Thin Films through Ligand Exchange,” *ACS Nano*, vol. 8, pp. 5863–5872, 2014.

[43] P. Y. Yu and M. Cardona, *Fundamentals of Semiconductors - Physics and Materials Properties*. Berlin: Springer, 1996.

[44] H. Huang and J. Huang, *Organic and Hybrid Solar Cells*. Switzerland: Springer International Publishing, 2014.

[45] W. Tress, *Organic Solar Cells*, Switzerland: Springer International Publishing, 2014.

[46] W. Shockley, "The Theory of p-n Junctions in Semiconductors and p-n Junction Transistors," *Bell Syst. Tech. J.*, pp. 435–489, 1948.

[47] S. M. Sze and K. K. NG., *Physics of Semiconductor Devices*, 3rd. ed. New Jersey: Wiley, 2007.

[48] J. Nelson, *The Physics of Solar Cells*. London: Imperial College Press, 2003.

[49] I. V Bodnar, G. F. Smirnova, T. V Smirnova, Y. A. Aleshchenko, and L. K. Vodopyanov, "Lattice Vibrations of $CuGaSe_2$, $CuInSe_2$ Ternary Compounds and $CuGa_xIn_{1-x}Se_2$ Solid Solutions," *Phys. Stat. Sol.*, vol. 145, pp. 117–122, 1988.

[50] J. Jaffe and A. Zunger, "Electronic structure of the ternary chalcopyrite semiconductors $CuAlS_2$, $CuGaS_2$, $CuInS_2$, $CuAlSe_2$, $CuGaSe_2$, and $CuInSe_2$," *Phys. Rev. B*, vol. 28, pp. 5822–5847, 1983.

[51] A. N. Y. Samaan, R. Vaidhyanathan, R. Noufi, R. D. Tomlinson, S. Cells, C. Boulevard, and E. Engineering, "Growth and characterization of polycrystalline $CuInSe_2$ thin films," *Sol. Cells*, vol. 16, pp. 181–198, 1986.

[52] M. I. Alonso, M. Garriga, C. A. Durante Rincón, E. Hernández, and M. León, "Optical functions of chalcopyrite $CuGa_xIn_{1-x}Se_2$ alloys," *Appl. Phys. A Mater. Sci. Process.*, vol. 74, pp. 659–664, 2002.

[53] S. B. Zhang, S.-H. Wei, A. Zunger, and H. Katayama-Yoshida, "Defect physics of the $CuInSe_2$ chalcopyrite semiconductor," *Phys. Rev. B*, vol. 57, pp. 9642–9656, 1998.

[54] J. R. Tuttle, D. S. Albin, J. P. Goral, and R. Noufi, "Secondary and polymorphic phase behavior of thin film $CuInSe_2$: ramifications on the device performance," in *IEEE Conference on Photovoltaic Specialists*, vol. 53, pp.

748–754,1989.

[55] F. Kessler and D. Rudmann, “Technological aspects of flexible CIGS solar cells and modules,” *Sol. Energy*, vol. 77, pp. 685–695, 2004.

[56] G. Makrides, B. Zinsser, M. Norton, G. E. Georghiou, M. Schubert, and J. H. Werner, “Potential of photovoltaic systems in countries with high solar irradiation,” *Renew. Sustain. Energy Rev.*, vol. 14, pp. 754–762, 2010.

[57] B. J. Stanbery, “Copper Indium Selenides and Related Materials for Photovoltaic Devices,” *Crit. Rev. Solid State Mater. Sci.*, vol. 27, pp. 73–117, 2002.

[58] O. Lundberg, M. Edoff, and L. Stolt, “The effect of Ga-grading in CIGS thin film solar cells,” *Thin Solid Films*, vol. 480–481, pp. 520–525, 2005.

[59] M. Gloeckler and J. R. Sites, “Band-gap grading in Cu(In,Ga)Se_2 solar cells,” *J. Phys. Chem. Solids*, vol. 66, pp. 1891–1894, 2005.

[60] T. Dullweber, G. Hanna, U. Rau, and H. W. Schock, “A new approach to high-efficiency solar cells by band gap grading in Cu(In,Ga)Se_2 chalcopyrite semiconductors,” *Sol. Energy Mater. Sol. Cells*, vol. 67, pp. 145–150, 2001.

[61] S. H. Wei, S. B. Zhang, and A. Zunger, “Effects of Ga addition to $CuInSe_2$ on its electronic, structural, and defect properties,” *Appl. Phys. Lett.*, vol. 72, pp. 3199–3201, 1998.

[62] D. S. Albin, J. R. Tuttle, G. D. Mooney, J. J. Carapella, A. Duda, A. Mason, and R. Noufi, “A study on the optical and microstructural characteristics of quaternary Cu(In,Ga)Se_2 polycrystalline thin films,” in *IEEE Conference on Photovoltaic Specialists*, pp. 562–569, 1990.

[63] T. Wada, N. Kohara, T. Negami, and M. Nishitani, “Chemical and Structural Characterization of Cu(In ,Ga)Se_2 /Mo Interface in Solar Cells Cu(In,Ga)Se_2,” *Jpn. J. Appl. Phys.*, vol. 35, pp. 1253–1256, 1996.

[64] M. Bär, S. Nishiwaki, L. Weinhardt, S. Pookpanratana, W. N. Shafarman, and C. Heske, “Electronic level alignment at the deeply buried absorber/Mo interface in chalcopyrite-based thin film solar cells,” *Appl. Phys. Lett.*, vol. 93, p. 042110, 2008.

[65] J. H. Scofield, A. Duda, D. Albin, B. L. Ballard, and P. K. Predecki, “Sputtered molybdenum bilayer back contact for copper indium diselenide-based polycrystalline thin-film solar cells,” *Thin Solid Films*, vol. 260, pp. 26–31, 1995.

[66] M. A. Contreras, B. Egaas, K. Ramanathan, J. Hiltner, A. Swartzlander, F. Hasoon, and R. Noufi, “Progress Toward 20% Efficiency in Cu(In,Ga)Se_2 Polycrystalline Thin-film Solar Cells,” *Prog. Photovoltaics Res. Appl.*, vol. 7, pp. 311–316, 1999.

[67] A. Chirilă, S. Buecheler, F. Pianezzi, P. Bloesch, C. Gretener, A. R. Uhl, C. Fella, L. Kranz, J. Perrenoud, S. Seyrling, R. Verma, S. Nishiwaki, Y. E. Romanyuk, G. Bilger, and A. N. Tiwari, “Highly efficient Cu(In,Ga)Se_2 solar cells grown on flexible polymer films.,” *Nat. Mater.*, vol. 10, pp. 857–861, 2011.

[68] O. A. A. Ekimov A. I., “Quantum size effect in three-dimensional microscopic semiconductor crystals,” *JETP Lett.*, vol. 34, pp. 345 – 348, 1981.

[69] A. Tartakovskii, *Quantum Dots*. Cambridge: Cambridge University Press, 2012.

[70] V. I. Klimov, *Nanocrystal Quantum Dots*, 2nd ed. Florida, USA: CRC Press, 2010.

[71] J. Wu, S. Chen, A. Seeds, and H. Liu, “Quantum dot optoelectronic devices: lasers, photodetectors and solar cells,” *J. Phys. D. Appl. Phys.*, vol. 48, p. 363001, 2015.

[72] L. Brus, “Electronic wave functions in semiconductor clusters: experiment and theory,” *J. Phys. Chem.*, vol. 90, pp. 2555–2560, 1986.

[73] D. Vanmaekelbergh and P. Liljeroth, “Electron-conducting quantum dot solids: novel materials based on colloidal semiconductor nanocrystals.,” *Chem. Soc. Rev.*, vol. 34, pp. 299–312, 2005.

[74] A. J. Nozik, “Spectroscopy and Hot Electron Relaxation Dynamics in Semiconductor Quantum Well and Quantum Dots,” *Annu. Rev. Phys. Chem.*, vol. 52, pp. 193–231, 2001.

[75] Sigma-Aldrich, “Quantum Dots.” Online Available: http://www.sigmaaldrich.com/content/dam/sigma-aldrich/materials-science/nanomaterials/quantum-confinement-effect.jpg. (last accessed on February 3, 2016.)

[76] V. V. Mitin, V. A. Kochelap, and M. A. Stroscio, *Introduction to Nanoelectronics*. Cambridge University Press, 2008.

[77] M. Kuno, *Introductory Nanoscience: Physical and Chemical Concepts*. New York: Garland Science, Taylor & Francis Group, LLC, 2012.

[78] T. Trupke, M. a. Green, and P. Würfel, “Improving solar cell efficiencies by up-conversion of sub-band-gap light,” *J. Appl. Phys.*, vol. 92, pp. 4117–4122, 2002.

[79] A. Shalav, B. S. Richards, and M. A. Green, “Luminescent layers for enhanced silicon solar cell performance: Down-conversion,” *Sol. Energy Mater. Sol. Cells*, vol. 91, pp. 829–842, 2007.

[80] B. S. Richards, “Luminescent layers for enhanced silicon solar cell performance: Down-conversion,” *Sol. Energy Mater. Sol. Cells*, vol. 90, pp. 1189–1207, 2006.

[81] N. Bloembergen, “Solid State Infrared Quantum Counters,” *Phys. Rev. Lett.*, vol. 2, pp. 84–85, 1959.

[82] F. Auzel, “Upconversion processes in coupled ion systems,” *J. Lumin.*, vol. 45, pp. 341–345, 1990.

[83] V. V. Ovsyankin and P. P. Feofilov, “Cooperative Sensitization of Luminescence in Crystals Activated with Rare Earth Ions,” *Sov. Phys. JETP Lett.*, vol. 4, p. 317, 1966.

[84] L. Y. Ang, M. E. Lim, L. C. Ong, and Y. Zhang, “Applications of upconversion nanoparticles in imaging, detection and therapy,” *Nanomedicine*, vol. 6, pp. 1273–1288, 2011.

[85] H.-Q. Wang, M. Batentschuk, A. Osvet, L. Pinna, and C. J. Brabec, “Rare-Earth Ion Doped Up-Conversion Materials for Photovoltaic Applications,” *Adv. Mater.*, vol. 23, pp. 2675–2680, 2011.

[86] B. S. Richards and A. Shalav, “Enhancing the Near Infrared Spectral Response of Silicon Opto-Electronic Devices,” *IEEE Trans. Electron Devices*, vol. 54, pp. 2679–2684, 2007.

[87] Z. Huang, X. Li, M. Mahboub, K. M. Hanson, V. M. Nichols, H. Le, M. L. Tang, and C. J. Bardeen, “Hybrid Molecule–Nanocrystal Photon Upconversion Across the Visible and Near-Infrared,” *Nano Lett.*, vol. 15, pp. 5552–5557, 2015.

[88] M. C. Beard and R. J. Ellingson, “Multiple exciton generation in semiconductor nanocrystals: Toward efficient solar energy conversion,” *Laser Photonics Rev.*, vol. 2, pp. 377–399, 2008.

[89] W. Shockley and H. J. Queisser, “Detailed Balance Limit of Efficiency of p-n Junction Solar Cells,” *J. Appl. Phys.*, vol. 32, p. 510, 1961.

[90] C. Smith and D. Binks, “Multiple exciton generation in Colloidal nanocrystals,” *Nanomaterials*, vol. 4, pp. 19–45, 2014.

[91] S. Kolodinski, J. H. Werner, T. Wittchen, and H. J. Queisser, “Quantum efficiencies exceeding unity due to impact ionization in silicon solar cells,” *Appl. Phys. Lett.*, vol. 63, pp. 2405–2407, 1993.

[92] J. Bude and K. Hess, “Thresholds of impact ionization in semiconductors,” *J. Appl. Phys.*, vol. 72, pp. 3554–3561, 1992.

[93] H. K. Jung, K. Taniguchi, and C. Hamaguchi, “Impact ionization model for full band Monte Carlo simulation in GaAs,” *J. Appl. Phys.*, vol. 79, pp. 2473–2480, 1996.

[94] D. Harrison, R. A. Abram, and S. Brand, “Characteristics of impact ionization rates in direct and indirect gap semiconductors.,” vol. 85, pp. 8186–8192, 1999.

[95] A. J. Nozik, “Multiple exciton generation in semiconductor quantum dots,” *Chem. Lett. Lett.*, vol. 457, pp. 3–11, 2008.

[96] A. K. K. Kyaw, X. W. Sun, C. Y. Jiang, G. Q. Lo, D. W. Zhao, and D. L. Kwong, “An inverted organic solar cell employing a sol-gel derived ZnO electron selective layer and thermal evaporated MoO_3 hole selective layer,”

Appl. Phys. Lett., vol. 93, p. 221107, 2008.

[97] S. M. George, B. Yoon, and A. a Dameron, "Surface chemistry for molecular layer deposition of organic and hybrid organic-inorganic polymers," *Acc. Chem. Res.*, vol. 42, pp. 498–508, 2009.

[98] D. Vak, S.-S. Kim, J. Jo, S.-H. Oh, S.-I. Na, J. Kim, and D.-Y. Kim, "Fabrication of organic bulk heterojunction solar cells by a spray deposition method for low-cost power generation," *Appl. Phys. Lett.*, vol. 91, p. 081102, 2007.

[99] T. R. Hebner, C. C. Wu, D. Marcy, M. H. Lu, and J. C. Sturm, "Ink-jet printing of doped polymers for organic light emitting devices," *Appl. Phys. Lett.*, vol. 72, pp. 519–521, 1998.

[100] W. C. H. Choy, *Organic Solar Cells : Materials and Device Physics*. Verlag-London: Springer, 2013.

[101] A. M. Bagher, "Introduction to Organic Solar Cells," *Sustain. Energy*, vol. 2, pp. 85–90, 2014.

[102] H. Sirringhaus, P. J. Brown, R. H. Friend, M. M. Nielsen, K. Bechgaard, B. M. W. Langeveld-Voss, A. J. H. Spiering, R. A. J. Janssen, E. W. Meijer, P. Herwig, and D. M. de Leeuw, "Two-dimensional charge transport in self-organized, high-mobility conjugated polymers," *Nature*, vol. 401, pp. 685–688, 1999.

[103] S. Günes, H. Neugebauer, and N. S. Sariciftci, "Conjugated polymer-based organic solar cells.," *Chem. Rev.*, vol. 107, pp. 1324–38, 2007.

[104] M. A. Green, *Solar cells: operating principles, technology, and system applications*. Englewood Cliffs, NJ: Prentice-Hall, Inc., 1982.

[105] C. Richter, D. Lincot, and C. A. Gueymard, Eds., *Solar Energy*. New York: Springer, 2012.

[106] A. Haugeneder, M. Neges, C. Kallinger, W. Spirkl, U. Lemmer, J. Feldmann, U. Scherf, E. Harth, A. Gügel, and K. Müllen, "Exciton diffusion and dissociation in conjugated polymer/fullerene blends and heterostructures," *Phys. Rev. B*, vol. 59, pp. 15346–15351, 1999.

[107] J. J. M. Halls, K. Pichler, R. H. Friend, S. C. Moratti, and A. B. Holmes, “Exciton diffusion and dissociation in a poly(p-phenylenevinylene)/C60 heterojunction photovoltaic cell,” *Appl. Phys. Lett.*, vol. 68, p. 3120, 1996.

[108] C. W. Tang, S. a. Vanslyke, and C. H. Chen, “Electroluminescence of doped organic thin films,” *J. Appl. Phys.*, vol. 65, pp. 3610–3616, 1989.

[109] G. Yu, J. Gao, J. C. Hummelen, and A. J. Heeger, “Polymer photovoltaic cells: enhanced efficiencies via a network of internal donor-acceptor heterojunctions,” *Science*, vol. 270, pp. 1789–1791, 1995.

[110] Z. Lin and J. Wang, Eds., *Low-cost Nanomaterials*. Verlag-London: Springer, 2014.

[111] M. Jørgensen, K. Norrman, and F. C. Krebs, “Stability/degradation of polymer solar cells,” *Sol. Energy Mater. Sol. Cells*, vol. 92, pp. 686–714, 2008.

[112] T. Shirakawa, T. Umeda, Y. Hashimoto, A. Fujii, and K. Yoshino, “Effect of ZnO layer on characteristics of conducting polymer/C60 photovoltaic cell,” *J. Phys. D. Appl. Phys.*, vol. 37, pp. 847–850, 2004.

[113] M. Al-ibrahim, S. Sensfuss, and J. Uziel, “Comparison of normal and inverse poly (3- hexylthiophene)/ fullerene solar cell architectures,” *Sol. Energy Mater. Sol. Cells*, vol. 85, pp. 277–283, 2005.

[114] D. Fichou, *Handbook of Oligo- and Polythiophene*. New York: Wiley, 1999.

[115] J. Li, F. Dierschke, J. Wu, A. C. Grimsdale, and K. Müllen, “Poly(2,7-carbazole) and perylene tetracarboxydiimide: a promising donor/acceptor pair for polymer solar cells,” *J. Mater. Chem.*, vol. 16, pp. 96–100, 2006.

[116] J. C. Nolasco, R. Cabré, J. Ferré-Borrull, L. F. Marsal, M. Estrada, and J. Pallarès, “Extraction of poly (3-hexylthiophene) (P3HT) properties from dark current voltage characteristics in a P3HT/n-crystalline-silicon solar cell,” *J. Appl. Phys.*, vol. 107, p. 044505, 2010.

[117] S. a. Choulis, Y. Kim, J. Nelson, D. D. C. Bradley, M. Giles, M. Shkunov, and I. McCulloch, “High ambipolar and balanced carrier mobility in regioregular poly(3-hexylthiophene),” *Appl. Phys. Lett.*, vol. 85, pp. 3890–3892, 2004.

[118] G. J. Matt, S. Gu, T. B. Singh, and N. Marjanovic, “High-mobility n -channel

organic field-effect transistors based on epitaxially grown C60 films," *Org. Electron.*, vol. 6, pp. 105–110, 2005.

[119] C. Waldauf, P. Schilinsky, M. Perisutti, J. Hauch, and C. J. Brabec, "Solution-Processed Organic n-Type Thin-Film Transistors," *Adv. Mater.*, vol. 15, pp. 2084–2088, 2003.

[120] S. H. Yoo, J. M. Kum, and S. O. Cho, "Tuning the electronic band structure of PCBM by electron irradiation.," *Nanoscale Res. Lett.*, vol. 6, p. 545, 2011.

[121] K. Yoshida, T. Oku, A. Suzuki, T. Akiyama, and Y. Yamasaki, "Fabrication and Characterization of PCBM : P3HT Bulk Heterojunction Solar Cells Doped with Germanium Phthalocyanine or Germanium Naphthalocyanine," *Mater. Sci. Appl.*, vol. 4, pp. 1–5, 2013.

[122] F. Matteucci, M. Dondi, and G. Guarini, "Effect of soda-lime glass on sintering and technological properties of porcelain stoneware tiles," *Ceram. Int.*, vol. 28, pp. 873–880, 2002.

[123] W. a. Lanford, K. Davis, P. Lamarche, T. Laursen, R. Groleau, and R. H. Doremus, "Hydration of soda-lime glass," *J. Non. Cryst. Solids*, vol. 33, pp. 249–266, 1979.

[124] A. Luque and S. Hegedus, *Handbook of Photovoltaic Science and Engineering*, 2nd. ed. Sussex: John Wiley & Sons, Inc., 2003.

[125] D. M. Mattox, *Handbook of Physical Vapor Deposition (PVD) Processing: Film Formation, Adhesion, Surface Preparation and Contamination Control*. New Jersey: Noyes Publications, 1998.

[126] A. L. Patterson, "The Scherrer Formula for X-Ray Particle Size Determination," *Phys. Rev.*, vol. 56, pp. 978–982, 1939.

[127] J. R. Ferraro, K. Nakamoto, and C. W. Brown, *Introductory Raman Spectroscopy*. San Diego, California: Elsevier Academic Press, 2003.

[128] W. H. Weber and R. Merlin, *Raman Scattering in Material Science*. Heidelberg, Berlin: Springer-Verlag, 2000.

[129] G. Turrell and J. Corset, *Raman Microscopy: Developments and Applications*. San Diego, California: Elsevier Academic Press, 1996.

[130] E. H. Hall, “On a new Action of the Magnet on Electric Currents,” *Am. J. Math.*, vol. 2, pp. 287–292, 1879.

[131] İ. Candan, “Growth and Characterization of $CuIn_{1-x}Ga_xSe_2$ Thin Film for Solar Cell Structures,” Ms. Thesis in Physics Department of Middle East Technical University, 2009.

[132] K. Yılmaz, “Investigation of InSe Thin Film Based Devices,” PhD Thesis in Physics Department of Middle East Technical University, 2004.

[133] S. R. Wenham, M. A. Green, M. E. Watt, and R. Corkish, *Applied Photovoltaics*, 2nd. ed. London: Earthscan, 2007.

[134] E. V. M. Papadopoulou, *Photovoltaic Industrial Systems : An Environmental Approach*. Heidelberg, Berlin: Springer-Verlag, 2011.

[135] J. Bisquert, F. Fabregat-santiago, I. Mora-Seró, G. Garcia-Belmonte, and S. Gimenez, “Electron Lifetime in Dye-Sensitized Solar Cells: Theory and interpritation of Measurements,” *J. Phys. Chem. C*, vol. 113, pp. 17278–17290, 2009.

[136] A. M. Hermann, M. Mansour, V. Badri, B. Pinkhasov, C. Gonzales, F. Fickett, M. E. Calixto, P. J. Sebastian, C. H. Marshall, and T. J. Gillespie, “Deposition of smooth $Cu(In,Ga)Se_2$ films from binary multilayers,” *Thin Solid Films*, vol. 361, pp. 74–78, 2000.

[137] I. Martil, J. Santamaria, E. Iborra, G. Gonzalez-Diaz, and F. Sanchez-Quesada, “CuInSe2 thin films produced by rf sputtering in Ar/H_2 atmospheres,” *J. Appl. Phys.*, vol. 62, p. 4163, 1987.

[138] J. I. Langford and A. J. C. Wilson, “Scherrer after sixty years: A survey and some new results in the determination of crystallite size,” *J. Appl. Crystallogr.*, vol. 11, pp. 102–113, 1978.

[139] S. Roy, P. Guha, S. Kundu, H. Hanazawq, S. Chaudhuri, and A. Pal, “Characterization of $Cu(In,Ga)Se_2$ films by Raman scattering,” *Mater. Chem. Phys.*, vol. 73, pp. 24–30, 2002.

[140] I. H. Choi, “Raman spectroscopy of $CuIn_{1-x}Ga_xSe_2$ for in-situ monitoring of the composition ratio,” *Thin Solid Films*, vol. 519, pp. 4390–4393, 2011.

[141] C. Rincón and F. J. Ramírez, "Lattice vibrations of $CuInSe_2$ and $CuGaSe_2$ by Raman microspectrometry," *J. Appl. Phys.*, vol. 72, pp. 4321–4324, 1992.

[142] D. Albin, R. Noufi, J. Tuttle, J. Goral, and S. H. Risbud, "Composition-structure relationships for multisource evaporated $CuGaSe_2$ thin films," *J. Appl. Phys.*, vol. 64, pp. 4903–4908, 1988.

[143] H. Miyazaki, R. Mikami, A. Yamada, and M. Konagai, "$Cu(InGa)Se_2$ thin film absorber with high Ga contents and its application to the solar cells," *J. Phys. Chem. Solids*, vol. 64, pp. 2055–2058, 2003.

[144] C. De Blasi, D. Manno, G. Micocci, and A. Tepore, "Optical absorption and structure of thermally annealed gallium selenide thin films," *J. Appl. Phys.*, vol. 65, pp. 1164 –1167, 1989.

[145] J. Touc, *Amorphous and Liquid Semiconductors*. New York: Springer, 1974.

[146] J. I. Pankove, *Optical Processes in Semiconductors*. New York: Dover Publications Inc., 1971.

[147] B. Thomas and T. R. N. Kutty, "Formation of Single-Phase Indium Selenide Thin Films by Elemental Evaporation," *Phys. Status Solidi*, vol. 119, pp. 127–138, 1990.

[148] C. Julien, N. Benramdane, and J. P. Guesdon, "Transformation steps of structure in flash-deposited films of a-InSe," *Semicond. Sci. Technol.*, vol. 5, pp. 905–910, 1990.

[149] I. Introduction, "Transport mechanisms in ZnO/CdS/$CulnSe_2$ solar cells," vol. 94305, pp. 4694–4699, 1990.

[150] S. Majumdar, S. Chattopadhyay, and P. Banerji, "Electrical characterization of p-ZnO/p-Si heterojunction," *Appl. Surf. Sci.*, vol. 255, pp. 6141–6144, 2009.

[151] H. Uslu, A. Bengi, S. Ş. Çetin, U. Aydemir, S. Altindal, S. T. Aghaliyeva, and S. Özçelik, "Temperature and voltage dependent current-transport mechanisms in GaAs/AlGaAs single-quantum-well lasers," *J. Alloys Compd.*, vol. 507, pp. 190–195, 2010.

[152] K. S. Karimov, M. M. Ahmed, S. A. Moiz, and M. I. Fedorov, "Temperature-dependent properties of organic-on-inorganic Ag/p-CuPc/n-GaAs/Ag

photoelectric cell," *Sol. Energy Mater. Sol. Cells*, vol. 87, pp. 61–75, 2005.

[153] E. Coşkun, H. H. Güllü, İ. Candan, Ö. Bayraklı, M. Parlak, and Ç. Erçelebi, "Device behavior of an In/p-Ag(Ga,In)Te_2/n-Si/Ag heterojunction diode," *Mater. Sci. Semicond. Process.*, vol. 34, pp. 138–145, 2015.

[154] G. Garcia-Belmonte, P. P. Boix, J. Bisquert, M. Sessolo, and H. J. Bolink, "Simultaneous determination of carrier lifetime and electron density-of-states in P3HT:PCBM organic solar cells under illumination by impedance spectroscopy," *Sol. Energy Mater. Sol. Cells*, vol. 94, pp. 366–375, 2010.

[155] V. Janardhanam, H. K. Lee, K. H. Shim, H. B. Hong, S. H. Lee, K. S. Ahn, and C. J. Choi, "Temperature dependency and carrier transport mechanisms of Ti/p-type InP Schottky rectifiers," *J. Alloys Compd.*, vol. 504, pp. 146–150, 2010.

[156] M. Shao, J. Keum, J. Chen, Y. He, W. Chen, J. F. Browning, J. Jakowski, B. G. Sumpter, I. N. Ivanov, Y.-Z. Ma, C. M. Rouleau, S. C. Smith, D. B. Geohegan, K. Hong, and K. Xiao, "The isotopic effects of deuteration on optoelectronic properties of conducting polymers," *Nat. Commun.*, vol. 5, pp. 1–11, 2014.

[157] Y. Lee, S. H. Lee, K. Kim, J. W. Lee, K.-Y. Han, J. Kim, and J. Joo, "Single nanoparticle of organic p-type and n-type hybrid materials: nanoscale phase separation and photovoltaic effect," *J. Mater. Chem.*, vol. 22, pp. 2485–2490, 2012.

[158] E. Klimov, W. Li, X. Yang, G. G. Hoffmann, and J. Loos, "Scanning near-field and confocal Raman microscopic investigation of P3HT-PCBM systems for solar cell applications," *Macromolecules*, vol. 39, pp. 4493–4496, 2006.

[159] G. Louarn, M. Trznadel, J. P. Buisson, J. Laska, A. Pron, M. Lapkowski, and S. Lefrant, "Raman Spectroscopic Studies of Regioregular Poly(3-alkylthiophenes)," *J. Phys. Chem.*, vol. 100, pp. 12532–12539, 1996.

[160] X. Wang, D. Zhang, K. Braun, H.-J. Egelhaaf, C. J. Brabec, and A. J. Meixner, "High-Resolution Spectroscopic Mapping of the Chemical Contrast from Nanometer Domains in P3HT:PCBM Organic Blend Films for Solar-Cell Applications," *Adv. Funct. Mater.*, vol. 20, pp. 492–499, 2010.

[161] S. Falke, P. Eravuchira, A. Materny, and C. Lienau, “Raman spectroscopic identification of fullerene inclusions in polymer/fullerene blends,” *J. Raman Spectrosc.*, vol. 42, pp. 1897–1900, 2011.

[162] W. C. Tsoi, D. T. James, J. S. Kim, P. G. Nicholson, C. E. Murphy, D. D. C. Bradley, J. Nelson, and J. S. Kim, “The nature of in-plane skeleton Raman modes of P3HT and their correlation to the degree of molecular order in P3HT:PCBM blend thin films,” *J. Am. Chem. Soc.*, vol. 133, pp. 9834–9843, 2011.

[163] S. Miller, G. Fanchini, Y.-Y. Lin, C. Li, C.-W. Chen, W.-F. Su, and M. Chhowalla, “Investigation of nanoscale morphological changes in organic photovoltaics during solvent vapor annealing,” *J. Mater. Chem.*, vol. 18, pp. 306–312, 2008.

[164] T. F. Guo, T. C. Wen, G. L’vovich Pakhomov, X. G. Chin, S. H. Liou, P. H. Yeh, and C. H. Yang, “Effects of film treatment on the performance of poly(3-hexylthiophene)/soluble fullerene-based organic solar cells,” *Thin Solid Films*, vol. 516, pp. 3138–3142, 2008.

[165] B. Paci, A. Generosi, V. R. Albertini, G. D. Spyropoulos, E. Stratakis, and E. Kymakis, “Enhancement of photo/thermal stability of organic bulk heterojunction photovoltaic devices via gold nanoparticles doping of the active layer,” *Nanoscale*, vol. 4, pp. 7452–7459, 2012.

[166] P. R. Brown, R. R. Lunt, N. Zhao, T. P. Osedach, D. D. Wanger, L. Y. Chang, M. G. Bawendi, and V. Bulović, “Improved current extraction from ZnO/PbS quantum dot heterojunction photovoltaics using a MoO_3 interfacial layer,” *Nano Lett.*, vol. 11, pp. 2955–2961, 2011.

[167] S. Kim, S. H. Im, M. Kang, J. H. Heo, S. Il Seok, S.-W. Kim, I. Mora-Seró, and J. Bisquert, “Air-stable and efficient inorganic–organic heterojunction solar cells using PbS colloidal quantum dots co-capped by 1-dodecanethiol and oleic acid,” *Phys. Chem. Chem. Phys.*, vol. 14, pp. 14999–15002, 2012.

[168] R. J. Ellingson, M. C. Beard, J. C. Johnson, P. Yu, O. I. Micic, a J. Nozik, a Shabaev, and a L. Efros, “Highly Efficient Multiple Excition Generation in Colloidal PbSe and PbS Quantum Dots,” *Nano Lett.*, vol. 5, pp. 865–871,

2005.

[169] G. F. Brown and J. Wu, “Third generation photovoltaics,” *Laser Photonics Rev.*, vol. 3, pp. 394–405, 2009.

[170] M. Law, M. C. Beard, S. Choi, J. M. Luther, M. C. Hanna, and A. J. Nozik, “Determining the internal quantum efficiency of PbSe annocrystal solar cells with the aid of an optical model,” *Nano Lett.*, vol. 8, pp. 3904–3910, 2008.

[171] E. Barsoukov and J. R. Macdonald, *Impedance Spectroscopy Theory, Experiment, and Applications*, 2nd. ed. Hoboken, New Jersey: Wiley & Sons, Inc., 2005.

[172] T. Kuwabara, Y. Kawahara, T. Yamaguchi, and K. Takahashi, “Characterization of inverted-type organic solar cells with a ZnO layer as the electron collection electrode by ac impedance spectroscopy,” *ACS Appl. Mater. Interfaces*, vol. 1, pp. 2107–2110, 2009.

VITA

The author, İdris Candan was born at Hatay, Turkey. He received his Bs degree in Physics Department from Kocaeli University in 2004. Idris got his Ms degree from Physics Department of Middle East Tachnical University (**METU**) in 2009. His Ms thesis was on "Growth and Characterization of $CuIn_{1-x}Ga_xSe_2$ (CIGS) Thin Films For Solar Cell Structure". He has worked as a Research Assistant at METU and also as a researcher at The Center for Solar Energy Research and Applications (**GÜNAM**).

He joined the Device Research Laboratory (DRL) in the Electrical Engineering Department at University of California, Los Angeles (**UCLA**) on February 2014 as a Visiting Scholar (Visiting Researcher) till January 31, 2015. He worked at Western Institute of Nanoelectronics (WIN) at UCLA as a Development Engineer from February 1, 2015 through May 28, 2015. His research interests include thin film solar cell, nanomaterials for flexible electronics and energy converting devices and diluted magnetic semiconductor devices. His recent publications are :

A. Articles

1- H.H. Güllü, **İ. Candan**, E. Coşkun, M. Parlak, "*Investigation of Structural and Optical Parameters of Cu-Ag–In–Se Thin Films Deposited by Thermal , Evaporation Method*" Optik - International Journal for Light and Electron Optics, Vol. 126, issue 18, p. 1578-1583, 2015. (doi:10.1016/j.ijleo.2015.05.026)

2- E. Coşkun, H.H. Güllü, **İ. Candan**, Ö. Bayraklı, M. Parlak, Ç. Erçelebi "*Device Behavior of an In/p-Ag(Ga, In)Te_2/n-Si/Ag Heterojunction Diode*", Material Science in Semiconductor Processing, Vol. 34, p.138-145, 2015. (doi:10.1016/j.mssp.2015.02.043)

3- H. H. Güllü, Ö. Bayraklı, **İ. Candan**, E. Coşkun, M. Parlak, *"Structural and optical properties of Zn-In-Te thin films deposited by thermal evaporation technique"*, Journal of Alloys and Compounds, 566, p. 83-89, 2013. (doi:10.1016/j.jallcom.2013.03.030)

B. Posters:

1-H. H.Güllü, E. Coşkun, Ö. Bayraklı, **İ. Candan**, M. Parlak, "Characterization of Sputtered Cu-Zn-Sn-Te Thin Films for Device Applications", *Є-MRS Spring Meeting 2014, Lille- FRANCE, 26 May – 30 May 2014*

2- **İ. Candan**, H. H. Güllü, Ö. Bayraklı, M. Parlak and Ç. Erçelebi, "Growth and optimization of ZIT thin films for photovoltaic applications", *9th Nanoscience and Nanotechnology Conference, Erzurum, TURKEY, 24 June -28 July 2013*

3- H. H. Güllü, **İ. Candan**, and M. Parlak "Characterization of co-evaporated Cu-Ag-In-Se thin film by the physical vapor deposition", *9th Nanoscience and Nanotechnology Conference, Erzurum, TURKEY, 24 June -28 July 2013*

4- G. Kılıçerkan, **İ. Candan**, H. H. Güllü, R. Turan and M. Ertuğrul, "Structural characterization of aluminum induced polycrystalline silicon films", *9th Nanoscience and Nanotechnology Conference, Erzurum, TURKEY, 24 June -28 July 2013*

5- **İ. Candan**, H. H. Güllü, Ö. Bayraklı, M. Parlak and Ç. Erçelebi, "Growth and characterization of Ga-rich $CuIn_{1-x}Ga_xSe_2$ (CIGS) thin films by sputtering technique for photovoltaic application", *Є-MRS Spring Meeting 2013, Strasbourg- FRANCE, 27May – 31 May 2013*

6- H. H. Güllü, **İ. Candan**, Ö. Bayraklı, Ç. Erçelebi and M. Parlak, "Investigation of the physical properties of Cu-In-Zn-Se Thin Films Deposited by Sputtering" *Є-MRS Spring Meeting 2013, Strasbourg- FRANCE, 27May – 31 May 2013*

7- **İ. Candan**, H. H. Güllü, Ö. Bayraklı, M. Parlak and Ç. Erçelebi, "Effect of In/Ga Ratio on The Properties of Semiconductor $CuIn_{1-x}Ga_xSe_2$ (CIGS) Thin Films", *SolarTR-2, Antalya,TURKEY, 06 November - 09 November 2012*

8- H. H. Güllü, **İ. Candan**, M. Parlak, and Ç. Erçelebi, "Investigation of Structural, Electrical and Optical Properties of $Cu_{1-x}Ag_xInSe_2$ Thin Films with Different Cu-Ag Ratios", *7th Nanoscience and Nanotechnology Conference, İstanbul, TURKEY, 27 June -1 July 2011*

9- **İ. Candan**, H. H. Güllü, M. Parlak, and Ç. Erçelebi, "The Structural and Optical Analyzing of CIGS Thin Films Deposited by Sputtering Technique", *7th Nanoscience and Nanotechnology Conference, İstanbul, TURKEY, 27 June -1 July 2011*

10- **İ. Candan**, M. Parlak and Ç. Erçelebi, "Characterization of CIGS Thin Films Deposited with Double Sources e-beam Evaporation by the Three-stage Process", *Є-MRS Spring Meeting 2010, Strasbourg- FRANCE, 07 June – 11 June 2010*

11- **İ. Candan**, H. Karaağaç, M. Parlak, Ç. Erçelebi, "Electrical and Optical Characterization of $CuIn_{0.5}Ga_{0.5}Se_2$ Thin Films Deposited by Electron Beam Technique for Solar Cell Structures", *SolarTR-1, METU – Ankara, TURKEY, 29-30 April 2010*

12- M. Kaleli, M. Parlak, H. Karaağaç, Ç. Erçelebi, **İ. Candan**, "The Device Behaviors of p-Si/n-(Ag-In-Se) Junction", *Є-MRS Spring Meeting 2009, Strasbourg- FRANCE, 8 June – 12 June 2009*

13- H. Karaağaç, M. Parlak, **İ. Candan**, M. Kaleli "Annealing Effects on the Structural and Optical Properties of $AgGa_{0.5}In_{0.5}Se_2$ Thin Films Deposited by Electron Beam Technique", *Є-MRS Spring Meeting 2009, Strasbourg- FRANCE, 8 June – 12 June 2009*

C. Oral Presentations

1- Ö. Bayraklı, H. H. Güllü, **İ. Candan,** E. Coşkun**,** M. Parlak, and Ç. Erçelebi, "Characterization of Ag-Ga-In-Te Thin Film for Solar Cell Applications.", *Science and Applications of Thin Films, Conference and Exhibition, Izmir, Turkey, September 15-19, 2014.*